JETP Letters, Vol. 81, No. 7, 2005, pp. 303–306. From Pis'ma v Zhurnal Éksperimental'noĭ i Teoreticheskoĭ Fiziki, Vol. 81, No. 7, 2005, pp. 387–390.

Indication of Asymptotic Scaling in the Reactions $dd \longrightarrow p^3\mathrm{H}$, $dd \longrightarrow n^3\mathrm{He}$, and $pd \longrightarrow pd$¶

Yu. N. Uzikov

Joint Institute for Nuclear Research, LNP, Dubna, Moscow region, 141980 Russia

e-mail: uzikov@nusun.jinr.ru

Received January 11, 2005; in final form, February 28, 2005

It is shown that the differential cross sections of the reactions $dd \longrightarrow n^3\mathrm{He}$ and $dd \longrightarrow p^3\mathrm{H}$ measured at a c.m.s. scattering angle $\theta_{cm} = 60°$ in the interval of the deuteron beam energy 0.5–1.2 GeV demonstrate the scaling behavior $d\sigma/dt \sim s^{-22}$, which follows from constituent quark counting rules. It is found also that the differential cross section of the elastic $dp \longrightarrow dp$ scattering at $\theta_{cm} = 125°$–$135°$ follows the scaling regime $\sim s^{-16}$ at beam energies 0.5–5 GeV. These data are parameterized here using the Reggeon exchange. © *2005 Pleiades Publishing, Inc.*

PACS numbers: 13.75.–n, 24.85.+p, 25.10.+s, 25.40.Cm

Nuclei and nuclear reactions at low and intermediate energies (or at long and medium distances between nucleons $r_{NN} > 0.5$ Fm) traditionally are described in terms of effective nucleon–nucleon interactions that are mediated by the exchange of mesons. In the limit of very high energies ($s \longrightarrow \infty$) and transferred four-momenta ($t \longrightarrow \infty$), the perturbative quantum chromodynamics (pQCD) is expected to be applied to an explanation of nuclear reactions in terms of quarks and gluons. At present, one of the most interesting problems in nuclear physics is the interplay between the meson–baryon and quark–gluon pictures of the strong interaction. The main question is the following: at which s and t values (or, more precisely, relative momenta q of nucleons in nuclei) does the transition region from the meson–baryon to the quark–gluon picture of nuclei set in?

A possible signature for this transition is given by the constituent counting rules (CCR) [1, 2]. According to dimensional scaling [1, 2] and pQCD [3], the differential cross section of a binary reaction $AB \longrightarrow CD$ at sufficiently high incident energy can be parameterized for a given c.m.s. scattering angle θ_{cm} as

$$\frac{d\sigma}{dt}(AB \longrightarrow CD) = \frac{f(t/s)}{s^{n-2}}, \qquad (1)$$

where $n = N_A + N_B + N_C + N_D$ (N_i is the minimum number of pointlike constituents in the ith hadron; for a lepton, one has $N_l = 1$) and $f(s/t)$ is a function of θ_{cm}. The existing data for many measured hard scattering processes with free hadrons appear to be consistent with Eq. (1) [4]. At present, in a nuclei sector, only electromagnetic processes on the deuteron were found to be compatible with the CCR. Thus, the deuteron electromagnetic form factor measured at SLAG [5] and JLab [6] at high momentum transfer $Q^2 > 4$ GeV^2 approaches to the scaling as $\sqrt{A(Q^2)} \longrightarrow Q^{-10}$, which is in agreement with the CCR. The deuteron two-body photodisintegration cross section $\gamma d \longrightarrow pn$ demonstrates the s^{-11} scaling behavior in the data obtained in SLAG [7–9] at $E_\gamma > 1$ GeV, $\theta_{cm} \approx 90°$, and Jlab [10] at $E_\gamma = 1$–2 GeV for $\theta_{cm} = 89°$, 69° [11]. According to the data [10], at a photon energy of 3.1 GeV and scattering angle $\theta_{cm} = 36°$, there is no evidence for the s^{-11} scaling. A nearly complete angular distribution of the cross section of this reaction recently measured at energies 0.5–3.0 GeV [12] demonstrates the s^{-11} behavior at proton transverse momenta $p_T > 1.1$ GeV/c [13]. Meson-exchange models fail to explain the $\gamma d \longrightarrow pn$ data at $E_\gamma > 1$ GeV (see, for example, [10] and references [3, 4, 9, 10] therein). Recent models based on quark degrees of freedom have become quite successful in describing this data. Thus, the observed in [8, 11] forward–backward asymmetry was described within the Quark–Gluon String (QGS) model [14] using a nonlinear Regge trajectory of the nucleon. Other quark models applied to this reaction are reviewed in [15].

The dimensional scaling was derived before the QCD was discovered. The main assumption was a self-similarity hypothesis for the amplitude of the binary reaction with pointlike constituents in colliding (and outgoing) particles and sufficiently high s and t [1]. The pQCD (and, consequently, the scaling behavior within the pQCD) is expected to be valid at very high transferred momenta that have not yet been reached in existing data for nucleon and deuteron form factors [16, 17]. From this point of view, the origin of the scaling behav-

¶ This article was submitted by the author in English.

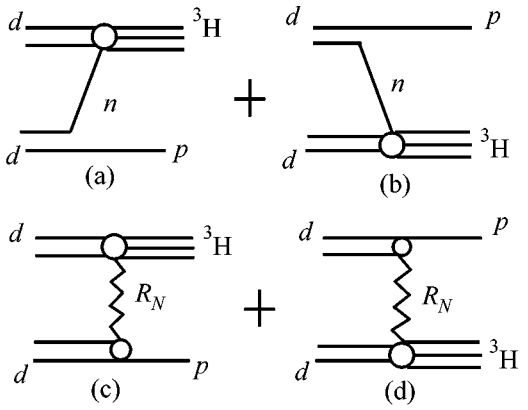

Fig. 1. The mechanisms of the reaction $dd \longrightarrow p^3\mathrm{H}$: one nucleon exchange (a, b), Reggeon exchange (c, d).

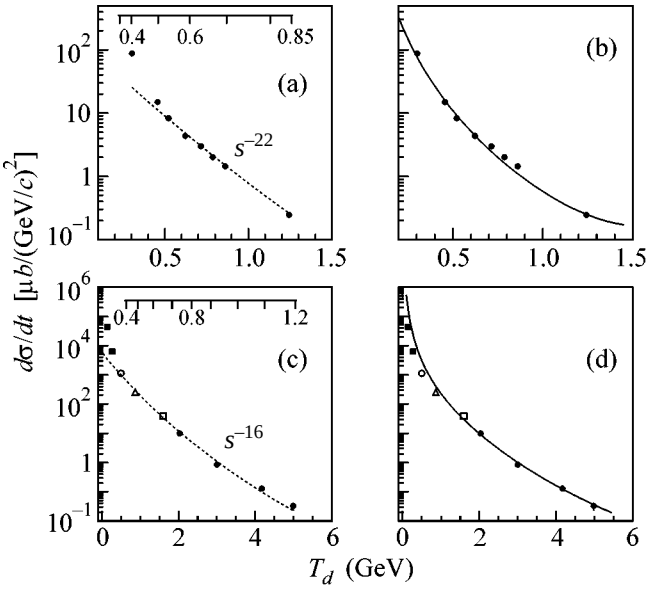

Fig. 2. The differential cross section of the $dd \longrightarrow n^3\mathrm{He}$ and $dd \longrightarrow p^3\mathrm{H}$ reactions at $\theta_{cm} = 60°$ (a), (b) and $dp \longrightarrow dp$ at $\theta_{cm} = 127°$ (c), (d) versus the deuteron beam kinetic energy. Experimental data in (a), (b) are taken from [20]. In (c), (d), the experimental data (closed squares), (○), (△), (open square), and (●) are taken from [22–26], respectively. The dashed curves give the s^{-22} (a) and s^{-16} (c) behavior. The full curves show the result of calculations using the Regge formalism given by Eqs. (2)–(4) with the following parameters: (b) $C_1 = 1.9$ GeV^2, $R_1^2 = 0.2$ GeV^{-2}, $C_2 = 3.5$, $R_2^2 = -0.1$ GeV^{-2}; (d) $C_1 = 7.2$ GeV^2, $R_1^2 = 0.5$ GeV^{-2}, $C_2 = 1.8$, $R_2^2 = -0.1$ GeV^{-2}. The upper scales in (a) and (c) show the relative momentum q_{pn} (GeV/c) in the deuteron for the ONE mechanism.

ior observed in the reactions with the deuteron at moderate transferred momenta [5–12] is unclear and considered in some papers as a potentially misleading indicator of the success of pQCD [15]. Moreover, the hadron helicity conservation predicted by the pQCD was not confirmed experimentally in the scaling region (see [18] and references therein). On the other hand, in these reactions, the three-momentum transfer Q = 1–5 GeV/c is large enough to probe very short distances between nucleons in nuclei, $r_{NN} \sim 1/Q < 0.3$ Fm, where 0.3 Fm is the size of a constituent quark [19]. One may expect nucleons to lose their separate identity in this overlapping region and, therefore, six-quark (or, in the general case, multiquark) components of a nucleus can be probed in these reactions. In order to get more insight into the underlying dynamics of the scaling behavior, new data are necessary, in particular for hadron–nuclei interactions.

In the present paper we show that, in hadron interactions with the participation of the lightest nuclei ^{2}H, ^{3}H, and ^{3}He, the scaling behavior given by Eq. (1) is also occurs, specifically, at beam energies around 1 GeV if the scattering angle is large enough. In order to estimate at which internal momenta q_{pn} between nucleons in the deuteron one should expect the scaling onset, we consider here the reaction $\gamma d \longrightarrow pn$ assuming that the one-nucleon-exchange (ONE) mechanism dominates. Under this assumption, the cross section is proportional to the squared wave function of the deuteron in momentum space: $d\sigma \sim |\psi_d(q_{pn})|^2$. Using relativistic kinematics, we find that q_{pn} is larger than 1 GeV/c at the photon energy $E_\gamma > 1$ GeV and $\theta_{cm} = 90°$. Furthermore, assuming for the reaction $dd \longrightarrow p^3\mathrm{H}$ (or $dd \longrightarrow n^3\mathrm{He}$) that the ONE mechanism dominates (Figs. 1a and 1b), we get $d\sigma \sim |\psi_d(q_{pn})|^2 \times |\Psi_h(q_{Nd})|^2$, where $\Psi_h(q_{Nd})$ is the overlap between the ^{3}H(^{3}He) and deuteron wave functions and q_{Nd} is the $N - d$ relative momentum in the ^{3}H(^{3}He). On this basis we obtain, for example, at T_d = 0.8 GeV and $\theta_{cm} = 90°$, the relative momenta q_{pn} = 0.8 GeV/c and $q_{Nd} = 1.0$ GeV/c. These values are close to those that we have found for the $\gamma d \longrightarrow pn$ reaction in the scaling region. Therefore, one may expect that the scaling behavior in the $dd \longrightarrow n^3\mathrm{He}$ reaction occurs in the GeV region for large scattering angles, $\theta_{cm} \sim 90°$. In Figs. 2a and 2b, we show the experimental data from [20] obtained at SATURNE at beam energies 0.3–1.25 GeV for the maximum measured scattering angle $\theta_{cm} = 60°$. Shown on the upper scale is the minimum relative momentum in the deuteron for the ONE diagram. One can see that, at beam energies 0.5–1.25 GeV, the data perfectly follow the s^{-22} dependence. (In this reaction, $n = 6 + 6 + 9 + 3 = 24$.) In Fig. 2a, the dashed curve represents the s^{-22} dependence with arbitrary normalization fitted on the data with $\chi^2_{n.d.f.} = 1.18$. For the ONE diagram in Fig. 1b, which dominates at $\theta_{cm} = 60°$, this region corresponds to the internal momenta q_{pn} =

0.55–0.85 GeV/c in the deuteron and q_{Nd} = 0.60–0.94 GeV/c in the ^{3}He (^{3}H) nuclei. Therefore, within this model, the probed NN distances in the deuteron are less than $r_{NN} < 1/0.55$ GeV/c = 0.35 Fm. This regime, in principle, corresponds to the formation of a six-quark configuration in the deuteron. At $\theta_{cm} = 90°$, the diagrams in Figs. 1a and 1b are equivalent and correspond to higher momenta q_{pn} = 0.7–1.1 GeV/c and q_{Nd} = 0.80–1.22 GeV/c for the same beam energies 0.5–1.25 GeV. Therefore, continuation of measurements up to $\theta_{cm} = 90°$ is very desirable to confirm the observed s^{-22} behavior. One can see on the linear scale that the cross section $s^{-22}d\sigma/dt$ demonstrates some oscillations that are similar to those observed in pp scattering at $\theta_{cm} = 90°$ [21]. However, the number of available experimental points is too small in the scaling region (five or six) and has to be increased to reach a more definite conclusion.

The $dp \longrightarrow dp$ data obtained in different experiments [22–26] at the c.m.s. scattering angle $\theta_{cm} = 127°$ are shown in Figs. 2c and 2d versus the deuteron beam energy T_d. This scattering angle corresponds to a region of the minimum in the angular dependence of the differential cross section $dp \longrightarrow dp$, where the contribution of the three-body forces (and nonnucleon degrees of freedom in the deuteron) is expected to be best pronounced [27, 28]. One can see that, at low energies (<0.25 GeV), the cross section falls very fast with increasing T_d, but the slope of the energy dependence is sharply changed at about 0.5 GeV. Above this energy, the cross section appears to follow the s^{-16} scaling behavior. (In the $dp \longrightarrow dp$, one has $n = 3 + 6 + 3 + 6 = 18$.) We can show that a similar behavior is observed at $\theta_{cm} = 135°$. However, the parameter $\chi^2_{n.d.f.}$ is rather high for the $dp \longrightarrow dp$ data, namely, $\chi^2_{n.d.f.} = 4.3$. The high $\chi^2_{n.d.f.}$ value can presumably be attributed to uncertainties due to systematic errors that are different in various experiments [26]. Therefore, new, more detailed data are needed, preferably from one experiment covering the whole interval of energies T_d = 1–5 GeV. We notice that the discrepancy observed in [29] between the results of the Faddeev calculations and the measured unpolarized cross section of the $pd \longrightarrow pd$ at T_p = 0.25 GeV (corresponding to T_d = 0.5 GeV in the $dp \longrightarrow dp$), is, presumably, caused by the deuteron six-quark component that is not taken into account in [29] but, as seen from Fig. 2c, starts playing a role in the $pd \longrightarrow pd$ at this kinematics.

Due to very high internal momenta in the $d \Longleftrightarrow pn$ and $Nd \Longleftrightarrow {}^3\mathrm{H}({}^3\mathrm{He})$ vertices, $q \sim 1$ GeV/c, calculation with the ^{3}H(^{3}He) and deuteron wave functions obtained from the Schrödinger equation with conventional NN potentials are likely unrealistic. Since, in the reactions $\gamma d \longrightarrow pn$, $dd \longrightarrow p^3\mathrm{H}$ (or $dd \longrightarrow n^3\mathrm{He}$), and $dp \longrightarrow dp$ (in the backward hemisphere), an important contribution comes from the baryon-exchange mechanism, for numerical estimations we apply here the Reggeon exchange formalism developed earlier for the $pp \longrightarrow d\pi^+$ reaction at $-t < 1.6$ (GeV/c)^2 [30] and the $\gamma d \longrightarrow pn$ at $E_\gamma > 1$ GeV [14]. In this way, one may estimate to what extent the observed scaling behavior in the $dd \longrightarrow n^3\mathrm{He}$ ($dd \longrightarrow p^3\mathrm{H}$) and $dp \longrightarrow dp$ reactions is connected to that in the $\gamma d \longrightarrow pn$. The amplitude of the reaction $dd \longrightarrow p^3\mathrm{H}$ can be written as

$$T = T(s, t) + T(s, u), \qquad (2)$$

where the first (second) term corresponds to the diagram in Figs. 1a, 1b and the plus sign is chosen due to the Bose statistics for the deuterons. The amplitude $T(s, t)$ is written in the Regge form:

$$T(s, t) = F(t)\left(\frac{s}{s_0}\right)^{\alpha_N(t)} \exp\left[-\frac{i\pi}{2}\left(\alpha_N(t) - \frac{1}{2}\right)\right]. \qquad (3)$$

We use here the effective Regge trajectory for the nucleon from [30]: $\alpha_N(t) = \alpha_N(0) + \alpha'_N t + \alpha''_N/2t^2$ with the parameters $\alpha_N(0) = -0.5$, $\alpha'_N = 0.9$ GeV^{-2} and $\alpha''_N = 0.4$ GeV^{-4}, so $\alpha_N(m_N^2) = 1/2$, where m_N is the nucleon mass. The function $F(t)$ is parameterized as [30]

$$F(t) = \frac{C_1 \exp(R_1^2 t)}{m_N^2 - t} + C_2 \exp(R_2^2 t), \qquad (4)$$

where the first term explicitly takes into account the nucleon pole in the t channel. According to [30], the second term at $R^2 \approx 0$ is important at $|t| > 1$ GeV^2, which indicates the presence of structureless configurations in the deuteron (^{3}He, ^{3}H) wave functions at short distances. The results of calculations are shown in Fig. 2b, and the parameters C and R^2 are given in the caption. One can see fairly good agreement with the data. For the reactions $dd \longrightarrow p^3\mathrm{H}$ and $dd \longrightarrow n^3\mathrm{He}$, the parameter R_1^2 is lower than that used in [30] ($R_1^2 = 3$ GeV^2) to fit the $pp \longrightarrow d\pi^+$ data. Such a diminishing R_1^2 is likely connected to a much more intensive high-momentum nucleon component of the ^{3}He(^{3}H) wave function as compared with the deuteron [31]. The increasing ratio C_1/C_2 could mean that multiquark configurations in the ^{3}He(^{3}H) become more important at given t as compared with the deuteron. We also performed this analysis for the $dp \longrightarrow dp$ reaction and obtained good agreement with the data under minor modification of the parameters R_1^2 and C_1/C_2 (see Fig. 2d).

In conclusion, the CCR scaling behavior is observed in cross sections of hadron–nucleus reactions with the deuteron and ^{3}He(^{3}H) nuclei. This behavior sets in at energies around 1 GeV and large scattering angles, where the high-momentum components of nuclear wave functions are required in the Schrödinger formalism. To confirm this observation, more detailed data are

necessary for these and other exclusive reactions in the pd, dd, p^3He collisions, probably including meson production.

I am thankful to V.I. Komarov, A.V. Kulikov, V.V. Kurbatov, B. Pire, and H. Seyfarth for stimulating discussions.

REFERENCES

1. V. A. Matveev, R. M. Muradyan, and A. N. Tavkhelidze, Lett. Nuovo Cimento **7**, 719 (1973).
2. S. J. Brodsky and G. R. Farrar, Phys. Rev. Lett. **31**, 1153 (1973).
3. S. J. Brodsky and G. R. Farrar, Phys. Rev. D **11**, 1309 (1975).
4. R. L. Anderson, D. B. Gustavson, D. M. Ritson, *et al.*, Phys. Rev. D **14**, 679 (1976).
5. R. G. Arnold, B. T. Chertok, E. B. Dally, *et al.*, Phys. Rev. Lett. **35**, 776 (1975).
6. L. C. Alexa, B. D. Anderson, K. A. Aniol, *et al.*, Phys. Rev. Lett. **82**, 1374 (1999).
7. J. Napolitano, S. J. Freedman, D. F. Geesaman, *et al.*, Phys. Rev. Lett. **61**, 2530 (1988).
8. S. J. Freedman, D. F. Geesaman, R. Gilman, *et al.*, Phys. Rev. C **48**, 1864 (1993).
9. J. E. Belz, D. H. Potterveld, P. Anthony, *et al.*, Phys. Rev. Lett. **74**, 646 (1995).
10. C. Bochna, B. P. Terburg, D. J. Abbott, *et al.*, Phys. Rev. Lett. **81**, 4576 (1998).
11. E. C. Schulte, A. Afanasev, M. Amarian, *et al.*, Phys. Rev. C **66**, 042201(R) (2002).
12. M. Mirazita, F. Ronchetti, P. Rossi, *et al.*, Phys. Rev. C **70**, 014005 (2004).
13. P. Rossi, M. Mirazita, F. Ronchetti, *et al.*, hep-ph/0405207.
14. V. Yu. Grishina, L. A. Kondratyuk, W. Cassing, *et al.*, Eur. Phys. J. A **10**, 355 (2001); Eur. Phys. J. A **19**, 117 (2004).
15. R. Gilman and F. Gross, J. Phys. G **28**, R37 (2002).
16. N. Isgur and C. H. Llewellyn Smith, Phys. Rev. Lett. **52**, 1080 (1984); Phys. Lett. B **217**, 535 (1989).
17. G. R. Farrar, K. Huleihel, and H. Zhang, Phys. Rev. Lett. **74**, 650 (1995).
18. K. Wijesooriya, A. Afanasev, M. Amarian, *et al.*, Phys. Rev. Lett. **86**, 2975 (2001).
19. D. Diakonov, hep-ph/0406043.
20. G. Bizard, J. L. Laville, C. Le Brun, *et al.*, Phys. Rev. C **22**, 1632 (1980).
21. B. Pire and J. P. Ralston, Phys. Lett. B **117**, 233 (1982).
22. K. Sekiguchi, H. Sakai, H. Witala, *et al.*, Phys. Rev. C **65**, 034003 (2002).
23. K. Hatanaka, Y. Shimizu, D. Hirooka, *et al.*, Phys. Rev. C **66**, 044002 (2002).
24. N. E. Booth, C. Dolnick, R. J. Esterling, *et al.*, Phys. Rev. D **4**, 1261 (1971).
25. E. Winkelman, P. R. Bevington, M. W. McNaughton, *et al.*, Phys. Rev. C **21**, 2535 (1980).
26. L. Dubal, C. K. Hargrove, E. P. Hincks, *et al.*, Phys. Rev. D **9**, 597 (1974).
27. H. Witala, W. Glöckle, D. Hüber, *et al.*, Phys. Rev. Lett. **81**, 1183 (1998).
28. Yu. N. Uzikov, Pis'ma Zh. Éksp. Teor. Fiz. **75**, 7 (2002) [JETP Lett. **75**, 5 (2002)].
29. H. Witala, J. Golak, W. Glöckle, and H. Kamada, nucl-th/0412063.
30. A. Kaidalov, Yad. Fiz. **53**, 1410 (1991) [Sov. J. Nucl. Phys. **53**, 872 (1991)].
31. R. Sciavilla, V. R. Pandharipande, and R. B. Wiringa, Nucl. Phys. A **449**, 219 (1986).

JETP Letters, Vol. 81, No. 7, 2005, pp. 307–310. From Pis'ma v Zhurnal Éksperimental'noĭ i Teoreticheskoĭ Fiziki, Vol. 81, No. 7, 2005, pp. 391–394.

Soft and Hard Processes in QCD¶

I. M. Dremin

Lebedev Physical Institute, Russian Academy of Sciences, Moscow, 119991 Russia

e-mail: dremin@lpi.ru

Received February 28, 2005

QCD equations for the generating functions are applied to separate soft and hard jets in e^+e^- processes of multiparticle production. The dependence of average multiplicities and higher moments of multiplicity distributions of particles created in "newly born" soft subjets on the share of energy devoted to them is calculated in fixed coupling gluodynamics. This dependence is the same as for the total multiplicity up to a constant factor if soft jets are defined as those carrying out a fixed share of initial energy at all energies. The constant factor depends on this share in a nontrivial way. Other definitions are also proposed. The relation between these quantities for soft and hard processes is discussed. © *2005 Pleiades Publishing, Inc.*

PACS numbers: 12.38.Bx

In multiparticle production, it is quite a common procedure to separate all processes into soft and hard. Even though the intuitive approach is appealing, the criteria of the separation differ. It is shown below that QCD equations for the generating functions can be applied to this problem. It is demonstrated how the average multiplicities of soft and hard processes depend on the parameter that is used to distinguish between them. The same method can be applied to any moment of the multiplicity distributions, as is explicitly shown for the second moment (dispersion).

The QCD equations for the generating functions (functionals) have been known for a long time (e.g., see [1]). This is the system of two integro-differential equations that describe the evolution of quark and gluon jets. They are quite useful for the prediction and description of many properties of high-energy jets (for reviews see, e.g., [2–4]). It has been found that the main qualitative features of the process can be safely predicted by considering the single equation for gluon-jet evolution. In that, way one neglects quarks and treats gluodynamics instead of chromodynamics. Moreover, its solution may be further simplified if one disregards the running property of the QCD coupling strength and considers it to be fixed (see [5]). To avoid some technicalities, we adopt this approach in what follows and treat the multiplicity distributions of gluon jets. Both quark and gluon jets with running coupling strengths will be considered in the QCD context elsewhere.

When an initial gluon splits into two gluons (subjets), its energy E is additively shared among them, and the multiplicity of the whole process is a sum of the multiplicities of these two subjets. The energy dependence of the mean multiplicity of particles created in a subjet, which carries out some share of the initial energy xE with a fixed value of x, must be the same as for the initial jet if the gluons are equivalent. In experiments it is more convenient to deal with values of x ranging in some finite interval to get enough statistics. One of the ways to define this is to separate all of the subjets into soft and hard according to whether the parameter x is smaller or larger than some x_0. We show how the properties of these two sets behave with energy. We shall also consider the case when the parameter x_0 depends on the initial energy.

If the probability to create n particles[1] in a jet is denoted as P_n, the generating function G is defined as

$$G(z, y) = \sum_{n=0}^{\infty} P_n(y)(1+z)^n, \tag{1}$$

where z is an auxiliary variable; $y = \ln(p\Theta/Q_0) = \ln(2Q/Q_0)$ is the evolution parameter defining the energy scale; p is the initial momentum; Θ is the angle of the divergence of the jet (jet opening angle), assumed here to be fixed; Q is the jet virtuality; and $Q_0 = \text{const}$.

The gluodynamics equation for the generating function is written as

$$\frac{dG}{dy} = \int_0^1 dx K(x)\gamma_0^2 \times [G(y+\ln x)G(y+\ln(1-x)) - G(y)], \tag{2}$$

where

$$\gamma_0^2 = 6\alpha_S/\pi, \tag{3}$$

¶ This article was submitted by the author in English.

[1] In what follows, we adopt the local parton–hadron duality hypothesis with no difference between the notions of particles and partons up to some irrelevant factor.

α_S is the coupling strength, and the kernel $K(x)$ is

$$K(x) = 1/x - (1-x)[2 - x(1-x)]. \quad (4)$$

One should not be surprised that the shares of energy x and $1-x$ split between the two gluons after the initial one divides to form them enter asymmetrically into this equation. Surely, the initial equation is fully symmetrical. The asymmetry is introduced when the phase space is separated into two equally contributing parts: then, the jet with the share x is called the "newly born" one (for more details, see [1]). Therefore, we shall call soft processes those in which soft newly born jets are produced, i.e., those where x is sufficiently small ($x \le x_0 \ll 1$). In e^+e^- experiments, this would correspond to considering soft newly born gluon jets with energies $E_g \le x_0 E \ll E$ in three-jet events.

Before separating soft and hard jets, let us stress that, at a given energy, this is an additive procedure for probabilities $P_n = P_{ns} + P_{nh}$ and, consequently, for $G = G_s + G_h$, where the indices s and h are for soft and hard processes, respectively. It is convenient to rewrite the generating function in terms of unnormalized factorial moments

$$\mathcal{F}_q = \sum_n P_n n(n-1)\ldots(n-q+1) = \left.\frac{d^q G(z)}{dz^q}\right|_{z=0}, \quad (5)$$

so that

$$G = \sum_{q=0}^{\infty} \frac{z^q}{q!}\mathcal{F}_q. \quad (6)$$

The low-rank moments are

$$\mathcal{F}_1 = \langle n\rangle, \quad \mathcal{F}_2 = \langle n(n-1)\rangle = D^2 + \langle n\rangle^2 - \langle n\rangle \quad (7)$$

and D is the dispersion

$$D^2 = \langle n^2\rangle - \langle n\rangle^2. \quad (8)$$

It is seen from Eq. (5) that unnormalized moments are additive also. To retain the additivity property, we define the normalized factorial moments for soft and hard jets with the normalization to the total mean multiplicity but not to their multiplicities:

$$F_q = \frac{\mathcal{F}_q}{\langle n\rangle^q} = \frac{\mathcal{F}_{qs} + \mathcal{F}_{qh}}{\langle n\rangle^q} = F_{qs} + F_{qh}. \quad (9)$$

Thus, the total multiplicity is in the denominator. The additivity would be lost if soft and hard values were normalized to their average multiplicities $\langle n_s\rangle$ and $\langle n_h\rangle$. Introducing $f_q = F_q/q!$, we write

$$G = \sum_{q=0}^{\infty} z^q \langle n\rangle^q f_q. \quad (10)$$

The scaling property of the fixed coupling QCD [5] allows one to look for the solution of the Eq. (2) with

$$\langle n\rangle \propto \exp(\gamma y) \quad (\gamma = \text{const}) \quad (11)$$

and get the system of iterative equations for f_q:

$$\gamma q f_q = \gamma_0^2 \int_0^1 dx K(x)\Big[(x^{\gamma q} + (1-x)^{\gamma q} - 1) f_q + \sum_{m=1}^{q-1} x^{\gamma m}(1-x)^{\gamma(q-m)} f_m f_{q-m}\Big]. \quad (12)$$

By definition, $f_1 = 1$, and one gets at, $q = 1$, the relation between γ and γ_0

$$\gamma = \gamma_0^2 \int_0^1 dx K(x)(x^\gamma + (1-x)^\gamma - 1) = \gamma_0^2 M_1(1,\gamma), \quad (13)$$

where

$$M_1(z,\gamma) = \int_0^z dx K(x)(x^\gamma + (1-x)^\gamma - 1). \quad (14)$$

Let us point out that Eq. (13) is derived from the equation for mean multiplicities that follows from Eq. (2):

$$\langle n(y)\rangle' = \int_0^1 dx \gamma_0^2 K(x)(\langle n(y + \ln x)\rangle + \langle n(y + \ln(1-x))\rangle - \langle n(y)\rangle). \quad (15)$$

These results are well known [5]. Here, we would like to consider Eq. (13) in more detail. As follows from Eq. (15), the first two terms in the brackets correspond to the mean multiplicities of two subjets, and their sum is larger than the third term denoting the mean multiplicity of the initial jet (all divided by E^γ). Therefore, the integrand is positive, and Eq. (13) defines the anomalous dimension γ. This does not contradict to the statement that, for a given event, the total multiplicity is the sum of the multiplicities in the two subjets because the averages in Eq. (15) are done at different energies.

For sufficiently small γ and γ_0, one gets

$$\gamma \approx \gamma_0(1 - 0.458\gamma_0 + 0.213\gamma_0^2). \quad (16)$$

For the second moment, one gets the following from Eq. (12) at $q = 2$ for small γ:

$$F_2 \approx \frac{4}{3}(1 - 0.31\gamma). \quad (17)$$

Now, according to the above discussion, we define soft jets as those whose summed constituent particle energies are less than some $x_0 E$. First, consider $x_0 = \text{const}$ and small. Then, we should choose the upper limit of

integration in Eq. (12) equal to x_0. Therefore, the moments of soft processes f_{qs} are calculated as

$$\gamma q f_{qs} = \gamma_0^2 \int_0^{x_0} dx K(x) \Big[(x^{\gamma q} + (1-x)^{\gamma q} - 1) f_q + \sum_{m=1}^{q-1} x^{\gamma m} (1-x)^{\gamma(q-m)} f_m f_{q-m} \Big]. \quad (18)$$

One should not be confused that the total moments (obtained from the average multiplicities of both soft and hard jets) are in the integrand of Eq. (18). This is related to the difference between the notions of multiplicity in a given event and their averages discussed above. The integration over small x up to x_0 chooses just the mean multiplicity of particles belonging to soft jets $\langle n_s \rangle$, while the integration from x_0 to 1 gives that for hard jets.

For $q = 1$, one gets from (18)

$$\frac{\langle n_s \rangle}{\langle n \rangle} = \frac{M_1(x_0, \gamma)}{M_1(1, \gamma)}. \quad (19)$$

For small x_0, this is

$$\frac{\langle n_s \rangle}{\langle n \rangle} \approx \frac{\gamma_0^2}{\gamma^2} x_0^\gamma N_1(x_0, \gamma), \quad (20)$$

$$N_1(x_0, \gamma) = 1 - \gamma^2 x_0^{1-\gamma} - \frac{2\gamma}{1+\gamma} x_0 + \frac{\gamma^2(3+\gamma)}{4} x_0^{2-\gamma} + \frac{3\gamma}{2+\gamma} x_0^2 - \frac{\gamma^2(2+\gamma)}{3} x_0^{3-\gamma}. \quad (21)$$

Thus, we have found the energy dependence of mean multiplicity of particles in a set of subjets with low energies $E_s \le x_0 E$. As expected for constant x_0, it is the same as the energy dependence of the total multiplicity with a different factor in front of it. Namely, this dependence should be checked first with the experimental data. Imposed on one another, these figures should coincide up to normalization factor (19). This would confirm the universality of gluons in jets.

Quite interesting is the nontrivial dependence of the normalization factor in Eq. (19) on the parameter x_0, which does not coincide simply with x_0^γ. It reflects the structure of the QCD kernel $K(x)$. The main dependence on the cutoff parameter x_0 is given for $x_0 \ll 1$ by the factor x_0^γ with the same power as in the dependence of total multiplicity on energy. This corresponds to subjets with the largest energy of the set. However, with an increase in x_0, this dependence is modified according to Eqs. (19)–(21). The negative corrections become more important in Eq. (21). They are induced by subjets with energies lower than $x_0 E$, and their shape reflects the fact that these subjets are weighted according to the kernel

The values of mean multiplicity and second normalized factorial moment for different values of the coupling strength and cutoff parameters x_0

x_0	$\gamma = 0.5$, $\gamma_0 = 0.7$		$\gamma = 0.4$, $\gamma_0 = 0.516$		$\gamma = 0.3$, $\gamma_0 = 0.36$	
	n_s/n	F_{2s}	n_s/n	F_{2s}	n_s/n	F_{2s}
0.1	0.543	0.39	0.605	0.66	0.680	0.76
0.2	0.702	0.51	0.746	0.83	0.798	0.91
0.3	0.798	0.59	0.829	0.93	0.865	1.00

$K(x)$ determined by the QCD Lagrangian. The decrease in the normalization factor corresponds to the diminishing role of very low-energy jets at higher initial energies. This should be also checked experimentally.

If plotted as a function of the maximum energy in a set of jets ϵ_m, the mean multiplicity is

$$\langle n_s \rangle \propto \epsilon_m^\gamma \Big[1 - \gamma^2 \Big(\frac{\epsilon_m}{E}\Big)^{1-\gamma} - \frac{2\gamma}{1+\gamma}\Big(\frac{\epsilon_m}{E}\Big) + \frac{\gamma^2(3+\gamma)}{4}\Big(\frac{\epsilon_m}{E}\Big)^{2-\gamma} + \frac{3\gamma}{2+\gamma}\Big(\frac{\epsilon_m}{E}\Big)^2 - \frac{\gamma^2(2+\gamma)}{3}\Big(\frac{\epsilon_m}{E}\Big)^{3-\gamma} \Big]. \quad (22)$$

This recalls Eq. (11) with the correction factor in the brackets (for $\epsilon_m \ll E$ as in (21)).

This is the consequence of the scaling property of the fixed coupling QCD that results in the jet self-similarity. The relative weights of soft and hard processes are determined by the factor γ_0^2/γ^2, as seen from Eqs. (20) and (21). They can be used to find out this ratio experimentally.

For $q = 2$, we obtain

$$F_{2s} = [0.5 F_2 M_1(x_0, 2\gamma) + M_2(x_0, \gamma)]/M_1(1, \gamma), \quad (23)$$

where

$$M_2(z, \gamma) = \int_0^z dx K(x) x^\gamma (1-x)^\gamma. \quad (24)$$

For small x_0, one gets

$$F_{2s} = \frac{\gamma_0^2}{\gamma^2} x_0^\gamma [0.25 F_2 x_0^\gamma N_1(x_0, 2\gamma) + 2 N_2(x_0, \gamma)], \quad (25)$$

$$N_2(x_0, \gamma) = 1 - \gamma \frac{2+\gamma}{1+\gamma} x_0 + \gamma \frac{6 + 3\gamma + \gamma^2}{2(2+\gamma)} x_0^2. \quad (26)$$

Again, the main dependence on the cutoff parameter x_0 is provided by the factor x_0^γ.

Using these equations, we have calculated the mean multiplicities and second moments of multiplicity distributions for soft jets. They are shown in the table for different choices of γ and γ_0 considered to be the most realistic ones in previous studies. Note that $M_1(z, 2\gamma) = 0$ for $\gamma = 0.5$ (and so is $N_1(x_0, 2\gamma)$). One can notice that, at larger x_0, the values in the table decline from x_0^γ behavior in accordance with Eqs. (19) and (23).

The values for hard jets are obtained by subtracting these results from the values for the total process. Small values of the second factorial moments do not imply that multiplicity distributions in soft jets are sub-Poissonian, because they are normalized to the total mean multiplicity. To get the genuine second factorial moments for these processes, one should divide the numbers in the F_{2s} columns to squared values in the n_s/n columns. In this way, one gets quite large numbers, meaning that these processes are super-Poissonian, but note that the genuine moments are not additive anymore. However, the statement about the widths of the distributions can be compared to experimental data as well.

In principle, other definitions of soft jets are possible with $x_0 = x_0(E)$. Then, one should solve the equation

$$\frac{d\langle n_s\rangle}{dE} = E^{\gamma-1}\gamma_0^2 M_1(x_0(E), \gamma), \qquad (27)$$

which follows from Eq. (15). For example, one can choose the jets with energies less than some fixed constant independent of the initial energy. This would imply $\epsilon_m = \text{const}$ or $x_0(E) \propto 1/E$, and the exact integration of Eq. (27) is necessary. However, for qualitative estimates, Eqs. (20)–(22) can be used. They show that the average multiplicity tends to a constant at high energies corresponding to the multiplicity at the upper limit. At lower energies, it slightly increases with energy due to the increasing role of jets with energies closest to their upper limit.

It is well known that, for a running coupling, the power dependence $s^{\gamma/2}$ is replaced by $\exp(c\sqrt{\ln s})$. The qualitative statement about the similar energy behavior of mean multiplicities in soft and inclusive processes should be valid also.

The above results can be compared to experimental data if soft jets are separated in three-jet events. However, in our treatment we did not consider the common experimental cutoff, which must be also taken into account. This is the low-energy cutoff imposed on a soft jet for the third jet to be observable. It requires the soft jet to not be extremely soft. Otherwise, the third jet is not separated and the whole event is considered to be a two-jet event. Thus, the share of energy must be larger than some x_1, and the integration in Eq. (14) should be from x_1 to x_0. For $x_1 \le x_0 \ll 1$, one gets

$$\frac{\langle n_s\rangle}{\langle n\rangle} = \frac{\gamma_0^2}{\gamma^2}[\nu(x_0) - \nu(x_1)], \qquad (28)$$

where the function $\nu(x)$ is easily guessed from Eqs. (20) and (21). At $x_1 \ll x_0 \ll 1$, Eq. (20) is restored.

The cumulative moments of the distribution are not additive because they are obtained as derivatives of the generating function logarithm, which is not additive for additive G. Thus, the H_q moments [6, 7] are not additive either. Nevertheless, the role of hard jets can be traced by the preasymptotical oscillations of H_q. These oscillations are induced by the terms of the kernel K additive to the $1/x$ term. Thus, the oscillations of H_q are a sensitive test of the shape of the noninfrared terms in the QCD kernels and their integral contributions. Namely, these terms contribute much to hard processes because they favor larger values of x. The stronger their influence, the closer to zero the intercept of H_q with the abscissa axis should be. It would be interesting to get experimental information about the behavior of H_q for soft and hard jets separately.

In conclusion, the separation of soft and hard jets according to the share of energy devoted to the "newly born" jet is proposed. If this is done, the experimentally measured values of mean multiplicities and other multiplicity distribution parameters of particles belonging to the soft jet can be compared with the theoretical predictions obtained above at different values of this share of energy. For a constant share, this dependence is the same as for the average total multiplicity but with a nontrivial x_0 dependence of the factor in front of it. Some predictions are obtained for energy-dependent cutoffs. The conclusions can be compared to experiment.

I am grateful to V.A. Nechitailo and E. Sarkisyan-Grinbaum for useful comments. This work was supported in part by the Russian Foundation for Basic Research, project nos. 03-02-16134, 04-02-16445-a, and NSH-1936.2003.2.

REFERENCES

1. Yu. L. Dokshitzer, V. A. Khoze, A. H. Mueller, and S. I. Troyan, *Basics of Perturbative QCD*, Ed. by J. Tran Thanh Van (Frontieres, Gif-sur-Yvette, 1991).
2. I. M. Dremin, Phys. Usp. **37**, 715 (1994).
3. I. M. Dremin and J. W. Gary, Phys. Rep. **349**, 301 (2001).
4. V. A. Khoze and W. Oche, Int. J. Mod. Phys. A **12**, 2949 (1997).
5. I. M. Dremin and R. C. Hwa, Phys. Lett. B **324**, 477 (1994); Phys. Rev. D **49**, 5805 (1994).
6. I. M. Dremin, Phys. Lett. B **313**, 209 (1993).
7. I. M. Dremin and V. A. Nechitailo, Mod. Phys. Lett. A **9**, 1471 (1994); JETP Lett. **58**, 881 (1993).

JETP Letters, Vol. 81, No. 7, 2005, pp. 311–314. Translated from Pis'ma v Zhurnal Éksperimental'noĭ i Teoreticheskoĭ Fiziki, Vol. 81, No. 7, 2005, pp. 395–398.

Detonation in an Aluminum–Teflon Mixture

A. Yu. Dolgoborodov[1,*], M. N. Makhov[1], I. V. Kolbanev[1], A. N. Streletskiĭ[1], and V. E. Fortov[2]

[1] *Semenov Institute of Chemical Physics, Russian Academy of Sciences, ul. Kosygina 4, Moscow, 119991 Russia*
**e-mail: aldol@chph.ras.ru*

[2] *Institute of High Energy Densities, Joint Institute for High Temperatures, Russian Academy of Sciences, Izhorskaya ul. 13/19, Moscow, 127412 Russia*

Received February 16, 2005

Detonation in an aluminum–fluoroplastic-4 (Teflon) mixture is studied experimentally. To increase reactivity, the initial mixture is pretreated in a mechanochemical activator. As a result, a mechanically activated composite is obtained in the form of thin aluminum layers in a Teflon matrix. The action of a shock wave on a composite sample initiates the steady detonation regime, in which the initial and final substances are in the condensed state. Depending on the percentage composition and density of the mixture, the detonation velocity varies from 700 to 1300 m/s for the speed of sound below 100 m/s in the initial composition. The steady detonation velocity changes insignificantly when sample pores are filled with helium instead of air. The results prove that it is possible in principle to reach the steady detonation regime in reactive condensed mixtures forming final reaction products in the solid state. © *2005 Pleiades Publishing, Inc.*

PACS numbers: 82.33.Vx

Detonation is a self-sustained energy-release process propagating in a reactive medium at a constant velocity exceeding the speed of sound in the initial substance. As a rule, the detonation of condensed explosives results in the formation of gaseous end products, and the process of detonation is satisfactorily described by hydrodynamic theory [1]. Detonation in "gas-free" systems is not forbidden in principle. Although the solid-phase detonation of reactive mixtures has long been studied (see, e.g., [2, 3]), the steady regime has not yet been attained in such systems. Most gas-free systems are reactive mixtures of the oxidant–fuel type. According to Khariton [4], the detonation mechanism in such systems should be classified as the "mixture" type. In contrast to homogeneous explosives, no general criteria of the kinetics of energy release in the detonation of such systems have been established and it is extremely difficult to estimate the detonation capability of a mixture with fixed values of density and particle size. The reaction in mixtures most likely occurs in centers on the contact surface of reagent particles rather than in the entire volume of the substance. The reaction rate is determined not only by the chemical characteristics of reagents but also by the time of component mixing at the front of a shock or detonation wave. The highest reaction rate can be expected in porous samples due to the most favorable conditions for the relative motion and mixing of the components.

Previously [5], we studied the chemical processes occurring in mixtures of aluminum with sulfur and metal oxides under the action of a shock wave. In experiments with high-density mixtures and intense initiation, the reaction decayed at the initial propagation stage. In this case, the reaction rate was apparently insufficient for sustaining the process and the substance was dispersed in an unloading wave before entering the reaction. The detonation regime with a gradual decrease in the velocity of propagation over the sample was reached with low-density charges.

Attempts were made to increase the reactivity of mixtures. The strongest effect was obtained by using preliminary mechanochemical activation. Mixtures were treated in a vibratory mill designed by Aronov [6]. The conditions of mechanical activation were chosen so that the maximum homogenization of the mixture was ensured in the absence of the reaction between reagents in the course of treatment. On the basis of this method, a procedure was developed for obtaining mechanically activated energy composites (MAECs), which are highly homogeneous systems of mechanically bound particles or layers of an oxidant and a fuel of the submicron size. The reactivity of MAECs is much higher than that for ordinary mixtures, which ensures higher velocities of detonation and combustion processes. It should be noted that the application of the mechanochemical activation method to the preparation of energetic materials has begun only recently. For example, the Arrested Reactive Milling method was developed in the USA, and it is used to process aluminum–oxidant mixtures in a mechanochemical activator prior to the onset of a chemical reaction [7].

Among aluminum–oxidant mixtures reacting with the formation of solid products, the aluminum–fluoroplastic-4 (Teflon) (Al/Tf) composite is of special inter-

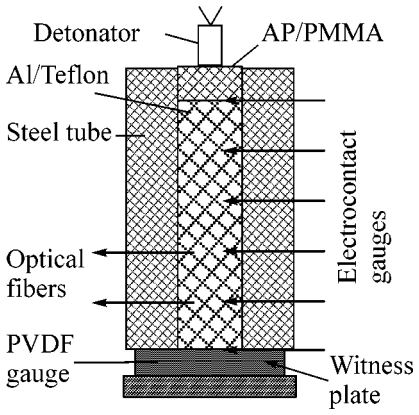

Fig. 1. Schematic diagram of the experiment.

est. This system is advantageous over the mixtures investigated earlier due to a higher thermal effect of the chemical reaction between its components. For example, the thermal effect of the reaction for the stoichiometric mixture (26.5% Al) with condensed end products is equal to 2070 kcal/kg, which exceeds the heat liberated during the explosion of not only high explosives, but also many aluminized explosive compositions [8]. First results on the Al/Tf 45/55 mixture detonation were reported in [9], where the detonation regime with a constant velocity was obtained in a porous MAEC sample. In a density range of 0.4–0.5 g/cm^3, the steady-state detonation velocity increased when density decreased and was equal to 840 m/s for 0.4 g/cm^3.

Ideal detonation in the Al/Tf 45/55 mixture was thermodynamically analyzed in [10]. As possible products, we considered the gaseous (fluid) phase consisting of CF_4 and F_2 molecules, solid and liquid phases of Al and AlF_3, solid graphite and diamond, and liquid carbon. The calculations for the initial density range 1.4–2.0 g/cm^3 show that no gas phase is formed at any point on detonation adiabats. At the same time, each detonation adiabat has a Chapman–Jouguet point at which all classical conditions of ideal detonation are satisfied [1]: D = min, S = min, and D–U_p = C (S is the entropy, U_p is the mass velocity, and C is the speed of sound in the detonation products). Unfortunately, the point of the detonation adiabats at which the Chapman–Jouguet conditions are satisfied could not be established for densities below 1.4 g/cm^3. Further improvement of the thermodynamic method for calculating the detonation parameters of the given mixture is associated primarily with the derivation of the appropriate equations of state for the reaction products. However, the thermodynamic analysis confirms the possibility of steady gas-free detonation in the Al/Tf mixture even at the present stage.

In this paper, we report on new experimental results in the search for gas-free detonation in the Al/Tf MAEC for various concentrations of the components. For preparing mixtures, we used ASD-6 Al powder formed by spherical particles with a mean size of 3.6 μm. The F4-PN Teflon powder contained two fractions: the coarse (main) fraction with a particle size of 10–300 μm and the fine fraction with a size of 1.5–2.5 μm. The mixing and mechanical activation of the components were carried out in Aronov's vibratory mill with the addition of a small amount of hexane, which was subsequently removed by drying the mixture. The energy efficiency of the mill (i.e., the energy passing through 1 g of the material per second during grinding) was 9 W/g. To prevent overheating of the mixture and initiation of the reaction in the activator, the treatment was carried out in 45-s cycles. The total activation time was 15 min. Analysis of the scanning electron microphotographs of Al/Tf MAEC particles showed that the composite particles have the shape of flakes consisting of thin aluminum layers in a Teflon matrix. The linear size of the main fraction of particles ranges from 5 to 50 μm, while their thickness varies from fractions of a micrometer to 1 μm.

X-ray diffraction analysis of the MAEC shows that mechanical activation is followed by the broadening of x-ray lines for both components, which may be due both to a decrease in the size of crystallites (coherent scattering regions) and to the accumulation of dislocations. In particular, the analysis indicates that the broadening of the x-ray lines of Al is caused by the formation of dislocations. The formation of dislocations is apparently associated with the intense plastic deformation of aluminum under mechanical actions. Deformation is accompanied by change in the shape (flattening) of the initially spherical aluminum particles. No products of chemical reactions between the components are detected.

The detonation experiments were carried out in thick-wall composite steel tubes with an inner diameter of 29 mm, which consisted of individual sections with a height of 20–30 mm. The schematic diagram of the experiment is shown in Fig. 1. The Al/Tf mixture was charged in portions into the tube and slightly compressed. An ammonium perchlorate–acrylic plastic mixture (95/5) with a mass of 10 g and a density of 0.55 g/cm^3 was used as the initiator. According to the estimate based on the method proposed in [11], the velocity and pressure of detonation in such a mixture are 2.5 km/s and 1 GPa, respectively. The initiating mixture was detonated by an ED-8 electric detonator. The velocity was measured by electric contact gauges and quartz optical fibers inserted into the mixture to half the diameter. The error of velocity measurements did not exceed 50 m/s. At the end of the charge, a compound witness plate made of duralumin (D16) or Teflon with a piezoelectric pressure gauge was installed. We used polyvinylidene fluoride film (PVDF) gauges, which were prepared and calibrated at the Russian Federal Nuclear Center VNIIEF. In our experiments, a PVDF gauge was mounted between two duralumin or Teflon plates or at the Teflon–acrylic plastic boundary.

The results of measurements of the detonation velocity are presented in Fig. 2, which also shows the data for $Al/S/Fe_2O_3$ 55/33/12 and Al/MoO_3 45/55 mixtures obtained in similar experiments [5]. For mixtures of aluminum with sulfur and metal oxides, the decaying regime was observed. In this case, the process terminated either with the transition to the slow combustion regime or with the formation of a high-density plug consisting of a mixture of reaction products and initial components.

The detonation regime with a constant velocity was obtained for Al/Tf mixtures. For a mixture with a weight ratio of 45/55, the steady-state detonation velocity was 700–850 m/s for a density of 0.4–0.5 g/cm^3. As the stoichiometric ratio of the components (Al/Tf 26.5/73.5) was approached, the detonation velocity increased, and the length of the segment preceding the steady regime decreased from 120–150 mm for the 45/55 mixture to 90 mm for the 25/75 mixture. The steady-state detonation velocity for the 35/65, 30/70, and 25/75 composites was equal to 1050, 1110, and 1280 m/s, respectively. A further decrease in the aluminum concentration reduces the velocity to 700 m/s for the 15/85 mixture.

To find the effect of atmospheric oxygen filling the pores of the sample, we performed an experiment in which the pores of the Al/Tf 45/55 MAEC were filled with helium. The sample density was 0.49 g/cm^3. Prior to the experiment, air was evacuated from the sample sealed in the tube and then helium was blown repeatedly. The results of this experiment show that filling of pores with helium instead of air insignificantly reduces the velocity of the process at the initial stage (by less than 5%). However, at the end of the charge, the velocity is at a level of 700 m/s; i.e., it becomes equal to the value corresponding to the steady-state segment for the sample with air-filled pores. This result indicates that the effect of atmospheric oxygen on the steady-state process velocity is insignificant in the sample under investigation. It should also be noted that the values obtained for the velocity are noticeably higher than the speed of sound in analogous porous mixtures. In the Al/Tf 45/55 mixture, the speed of sound in compressed samples was measured using the ultrasonic method. For a density of 1.2 g/cm^3 (0.5 of the maximal value), the speed was found to be 100 ± 20 m/s. At a lower density, the speed of sound must decrease. However, it could not be measured due to strong damping. Thus, the velocity of propagation of the detonation process in Al/Tf MAEC substantially exceeds the speed of sound in the initial mixture.

The pressure was recorded in various witness plates in experiments with the Al/Tf 45/55 mixture of densities 0.44–0.49 g/cm^3. The time of signal buildup to the maximum value did not exceed 0.5 μs. The maximum pressure was 1.0 GPa in duralumin, 0.6 GPa in Teflon, and 0.5 GPa at the Teflon–acrylic plastic boundary, which made it possible to estimate the pressure in the detonation products of the 45/55 mixture at ~0.1 GPa. For mixtures with a higher detonation velocity, the pressure at the Teflon boundary increased. The maximum pressure in Teflon was equal to 0.75 and 1.1 GPa for the Al/Tf 35/65 mixture of density 0.47 g/cm^3 and for the Al/Tf 30/70 mixture of density 0.55 g/cm^3, respectively. The cellular structure of imprints on the witness plates indicates that the propagation of the process in the systems considered here is accompanied by the formation of high-speed jets or product particles and may occur due to the transfer of the reaction from one center to another.

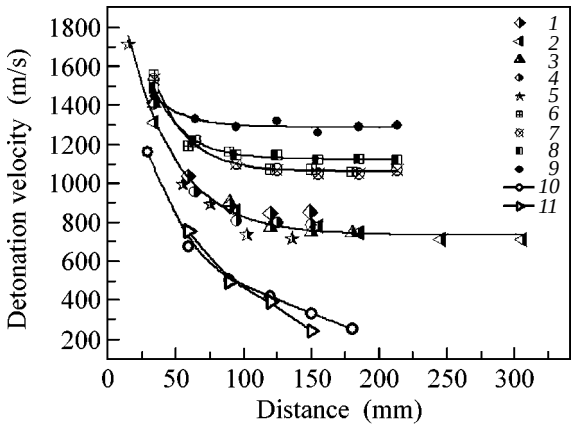

Fig. 2. Detonation velocity over the Al/Tf MAEC charge length for the following compositions: Al/Tf 45/55 of a density of (*1*) 0.40, (*2*) 0.50, (*3*) 0.48, (*4*) 0.44, and (*5*) 0.49 g/cm^3 in helium atmosphere; Al/Tf 35/65 of a density of (*6*) 0.5 and (*7*) 0.47 g/cm^3; (*8*) Al/Tf 30/70 of a density of 0.55 g/cm^3; and (*9*) Al/Tf 25/75 of a density of 0.54 g/cm^3; as well as for the compositions (*10*) $Al/S/Fe_2O_3$ 55/33/12 of a density of 0.81 g/cm^3 and (*11*) Al/MoO_3 45/55 of a density of 1.138 g/cm^3. The curves are the exponential extrapolations of the results.

In addition to experiments with low-density mixtures, we performed experiments with compressed Al/Tf samples with a porosity of about 5%. The experiments prove that the process rapidly decays in this case, which agrees qualitatively with the results of experiments on pressed samples of the Al/S and Al/MoO_3 mixtures [5].

Our results have demonstrated the possibility of reaching the steady detonation regime in the Al/Tf MAEC, in which the end products of detonation are in the condensed state. A detailed mechanism of the propagation of detonation in the mixtures under study remains unclear and requires further investigation.

Investigations of detonation in reactive mixtures forming solid end products will make it possible to deepen insight into the mechanisms of shock-induced physicochemical processes in condensed media. Moreover, these investigations will form the basis for obtaining a new type of energetic materials.

We are sincerely grateful to S.B. Viktorov (Moscow Engineering Physics Institute), who carried out thermodynamic calculations, to V.A. Borisenok and V.G. Simakov (Russian Federal Nuclear Center VNIIEF), who placed the PVDF gauges at our disposal, to A.K. Rogozinskiĭ (Semenov Institute of Chemical Physics, Russian Academy of Sciences), who measured the speed of sound in the mixtures, and to A.G. Merzhanov and Yu.A. Gordopolov (Institute of Structural Macrokinetics and Materials Science, Russian Academy of Sciences) for their interest in this study and for stimulating discussions.

This study was supported by the Russian Academy of Sciences (complex program "Thermal Physics and Mechanics of High-Power Effects") and by the Russian Foundation for Basic Research (project no. 03-03-32413-a). The work of V.E.F. was supported by the Max Planck Gesellschaft, Deutsche Forschungsgemeinschaft.

REFERENCES

1. Ya. B. Zel'dovich, Zh. Éksp. Teor. Fiz. **10**, 542 (1940).
2. A. F. Belyaev and A. B. Nalbandyan, Dokl. Akad. Nauk SSSR **46**, 113 (1945).
3. Yu. A. Gordopolov, V. S. Trofimov, and A. G. Merzhanov, Dokl. Akad. Nauk **341**, 327 (1995) [Phys. Dokl. **40**, 115 (1995)].
4. Yu. B. Khariton, in *Problems in the Theory of Explosives* (Akad. Nauk SSSR, Moscow, 1947), Book 1, p. 7 [in Russian].
5. A. Yu. Dolgoborodov, M. N. Makhov, M. F. Gogulya, *et al.*, in *Substances, Materials, and Constructions at Intense Dynamic Actions*, Ed. by A. L. Mikhaĭlov (Vser. Nauchno-Issled. Inst. Éksp. Fiz., Sarov, 2003), p. 273 [in Russian].
6. M. I. Aronov, Prib. Tekh. Éksp., No. 1, 153 (1959).
7. M. Schoenitz, T. Ward, and E. L. Dreizin, Mater. Res. Soc. Symp. Proc. **800**, AA2.6.1 (2004).
8. M. N. Makhov, Khim. Fiz. **19**, 83 (2000).
9. A. Yu. Dolgoborodov, M. N. Makhov, A. N. Streletskiĭ, *et al.*, Khim. Fiz. **23**, 85 (2004).
10. A. Yu. Dolgoborodov, M. N. Makhov, S. B. Viktorov, *et al.*, in *Physics of Extremal States of Substance-2004* (Chernogolovka, 2004), p. 82 [in Russian].
11. V. I. Pepekin and Yu. A. Lebedev, Dokl. Akad. Nauk SSSR **234**, 1391 (1977).

Translated by N. Wadhwa

JETP Letters, Vol. 81, No. 7, 2005, pp. 315–320. From Pis'ma v Zhurnal Éksperimental'noĭ i Teoreticheskoĭ Fiziki, Vol. 81, No. 7, 2005, pp. 399–404.

Damping Effects and the Metal–Insulator Transition in a Two-Dimensional Electron Gas¶

V. A. Khodel[1, *], M. V. Zverev[1], and J. W. Clark[2]

[1] *Russian Research Center Kurchatov Institute, Moscow, 123182 Russia*

**e-mail: vak@wuphys.wustl.edu*

[2] *McDonnell Center for the Space Sciences and Department of Physics, Washington University, St. Louis, MO 63130, USA*

Received February 24, 2005; in final form, March 9, 2005

The damping of single-particle degrees of freedom in strongly correlated two-dimensional Fermi systems is analyzed. Suppression of the scattering amplitude due to the damping effects is shown to play a key role in preserving the validity of the Landau–Migdal quasiparticle picture in a region of a phase transition associated with the divergence of the quasiparticle effective mass. The results of the analysis are applied to elucidate the behavior of the conductivity $\sigma(T)$ of the two-dimensional dilute electron gas in the density region where it undergoes a metal–insulator transition. © *2005 Pleiades Publishing, Inc.*

PACS numbers: 71.10.Hf, 71.27.+a

A quantitative understanding of the damping of single-particle excitations in a Fermi liquid (FL) is essential to the determination of the resistivity, thermal conductivity, and other kinetic properties of the system. When the temperature dependence of the properties of uncharged Fermi liquids is treated within Landau theory, the decay rate $\gamma(\varepsilon)$ of single-particle excitations at the relevant energies $\varepsilon \sim T$ is given by [1]

$$\gamma(T) = W(M^*)^3T^2. \quad (1)$$

Here, the effective mass M^* specifies the FL single-particle spectrum $\xi(p) \equiv \epsilon(p) - \mu = p_F(p - p_F)/M^*$, where $\epsilon(p) = \delta E_0/\delta n(p)$ and μ is the chemical potential. The factor W is proportional to the square of the scattering amplitude Γ, suitably averaged over the spins and momenta of incoming and outgoing particles.

Reliable experimental data on the modification of FL properties under the variation of controllable variables (e.g., the density n) exist only for two-dimensional (2D) Fermi systems, notably liquid ^{3}He and the electron gas. Landau theory adequately reproduces the behavior of these data in a broad density region, *except* in the vicinity of the critical density n_∞, where the effective mass diverges and the spectrum $\xi(p)$ becomes flat. This failure of FL theory is conventionally attributed to a strong enhancement of the dimensionless damping rate $r(T) = \gamma(T)/T$. Close to the critical point, $r(T)$ allegedly exceeds unity, invalidating the Landau–Migdal quasiparticle picture.

Here, we shall demonstrate that, in actuality, the parameter $r(T)$ remains rather small on both sides of the phase transition associated with the divergence of the effective mass in the 2D system, and, consequently, that the quasiparticle picture does apply. We then proceed to study kinetic phenomena within the quasiparticle formalism, while paying particular attention to the metal–insulator transition (MIT) occurring in the 2D electron gas in the density region where the effective mass diverges [2–4].

Our analysis is based on the standard formula for the damping rate [1, 5],

$$\gamma(\varepsilon) \sim -\sum_{\mathbf{p}_1, \mathbf{p}'} \iint W(\mathbf{p}, \mathbf{p}_1, \mathbf{p}', \mathbf{p}'_1; \varepsilon, \varepsilon_1, \omega) F(\varepsilon, \varepsilon_1, \omega, T) \times \mathrm{Im}G_R(\mathbf{p}_1, -\varepsilon_1)\mathrm{Im}G_R(\mathbf{p}', \varepsilon - \omega) \times \mathrm{Im}G_R(\mathbf{p}'_1, \omega - \varepsilon_1) d\varepsilon_1 d\omega, \quad (2)$$

where $\mathbf{p}$, $\mathbf{p}_1$ and $\mathbf{p}'$, $\mathbf{p}'_1$ are, respectively, the incoming and outgoing momentum pairs, and $\omega = \varepsilon - \varepsilon'$. The function W is given by the sum of absolute squares of the scalar (s) and spin-dependent (a) components Γ_s and Γ_a of the scattering amplitude $\Gamma = \Gamma_s + \Gamma_a\boldsymbol{\sigma}_1\boldsymbol{\sigma}_2$, while $F(\varepsilon, \varepsilon_1, \omega, T) = \cosh(\varepsilon/2T)[\cosh(\varepsilon_1/2T)\cosh((\varepsilon - \omega)/2T)\cosh((\omega - \varepsilon_1)/2T)]^{-1}$ and G_R is the retarded Green function. In what follows, we assume that the dependence of the mass operator $\Sigma(p, \varepsilon)$ on ε is not crucial, and, then,

$$\mathrm{Im}G_R(p, \varepsilon) = -\gamma(\varepsilon)/[(\varepsilon - \xi(p))^2 + \gamma^2(\varepsilon)]. \quad (3)$$

To begin, we note that, in collision integral (2), all the quasiparticle energies must lie close to the Fermi surface, so that $|\xi(p)| \le T$, $|\xi(p_1)| \le T$, and $|\xi(|\mathbf{p} - \mathbf{q}|)| \le T$, $|\xi(|\mathbf{p}_1 + \mathbf{q}|)| \le T$, since, as we shall see, broadening of the single-particle states is insignificant. In 2D, these con-

¶ This article was submitted by the authors in English.

ditions are easily met if (i) the momentum transfer $q = |\mathbf{p} - \mathbf{p}'|$ in the longitudinal particle–hole channel is small, i.e., $q \le q_c(T) = T(dp/d\xi)_T \sim TM^*/p_F$, or, equivalently, if (ii) the momentum transfer $q_1 = |\mathbf{p} - \mathbf{p}_1'|$ in the transverse particle–hole channel is small or (iii) the total momentum $P = |\mathbf{p} + \mathbf{p}_1|$ is close to zero. Outside these regions, contributions to the collision integral appear to be minor.

In dealing with small momentum transfers, we first address the scalar component Γ_s of the scattering amplitude Γ, which obeys the standard equation [5]

$$\Gamma_s(q, \omega) = f + f\Pi_0(q, \omega)\Gamma_s(q, \omega) \equiv [f^{-1} - \Pi_0(q, \omega)]^{-1}, \quad (4)$$

where f is the scalar part of the Landau interaction function. In FL theory, the polarization loop Π_0 is an integral over the product of two quasiparticle Green functions $G(p, \varepsilon) = (\varepsilon - \xi(p))^{-1}$, given by

$$\Pi_0(q, \omega) = 2\int \frac{n(\mathbf{p}) - n(\mathbf{p} - \mathbf{q})}{\xi(\mathbf{p}) - \xi(\mathbf{p} - \mathbf{q}) - \omega} d\nu, \quad (5)$$

in which $d\nu = d^2p/(2\pi)^2$ is the volume element in 2D momentum space and $n(p) = 1/[1 + \exp(\xi(p)/T)]^{-1}$ is the quasiparticle momentum distribution.

The value of Re Π_0 is of order $N(0)$, the density of states, proportional to M^*. In a strongly correlated FL obeying Landau theory, this quantity, whose sign depends on the ratio ω/q, is enhanced by the factor M^*/M compared to the corresponding ideal Fermi-gas value. On the other hand, at small ω and $q > q_{\min} = M^*\omega/p_F$, the imaginary part of $\Pi_0(q, \omega, T = 0)$, given by

$$\mathrm{Im}\Pi_0(q, \omega, T = 0) \simeq -\frac{\omega(M^*)^2}{\pi q p_F \sqrt{1 - (M^*\omega/qp_F)^2}}, \quad (6)$$

has the same order as Re Π_0. Thus, in strongly correlated systems, f^{-1} can be neglected, and Eq. (4) reduces to $|\Gamma_s(q \sim q_c, \omega \sim T)| \simeq N^{-1}(0)$ [6].

A similar situation applies for the spin-dependent part Γ_a of the scattering amplitude Γ, which satisfies the same Eq. (4) with the replacement $f \longrightarrow f_a$, where f_a is the spin-dependent part of the Landau interaction function. The 2D Fermi systems in question do not exhibit ferromagnetism, in spite of the negative sign of f_a derived from experimental data on the spin susceptibility. This means that the Pomeranchuck stability condition [1] $1 + f_aN(0) > 0$ is not violated, implying that $|f_aN(0)| < 1$ holds even if the enhancement of the effective mass is large. The estimate $|\Gamma_a(q \sim q_c, \omega \sim T)| \le N^{-1}(0)$ follows straightforwardly. In the transverse particle–hole channel, where small momentum transfer corresponds to $q \simeq 2p_F$, the situation is evidently the same, so that, in collision term (2), integration over q can be restricted to the region of small q, and the result is doubled.

In the third relevant momentum region where the total momentum P is small, the scattering amplitude $|\Gamma(P \longrightarrow 0)| \simeq -1/[N(0)\ln P^2]$ contains an additional suppression factor $1/\ln P^2$ due to the BCS logarithmic divergence of the particle–particle propagator [5]. Therefore, in what follows the respective contribution will be neglected. Thus, we conclude that a proper treatment of damping effects in the strongly correlated system leads to substantial suppression of the interaction factor W governing damping rate (2).

In the foregoing analysis, the momentum dependence of the Landau interaction function $\mathcal{F} = f + f_a\boldsymbol{\sigma}_1\boldsymbol{\sigma}_2$ has been neglected. Upon its inclusion, relation (4) is replaced by the integral equation

$$\Gamma(\mathbf{nn}_1, q, \omega) = \mathcal{F}(\mathbf{nn}_1) + \Pi_0(q, \omega)\int \mathcal{F}(\mathbf{nn}')\Gamma(\mathbf{n}'\mathbf{n}_1, q, \omega)d\varphi'/2\pi, \quad (7)$$

with $\mathbf{n} = \mathbf{p}/p_F$ and $\mathbf{n}_1 = \mathbf{p}_1/p_F$. We now make use of the smallness of the quantity $1/\Pi_0 \sim M/M^*$ and rewrite the scattering amplitude as

$$\Gamma(\mathbf{nn}_1, q, \omega) = X(\mathbf{nn}_1)/\Pi_0(q, \omega). \quad (8)$$

Neglecting small corrections, Eq. (7) becomes

$$0 = \mathcal{F}(\mathbf{nn}_1) + \int \mathcal{F}(\mathbf{nn}')X(\mathbf{n}'\mathbf{n}_1)d\varphi'/2\pi. \quad (9)$$

Inserting expression (8) into collision formula (2), standard algebra [7] converts it to

$$\gamma(\varepsilon \sim T) \sim \int_0^{\varepsilon \sim T}\int_{q_{\min}}^{q_c}\int X^2(\mathbf{nn}_1)\frac{\mathrm{Im}\Pi_0(q, \omega)}{|\Pi_0(q, \omega)|^2} \times \mathrm{Im}G_R(\mathbf{p} - \mathbf{q}, \varepsilon - \omega)d\omega q dq d\varphi, \quad (10)$$

where $\mathrm{Im}G_R(p, \varepsilon)$ is given by Eq. (3). In the 2D dilute electron gas where $X = 1$, this result practically coincides with that derived in [7]. As usual [8], integration over angles in Eq. (10) is replaced by integration over energies $\xi(l)$ where $\mathbf{l} = \mathbf{p} - \mathbf{q}$, and, after some algebra, we arrive at [7]

$$\gamma(T) \sim \frac{T^2M^*}{M\varepsilon_F^0}\ln\left(\frac{M^*T}{M\varepsilon_F^0}\right). \quad (11)$$

The same estimate is valid for other strongly correlated 2D Fermi systems where the spectrum $\xi(p)$ is specified only by the effective mass.

Result (10) holds in the density region where the effective mass M^* diverges, since in its derivation only relation (8) has been employed. Here, at relevant q, ω, the value of $\mathrm{Re}\Pi_0(q, \omega)$ turns out to be of order

$(dp/d\xi)_{\xi \simeq T}$. As for $\mathrm{Im}\Pi_0(q, \omega)$, its value is evaluated on the basis of the general formula [5]

$$\mathrm{Im}\Pi_0(q, \omega) = \iint\left[\tanh\frac{\varepsilon-\omega}{2T} - \tanh\frac{\varepsilon}{2T}\right] \times \mathrm{Im}G_R(\mathbf{p}-\mathbf{q}, \varepsilon-\omega)\mathrm{Im}G_R(\mathbf{p}, \varepsilon)\frac{d\varepsilon}{\pi}d\nu. \quad (12)$$

Insertion of the explicit form of $\mathrm{Im}G_R$ and integration over $\xi(p)$, $\xi(l)$ along the same lines, as before, gives

$$\mathrm{Im}\Pi_0(q, \omega) \sim \frac{p_F}{q}\int\left[\tanh\frac{\varepsilon-\omega}{2T} - \tanh\frac{\varepsilon}{2T}\right]\left(\frac{dp}{d\xi}\right)_T^2 d\varepsilon, \quad (13)$$

where the product $(dp/d\xi)_{\xi=\varepsilon}(dp/d\xi)_{\xi=\varepsilon-\omega}$ has been replaced by $(dp/d\xi)_T^2$. As a result, one finds

$$|\mathrm{Im}\Pi_0(q, \omega \sim T)| \sim \frac{Tp_F}{q}\left(\frac{dp}{d\xi}\right)_T^2. \quad (14)$$

Upon inserting this result into Eq. (10), we are led to

$$\gamma(T) \sim \frac{T^2}{p_F}\left(\frac{dp}{d\xi}\right)_T \ln\left[\frac{T}{p_F}\left(\frac{dp}{d\xi}\right)_T\right]. \quad (15)$$

Thus, for evaluation of the damping rate $\gamma(T)$ in the density region where M^* diverges, one needs to know the spectrum $\xi(p)$ close to the Fermi surface. To date, microscopic calculations in this density region have been performed only for the electron gas in 2D and 3D and only at $T = 0$ [9–11]. In Fig. 1, we display results for the spectrum $\xi(p)$ of the 2D electron gas, calculated at $T = 0$ within a functional approach [12]. Close to the Fermi surface, the electron spectrum $\xi(p, n_\infty)$, given in Fig. 1, behaves as $(p - p_F)^3$. The leading FL term reemerges at finite temperatures [13], so that

$$\xi(p, T, n_\infty) = p_F(p-p_F)/M^*(T, n_\infty) + \xi_3(p-p_F)^3, \quad (16)$$

with the effective mass [14] going like $M^*(T, n_\infty) \sim (dp/d\xi)_T \sim T^{-2/3}$. With this result, the damping rate evaluated with the help of Eq. (15) becomes $\gamma(T, n_\infty) \sim T^{4/3}\ln(\varepsilon_F^0/T)$.

The critical single-particle spectrum $\xi(p, T = 0, n_\infty) \sim (p - p_F)^3$ is not universal. In a broader context, the Landau state is known (e.g., from [15, 16]) to lose its stability at a density n_b for which a bifurcation point $p = p_b$ emerges in the equation

$$\xi(p, T = 0, n_b) = 0, \quad (17)$$

which ordinarily has only the single root $p = p_F$. The particular form $\xi(p, T = 0, n_\infty) \sim (p - p_F)^3$ corresponds to the case in which the bifurcation point p_b coincides with p_F. Obviously, in the general case, one has $p_b \neq p_F$, and the Landau state loses its stability before M^* becomes infinite. If the distance between p_b and p_F is small, then the single-particle spectrum has the form

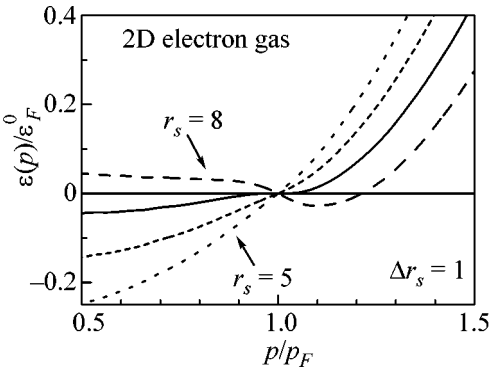

Fig. 1. Single-particle spectrum $\xi(p)$ of the homogeneous two-dimensional electron gas in units of $\varepsilon_F^0 = p_F^2/2M$, evaluated at $T = 0$ for different values of $r_s = (\pi n)^{-1/2}/a_B$, where a_B is the Bohr radius.

$$\xi(p, T = 0, n_b) \sim (p - p_b)^2(p - p_F). \quad (18)$$

Suppose the temperature T lies below the maximum value ξ_m of $|\xi(p, T = 0, n_b)|$ in the momentum interval $[p_b, p_F]$. In this case, the dominant contributions to the properties of interest come from the momentum region adjacent to the bifurcation point p_b, where, according to Eq. (18), $(dp/d\xi)_T \sim T^{-1/2}$. From this result and Eq. (15), one obtains $\gamma(T, n_b) \sim T^{3/2}\ln(\varepsilon_F^0/T)$.

Beyond the critical density n_b, Eq. (17) possesses two additional roots $p_1 < p_b < p_2$. The single-particle spectrum $\xi_{FL}(p, T = 0, n)$, evaluated with the Landau momentum distribution $n_{FL}(p) = \theta(p_F - p)$, has the form

$$\xi_{FL}(p, T = 0, n) \sim (p - p_1)(p - p_2)(p - p_F). \quad (19)$$

If $p_b \neq p_F$, the roots p_1, p_2 are both located either in the interior of the Fermi sphere or both outside it. If $p_b = p_F$, then $p_1 < p_F < p_2$. In all these cases, the Landau occupation numbers $n_L(p)$ are rearranged. As a rule, the Fermi surface becomes multiconnected, but the quasiparticle occupation numbers $n(p)$ continue to take values 0 or 1. Hence, the Landau–Migdal quasiparticle picture holds, with $n(\xi) = 1$ for $\xi < 0$ and 0 otherwise. Consider first the case $p_1 < p_2 < p_F$. Then, according to Eq. (19), the single-particle states remain filled in the intervals $p < p_1$ and $p_2 < p < p_F$, while the states corresponding to $p_1 < p < p_2$ are empty. We call this new phase the bubble phase. If the bifurcation point p_b coincides with the Fermi momentum p_F, then $p_1 < p_F$ and $p_2 < p_F$, and the states with $p < p_1$ and with $p_F < p < p_2$ are occupied, while those for $p_1 < p < p_F$ are empty. Again, one deals with the bubble phase.

At this point, we observe that solution (19) is not self-consistent, since the spectrum is evaluated with

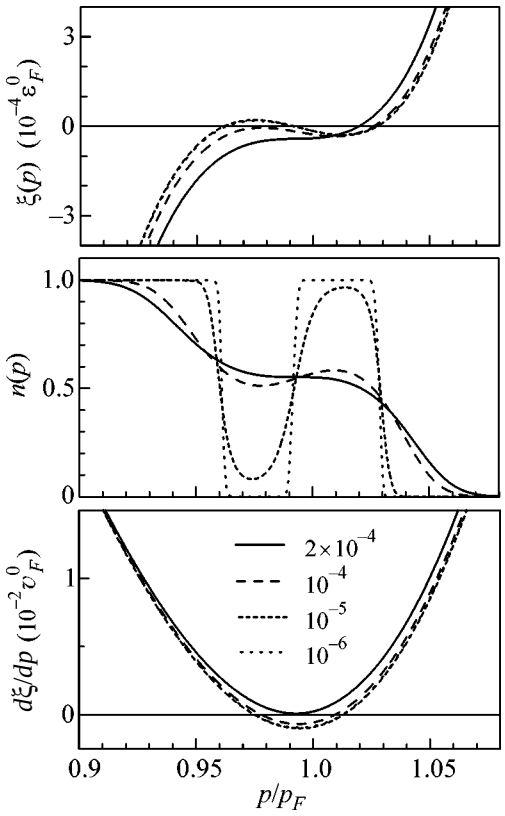

Fig. 2. Single-particle spectrum $\xi(p)$ in units of $10^{-4}\varepsilon_F^0$ (top panel), occupation numbers $n(p)$ (middle panel), and $d\xi/dp$ in units of $10^{-2}v_F^0$, where $v_F^0 = p_F/M$ (bottom panel), plotted versus p/p_F at four line-type-coded temperatures relevant to the bubble phase, in units of ε_F^0. Model (21) is assumed with parameters $\beta = 0.48$ and $\lambda = 3N_0$, where $N_0 = p_F M/\pi^2$.

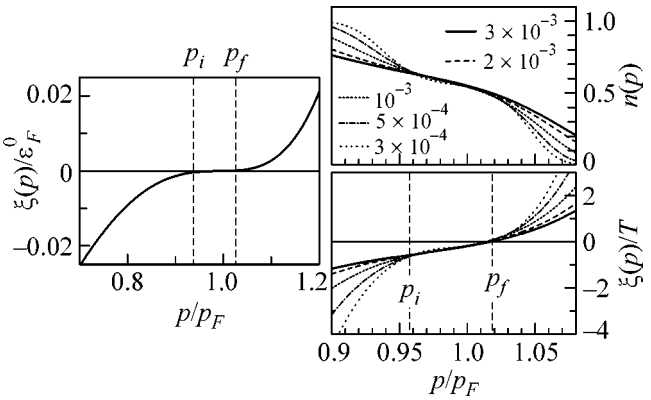

Fig. 3. Single-particle spectrum $\xi(p)$ in units of ε_F^0 at the critical temperature $T_Z = 3\times10^{-4}\varepsilon_F^0$ (left panel), occupation numbers $n(p)$ (right-top panel), and $\xi(p)/T$ (right-bottom panel), plotted versus p/p_F at five line-type-coded temperatures relevant to the phase with a FC, in units of ε_F^0. Model (21) is assumed.

$n_{FL}(p)$, while the true Fermi surface is doubly connected. Following [15], we consider the feedback of the rearrangement of $n_{FL}(p)$ on the spectrum $\xi(p)$ in the bubble phase based on the Landau relation [5]

$$\frac{\partial\epsilon(p)}{\partial\mathbf{p}} = \frac{\mathbf{p}}{M} + \int f(\mathbf{p},\mathbf{p}_1)\frac{\partial n(p_1)}{\partial\mathbf{p}_1}dv_1, \qquad (20)$$

where, as before, f is the scalar part of the Landau interaction function and $n(p) = [1 + \exp(\xi(p)/T)]^{-1}$ is the quasiparticle momentum distribution. The solutions of this nonlinear integral equation are known only in 3D Fermi systems with phenomenological functions f depending on $q = |\mathbf{p} - \mathbf{p}_1|$. Despite the diversity of forms assumed for $f(q)$, the resulting single-particle spectra and momentum distributions bear a close family resemblance. Figures 2 and 3 display results from the solution of Eq. (20) for the function

$$f(q) = \lambda/[((q/2p_F)^2 - 1)^2 + \beta^2]. \qquad (21)$$

Let us briefly summarize how solutions of Eq. (20) evolve under variations of T. When the bubble range $p_2 - p_1$ is small, then heating to $T \sim T_{FL} = (p_2 - p_1)^2/M$ results in its dissolution (see Fig. 2). With a further increase in T, the function $\xi(p)$ becomes smoother, and, in the region of a new critical temperature T_Z, a flat portion $\xi \simeq 0$ appears in the spectrum over an interval $[p_i, p_f]$ surrounding the Fermi momentum p_F, as shown in the left panel of Fig. 3. Since $\xi(p) = \epsilon(p) - \mu$ and $\epsilon(p) = \delta E_0/\delta n(p)$, the equality $\xi = 0$ can be rewritten as a variational condition [17]:

$$\frac{\delta E_0}{\delta n(p)} = \mu, \quad p_i < p < p_f, \qquad (22)$$

with $E_0 = \sum_{\mathbf{p}} \epsilon_{\mathbf{p}}^0 n(\mathbf{p}) + \frac{1}{2}\sum_{\mathbf{p},\,\mathbf{p}_1} f(\mathbf{p} - \mathbf{p}_1)n(\mathbf{p})n(\mathbf{p}_1)$ and $\epsilon_{\mathbf{p}}^0 = p^2/2M$. The solution $n_0(p)$ of Eq. (20) or, equivalently, of Eq. (22), is a continuous function of p with a nonzero derivative dn_0/dp (see Fig. 3, top-right panel). The set of single-particle states with $\xi(p) = 0$ is called the fermion condensate (FC), since the corresponding density of states $\rho(\varepsilon)$ contains a Bose-liquid-like term $\eta n\delta(\varepsilon)$. The dimensionless constant $\eta \simeq (p_f - p_i)/p_F$ is naturally identified as a characteristic parameter of the FC phase.

It has been demonstrated [18] that the FC "plateau" in $\xi(p)$ has a small slope, evaluated by inserting $n_0(p)$ into the above Fermi–Dirac formula for $n(\xi)$ to yield

$$\xi(p, T \geq T_Z) = T\ln\frac{1 - n_0(p)}{n_0(p)}, \quad p_i < p < p_f. \qquad (23)$$

As indicated in the bottom-right panel of Fig. 3, at $T \geq T_Z$ the ratio $\xi(p)/T$ is indeed a T-independent function of p in the FC region. The presence of this flat portion of $\xi(p) \sim T$ is a signature of the phenomenon called fermion condensation [17–19]. The width $\xi(p_f) - \xi(p_i) \equiv$

$\xi_f - \xi_i$ of the FC "band" appears to be of order T, almost independently of $\eta > \eta_{\min} \sim 10^{-2}$. Thus, at $\eta > \eta_{\min}$, the FC group velocity is estimated as

$$\left(\frac{d\xi(p)}{dp}\right)_T \sim \frac{T}{\eta p_F}, \quad p_i < p < p_f. \tag{24}$$

As shown in [10], the effective mass diverges before attaining the critical point r_{CDW} for the charge-density-wave instability. Microscopic calculations confirm this assertion: M^* diverges at $r_s = r_\infty \simeq 7$, while the condensate of the charge-density waves occurs at $r_{\mathrm{CDW}} \simeq 10$. Thus, in the interval $r_\infty < r_s < r_{\mathrm{CDW}}$, one deals with the homogeneous ground state having a FC. In this case, the damping rate of single particle excitations is evaluated on the basis of Eqs. (15) and (24), yielding

$$\gamma(T) \sim \eta T \ln(1/\eta). \tag{25}$$

Thus, as long as the FC density remains small, the dimensionless damping rate $r(T) = \gamma(T)/T$ proves to be small as well, so the presence of the FC does not destroy the quasiparticle picture. It is worth noting that, at greater energies $\varepsilon \gg T$, the damping $\gamma(\varepsilon)$ grows as $\sqrt{\varepsilon}$ with increasing ε [20]. Thus, at these energies, the ratio $\gamma(\varepsilon)/\varepsilon$ exceeds unity, and the quasiparticle picture fails independently of the η value.

Let us now apply our results to the elucidation of the behavior of the conductivity of a dilute 2D electron gas from data obtained in samples with silicon inversion layers [2, 4]. We focus our attention on low densities, where the 2D electron gas undergoes a metal–insulator transition (MIT), as signaled by a change in sign of the derivative $d\rho(T \longrightarrow 0)/dT$. In high-quality samples, the sign change occurs at the density $n_{\mathrm{MIT}} \simeq 0.9 \times 10^{11}$ cm^{-2}. On the metallic side of the MIT, this derivative has a positive sign, while, on the insulating side, it is negative, the separatrix $\rho_{\mathrm{MIT}}(T) \simeq 3h/e^2 \simeq 75\ k\Omega$ between the two phases being almost horizontal [2, 4].

At these densities, the electron–electron interaction, first taken into account within perturbation theory in [21], becomes a "play maker." A crucial point is that, close to the critical density n_{MIT}, the effective mass $M^*(n)$ diverges [2, 4]. In this situation, a standard method of the treatment of kinetic phenomena on the basis of the Boltzmann equation fails. Therefore, we employ a different approach where the conductivity $\sigma(T)$ is expressed in terms of the imaginary part of the polarization operator $\Pi(\mathbf{j}, \omega \longrightarrow 0, T)$ through [5]

$$\sigma(T) \sim -\lim_{\omega \to 0} \omega^{-1} \mathrm{Im}\Pi(\mathbf{j}, \omega, T). \tag{26}$$

This provides contributions of two different types, namely, from (i) imaginary parts of the quasiparticle Green functions and (ii) imaginary parts of the scattering amplitudes. As a rule, both of these contributions provide the same T dependence of $\sigma(T)$. For example, this is seen in homogeneous systems without impurities, where the two types of contributions cancel each other to ensure vanishing of the resistivity due to momentum conservation. (In solids, the resistivity $\rho(T)$ differs from 0 due to Umklapp processes.) Such a cancellation allows one to find the T dependence of the resistivity in the critical density region, where the spectrum $\xi(p)$ becomes flat, by retaining in Eq. (26) only contributions coming from $\mathrm{Im}G_R$. Thereby, the calculations are simplified considerably, and the expression for $\mathrm{Im}\Pi$ acquires the form

$$\mathrm{Im}\Pi(\mathbf{j}, \omega \longrightarrow 0, T) \sim \iint \left(\tanh\frac{\varepsilon - \omega}{2T} - \tanh\frac{\varepsilon}{2T}\right) \times |\mathcal{T}(\mathbf{j}, \omega = 0)|^2 \mathrm{Im}G_R(\mathbf{p}, \varepsilon - \omega)\mathrm{Im}G_R(\mathbf{p}, \varepsilon) d\varepsilon d\nu. \tag{27}$$

Here, $\mathcal{T}$ is the vertex part, whose static limit is given by [5] $\mathcal{T}(\mathbf{j}, \omega = 0) = e\partial\xi(p)/\partial\mathbf{p}$. Upon inserting the explicit form for $\mathrm{Im}G_R$ into Eqs. (27) and (26), the latter becomes [22]

$$\sigma(T) = 2e^2 \iint \frac{(d\xi/dp)^2 \gamma^2(\varepsilon) d\varepsilon d\nu}{2T[(\varepsilon - \xi(p))^2 + \gamma^2(\varepsilon)]^2 \cosh^2(\varepsilon/2T)}. \tag{28}$$

Converting, as before, the momentum integration to an integration over ξ and taking into account that the overwhelming contributions to this integral come from the vicinity of the point $\xi = \varepsilon$, we arrive at

$$\sigma(T) = 2\pi \frac{ne^2}{p_F} \int \frac{(d\xi/dp)}{2T\gamma(\xi)\cosh^2(\xi/2T)} d\xi, \tag{29}$$

where $n = p_F^2/2\pi$. Remembering that, in the region of the critical density of a 2D electron gas, where the effective mass diverges, one has $\gamma(T) \sim T^{4/3}\ln(\varepsilon_F^0/T)$; then, Eq. (29) gives

$$\sigma(T) \sim T^{-2/3}/\ln(\varepsilon_F^0/T). \tag{30}$$

Since $d\sigma(T \longrightarrow 0)/dT < 0$, this point is situated on the metallic side of the MIT. Beyond this density, i.e., at $r_\infty < r_s < r_{\mathrm{CDW}}$, and at greater but still very low temperatures $T \sim T_Z$, we pass the point of fermion condensation. The FC contribution to $\sigma(T)$ is evaluated with the help of Eqs. (25) and (24), yielding

$$\sigma_{FC}(T) = \sigma_0 e^2/\eta^2 \ln(1/\eta), \tag{31}$$

where σ_0 is a T-independent constant.

At $r_s > r_{\mathrm{CDW}}$, the spontaneous generation of the condensate of the charge-density waves occurs, and the ground state of the 2D electron gas becomes nonhomogeneous. Consequently, a gap in the single-particle spectrum opens, which results in an exponential decline of the conductivity $\sigma(T)$ at $T \longrightarrow 0$, implying that one is dealing with the insulating side of the MIT. Thus, the separatrix dividing the metallic and insulating domains is situated in the FC region, and, according to Eq. (31),

it is a straight line. This result is in agreement with available experimental data [2–4].

Flattening of the single-particle spectrum entails a change of the Hall coefficient $R_H = \sigma_{xyz}/\sigma_{xx}^2$ [23]. In homogeneous matter at $H \longrightarrow 0$, $\sigma_{xx} = \sigma/3$, with σ given by Eq. (29), while σ_{xyz} is recast as

$$\sigma_{xyz} = \frac{e^3}{3c\gamma^2}\int\left(\frac{d\xi}{dp}\right)^2\frac{\partial n(\xi)}{\partial\xi}d\xi, \qquad (32)$$

where $n(\xi)$ is the Fermi–Dirac distribution function. Far from the critical density n_∞, these formulas lead to the standard result $R_H = 1/nec$. The critical spectrum of 2D electron gas has the form $\xi(p, n_\infty, T = 0) \sim (p - p_F)^3$, and, with the help of Eqs. (29) and (32), one then finds $R_H = K/nec$, where

$$K(n_\infty, T \longrightarrow 0, H \longrightarrow 0) = \frac{\int z^{4/3}e^z[1 + e^z]^{-2}dz}{\left(\int z^{2/3}e^z[1 + e^z]^{-2}dz\right)^2} \simeq 1.5. \qquad (33)$$

We see that, at the critical density, the effective volume of the Fermi sphere considerably shrinks. It is important that, even quite close to the critical point where the effective mass still remains finite, the value $K = 1$ holds, so that, at low T, critical behavior (33) of K emerges abruptly. On the other hand, imposition of a static magnetic field H on the system at the critical density n_∞ renders the effective mass finite [13, 14], and, hence, one can expect an abrupt change in the Hall coefficient $R_H(n_\infty, T \longrightarrow 0, H)$ as a function of H.

In conclusion, we have analyzed damping effects in a strongly correlated 2D Fermi liquid in a density region where the effective mass diverges. We have demonstrated that, in spite of the enhancement of the dimensionless constants specifying the strength of the effective interaction between quasiparticles, the Landau–Migdal quasiparticle picture is applicable on both sides of the phase transition associated with the divergence of the effective mass. The results of the analysis have been applied to the interaction-driven metal–insulator transition in the 2D electron gas, demonstrating that the separatrix between the metallic and insulating regions is a straight line.

We thank V.T. Dolgopolov, V.M. Galitski, A.A. Shashkin, and V.M. Yakovenko for valuable discussions. This research was supported by NSF grant no. PHY-0140316 (JWC and VAK), by the McDonnell Center for the Space Sciences (VAK), and by grant no. NS-1885.2003.2 from the Russian Ministry of Education and Science (VAK and MVZ).

REFERENCES

1. D. Pines and P. Nozieres, *Theory of Quantum Liquid* (Benjamin, New York, 1966), Vol. 1.
2. S. V. Kravchenko and M. P. Sarachik, Rep. Prog. Phys. **67**, 1 (2004).
3. Y. Tsui, S. A. Vitkalov, and M. P. Sarachik, cond-mat/0406566.
4. A. A. Shashkin, cond-mat/0405556.
5. A. A. Abrikosov, L. P. Gor'kov, and I. E. Dzyaloshinski, *Methods of Quantum Field Theory in Statistical Physics* (Prentice-Hall, London, 1963).
6. V. A. Khodel and P. Schuck, Z. Phys. B **104**, 503 (1997).
7. G. F. Giuliani and J. J. Quinn, Phys. Rev. B **26**, 4421 (1982).
8. A. B. Migdal, Zh. Éksp. Teor. Fiz. **34**, 1438 (1958) [Sov. Phys. JETP **7**, 996 (1958)].
9. M. V. Zverev, V. A. Khodel, and V. R. Shaginyan, JETP **82**, 567 (1996).
10. V. A. Khodel, V. R. Shaginyan, and M. V. Zverev, JETP Lett. **65**, 253 (1997).
11. Y. Zhang, V. M. Yakovenko, and S. Das Sarma, cond-mat/0410039.
12. V. A. Khodel, V. R. Shaginyan, and V. V. Khodel, Phys. Rep. **249**, 1 (1994).
13. V. R. Shaginyan, JETP Lett. **79**, 286 (2004).
14. J. W. Clark, V. A. Khodel, and M. V. Zverev, Phys. Rev. B **71**, 012401 (2005).
15. M. V. Zverev and M. Baldo, JETP **87**, 1129 (1998); J. Phys.: Condens. Matter **11**, 2059 (1999).
16. M. Baldo *et al.*, J. Phys.: Condens. Matter **16**, 6431 (2004).
17. V. A. Khodel and V. R. Shaginyan, JETP Lett. **51**, 553 (1990); Condens. Matter Theor. **12**, 221 (1997).
18. P. Nozières, J. Phys. I **2**, 443 (1992).
19. G. E. Volovik, JETP Lett. **53**, 222 (1991).
20. V. A. Khodel and M. V. Zverev, JETP Lett. **74**, 502 (2001).
21. G. Zala, B. N. Narozhny, and I. L. Aleiner, Phys. Rev. B **64**, 214 204 (2001).
22. P. Vorugani, A. Golubentsev, and S. John, Phys. Rev. B **45**, 13 945 (1992).
23. M. R. Norman, Q. Si, Ya. B. Bazaliy, and R. Ramazashvili, Phys. Rev. Lett. **90**, 116601 (2002).

JETP Letters, Vol. 81, No. 7, 2005, pp. 321–325. Translated from Pis'ma v Zhurnal Éksperimental'noĭ i Teoreticheskoĭ Fiziki, Vol. 81, No. 7, 2005, pp. 405–409.

Quantum Analogue of the Spin-Flop Transition for a Spin Pair

B. A. Ivanov and V. E. Kireev

Institute of Magnetism, National Academy of Sciences of Ukraine and Ministry of Education and Science of Ukraine, Kiev, 03142 Ukraine

e-mail: kireev@imag.kiev.ua

Received December 6, 2004

Quantum (step) magnetization curves have been analyzed for a spin pair with antiferromagnetic interaction in the presence of a magnetic field that is parallel to the easy magnetization axis. Both semiclassical and numerical analyses have been performed for a wide range of the anisotropy parameter and spins up to $S \gtrsim 100$. In the dependence of the anisotropy character (single-ion or exchange), a spin jump larger than unity can appear in the magnetization curve or jumps can be concentrated in a narrow range of the field. In addition, regions of the problem parameters have been revealed where behavior is semiclassical for low spins on the order of $S = 5$ and where behavior is substantially quantum even for $S \longrightarrow \infty$. © *2005 Pleiades Publishing, Inc.*

PACS numbers: 75.30.Kz, 75.50.Ee, 75.60.Ej

Magnetic systems whose total spin S is high but that exhibit quantum effects associated with a finite spin have been extensively studied in the last decade. Among such systems are high-spin molecules with $S \sim 10$, magnetic clusters with $S \sim 100$, and magnetic dots (small magnetic particles 50–100 nm in size) [1, 2]. The existence of objects that manifest quantum properties on a macroscopic (more precisely, mesoscopic) scale is important for both the fundamental physics of magnetism and its applications such as quantum computers [3, 4] and information recording devices [1]. The simplest quantum effect that is manifested in such systems is directly associated with the quantization of the projection of the total system spin. This effect is stepwise magnetization under continuous variation of the external magnetic field [1, 2]. Such behavior is observed for many systems with prevailing antiferromagnetic interaction [5]. Among such systems, spin pairs with antiferromagnetic interaction, including pairs of high-spin Mn_4 molecules with the maximum total spin $2S = 9$ [6, 7], are most studied. However, measurements were also carried out for spin triplets, quartets, etc. [5, 8]. The method of magnetization jumps appeared to be useful for experimental determination of the material constants [5].

For realization of this method, it is important that the quantum problem that includes only isotropic exchange and an external field, i.e., when $B = 0$ and $\kappa = 0$ in Hamiltonian (1) presented below, has an exact solution for any spin. In this case, states with a given total spin S and its projection S^z are the eigenstates of the Hamiltonian, and the maximum S^z value $S^z = S$ corresponds to the minimum energy for a given S value. The energy of states is given by the expression $E(S, S^z) = JS(S + 1)/2 - g\mu_B HS^z$, S^z changes stepwise from $S^z = n - 1$ to $S^z = n$ for the field $H_n = Jn/g\mu_B$, and the complete saturation is reached at $H = H_{ex}$, where the exchange field is $H_{ex} = 2JS/g\mu_B$. Other exactly solvable models for clusters with antiferromagnetic interaction were discussed in [8]. In the presence of magnetic anisotropy, the quantum problem has no exact solution, excluding the Ising model, which corresponds to $\kappa = 1$ and $B = 0$ in Hamiltonian (1). In the latter case, which is classical in essence, $S^z = 0$ for $H < H_{ex}$ and the state is saturated, i.e., $S^z = 2S$, for $H > H_{ex} = JS/g\mu_B$.

We analyze the change in the magnetization of a spin pair with antiferromagnetic interaction and uniaxial anisotropy in the presence of a magnetic field parallel to the easy antiferromagnetic axis. The magnetization curve appeared to be more complicated than for the purely exchange case: jumps can be inequidistant, and their value ΔS^z can exceed unity. The behavior of the magnetization curve for single-ion anisotropy differs from that for exchange anisotropy. The behavior of the spin pair is similar to that for a macroscopic antiferromagnet near the spin-flop transition. This similarity can be suitable for qualitative estimate of the behavior of the system. A field range is found where deviations from the semiclassical behavior are not small even in the $S \longrightarrow \infty$ limit.

Quantum model and its semiclassical analysis. The Hamiltonian of a pair of spins $\mathbf{S}_1$ and $\mathbf{S}_2$ with antiferromagnetic interaction, which is described by the exchange integral $J > 0$, and uniaxial anisotropy in the external magnetic field $\mathbf{H}$ that is directed along the easy z axis is represented in the form

$$\begin{aligned}\mathcal{H} &= J[S_1^z S_2^z + (1 - \kappa)\mathbf{S}_1^\perp \mathbf{S}_2^\perp] \\ &- \frac{B}{2}[(S_1^z)^2 + (S_2^z)^2] - g\mu_B H(S_1^z + S_2^z).\end{aligned} \quad (1)$$

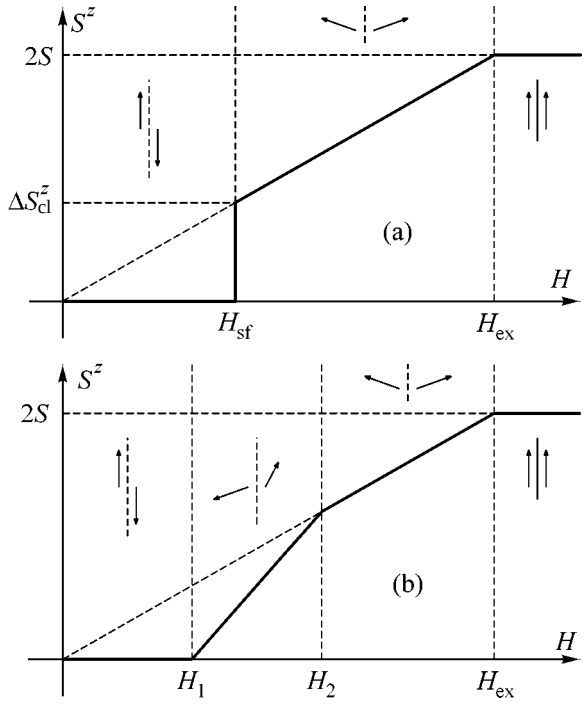

Fig. 1. Schematic field dependence of the ground state of the classical antiferromagnet with exchange and single-ion anisotropies when (a) single-ion or (b) exchange anisotropy prevails. The arrows are the directions of spins.

Here, both single-ion anisotropy with constant B and exchange anisotropy with constant κJ are taken into account. We start with the classical analysis of the problem. Treating the operators $\mathbf{S}_1$ and $\mathbf{S}_2$ as classical vectors (sublattice spins) of a macroscopic antiferromagnetic sample, we arrive at a suitable analogue of the problem of the spin-flop transition [9–11]. We introduce a unit vector $\mathbf{l} = (\mathbf{S}_1 - \mathbf{S}_2)/|\mathbf{S}_1 - \mathbf{S}_2|$. In terms of the angular variables, $l_z = \cos\theta$ and $l_x + il_y = \sin\theta\exp(i\phi)$. Excluding the total spin vector $\mathbf{S}_{\rm tot} = \mathbf{S}_1 + \mathbf{S}_2$ by means of the relation

$$\mathbf{S}_{\rm tot} = \frac{2g\mu_{\rm B}H(\mathbf{e}^z - \mathbf{l}\cdot\cos\theta)}{J(2-\kappa+\beta\cos2\theta)}, \qquad (2)$$

where $\beta = B/J$ and $\mathbf{e}^z$ is the unit vector along the symmetry axis (for details, see [11]), we write the energy $\mathcal{W}(\theta)$ of the antiferromagnet in the form

$$\mathcal{W}(\theta) = -\frac{(g\mu_{\rm B}H)^2\sin^2\theta}{J(2-\kappa+\beta\cos2\theta)} + J(\kappa+\beta)S^2\sin^2\theta. \qquad (3)$$

In the absence of the field, we arrive at the standard result: both exchange and single-ion anisotropies make an additive contribution to the effective magnetic anisotropy $(\kappa+\beta)JS^2\sin^2\theta$, which is of easy-axis character for $\kappa+\beta > 0$. The minimization of this energy for $H \neq 0$ shows that various phases can exist. The collinear phase $\Phi_\parallel$ is stable for $H < H_1$, and $S^z = 0$ and $\theta = 0$ or π in it. In the spin-flop phase $\Phi_\perp$, which is stable for $H > H_2$, $\theta = \pm\pi/2$ and the spin projection is linearly related to the field: $S^z = 2SH/H_{\rm ex}$. For $H \geq H_{\rm ex} = JS(2-\kappa-\beta)/g\mu_{\rm B}$, the state is saturated and $S^z = 2S$. The characteristic fields at which the phases lose stability are given by the expressions

$$H_1 = \frac{JS}{g\mu_{\rm B}}\sqrt{(2-\kappa+\beta)(\kappa+\beta)}, \quad H_2 = \frac{H_1^2}{H_{\rm sf}}, \qquad (4)$$

$$H_{\rm sf} = \frac{JS}{g\mu_{\rm B}}\sqrt{(2-\kappa-\beta)(\kappa+\beta)}. \qquad (5)$$

We note that the expression for the exchange field in the absence of single-ion anisotropy coincides with the saturation field for the exactly solvable Heisenberg and Ising quantum problems.

If anisotropy is purely exchange, i.e., $\beta = 0$, the critical fields H_1 and H_2 coincide with each other and a degenerate case arises. If $\beta > 0$, the transition from the collinear state $\Phi_\parallel$ to the spin-flop state $\Phi_\perp$ is stepwise (the spin-flop transition is a first-order transition) for the field $H = H_{\rm sf}$ introduced in Eq. (4) when S^z changes by

$$\Delta S^z_{\rm cl} = 2S\sqrt{\frac{\kappa+\beta}{2-\kappa-\beta}}. \qquad (6)$$

The spin can be reoriented in another way when $H_1 < H_2$ and the $\Phi_\parallel \longleftrightarrow \Phi_\perp$ transition occurs via two second-order transitions through the angular phase $\Phi_\angle$ [10, 11]. For this behavior, model (3) must include competing anisotropies—single-ion anisotropy with $\beta < 0$, which corresponds to easy-axis anisotropy for $\kappa = 0$, and sufficiently large exchange anisotropy with $\kappa > -\beta$—in order for the effective magnetic anisotropy to be easy-axis anisotropy. In this case, for fields in the range $H_1 < H < H_2$, S^z varies linearly from 0 to $\Delta S^z\big|_{H=H_2} \approx \Delta S^z_{\rm cl}$, but the slope of the straight line is much larger than that in the region of the spin-flop phase (see Fig. 1).

Quantum properties. These results can be compared with the properties of magnetization in quantum model (1) for high spin by hypothesizing that, as in the exactly solvable isotropic case, all continuous classical linear dependences $S^z(H)$ (see Fig. 1) are replaced by stepwise dependences with equidistant jumps $\Delta S^z = 1$ and the jump $\Delta S^z_{\rm cl} > 1$ at the spin-flop transition point holds in the quantum case. This hypothesis is meaningful when the spin-flop transition field is stronger than the field of the first quantum jump in the isotropic case, i.e., $H_{\rm sf} > J/g\mu_{\rm B}$, and $\Delta S^z_{\rm cl} > 1$. Both conditions lead to the inequality $\kappa + \beta > 1/2S^2$, which can be satisfied for $S \gg 1$ even when anisotropy is small.

It is convenient to represent the behavior of the system in the (b, β) plane, where $b = \kappa + \beta$ is the effective anisotropy constant (see Eq. (3)). According to the classical consideration, the spin-flop transition with the spin jump $\Delta S^z_{cl} > 1$ can occur only for $\beta > 0$, and the regions with different values $\Delta S^z_{cl} = n > 1$ are vertical stripes that are bounded from the bottom by the straight line $\beta = 0$ and from the right and left by the vertical straight lines $b = b_n$ and $b = b_{n+1}$, where $b_n = 8n^2/(n^2 + 4S^2)$. The behavior with equidistant jumps $\Delta S^z = 1$, which is characteristic of the isotropic case, can be expected for small anisotropy, as well as in the region $b < 0$ of easy-plane anisotropy. For large anisotropy b in the case $\beta < 0$, $S^z = 0$ holds to the field H_1 and, then, n jumps are concentrated in the narrow field range $H_1 < H < H_2$. Thus, the classical approach predicts quite diverse behavior of the system, and this prediction is corroborated by the numerical analysis of quantum model (1) with one substantial exclusion, which will be discussed below.

Numerical simulation. Hamiltonian (1) commutes with the operator of the total spin projection $\hat{S}^z = \hat{S}^z_1 + \hat{S}^z_2$, and the total Hilbert space of the problem is decomposed into subspaces with fixed S^z values. The projection of operator (1) onto these subspaces has the form of three diagonal matrices whose eigenvalues are determined by the QR algorithm. An important simplification is possible because the Zeeman term commutes with $\hat{S}^z$, and the eigenvalues of the Hamiltonian for any field H are obtained by shifting the eigenvalues $E(S^z, 0)$ that are obtained for $H = 0$: $E(S^z, H) = E(S^z, 0) - g\mu_B HS^z$. Owing to these properties, the problem can be analyzed over the entire phase plane (κ, β) even for a high spin above $2S = 250$ in reasonable time on a computer.

Numerical analysis shows that many properties of the classical spin-flop transition hold for quantum model (1) even for a low spin $S \sim 5$. First of all, the anisotropic antiferromagnet holds both the property that the transition with $S^z = 0$ occurs in the field range $0 < H < H_1$ and the existence of jumps with $\Delta S^z > 1$ for $\beta > 0$ when the classical spin-flop transition is a first order transition. The classically predicted concentration of jumps in the narrow field range $H_1 < H < H_2$ is also observed. The shape of regions with a given value $\Delta S^z > 1$ qualitatively corresponds to the classical calculation even for a low spin. In particular, lines bounding regions with $\Delta S^z = n > 1$ for $\beta > 0$ are close to vertical lines (see Fig. 2). However, there are appreciable deviations. The first such deviation is the continuation of regions with $\Delta S^z > 1$ for small ΔS^z values to the lower half-plane.

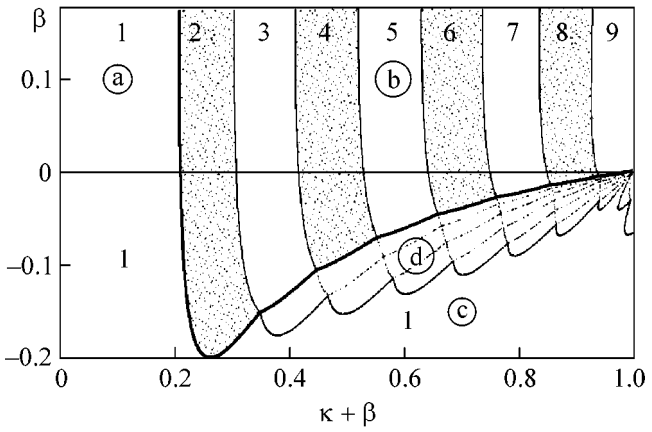

Fig. 2. Regions with different behaviors of the magnetization curve in the ($\kappa + \beta$, β) plane for $2S = 10$. The lines separate the regions with different values (indicated by digits) of the first jump ΔS^z. Regions with even ΔS^z values are shaded. A jump with $\Delta S^z = 10$ can occur even for $\kappa + \beta \geq 1$, and it corresponds to the only (Ising) point ($\kappa = 1$, $\beta = 0$) in the plane. The letters in the circles mark the characteristic regions of the phase diagram for which the $S^z(H)$ dependence is showed in Fig. 3. The thick line bounds the region where the first jump is $\Delta S^z > 1$. The curve under this region represents the region that is separated into parallelograms where the first jump is $\Delta S^z = 1$, but a value $\Delta S^z > 1$ is present among the subsequent jumps: see Fig. 3d and explanation in the text.

The behavior of the line separating regions with $\Delta S^z = 1$ and $\Delta S^z > 1$ appears to be unexpected. Its deviations from the classical result $\beta = 0$ turns out to be appreciable even for high spins $2S \simeq 200$ (see Fig. 4). The maximum size of this region in the negative β semiaxis even increases with spin and reaches the limiting value $\beta \sim -0.3$, but its area decreases with $S \longrightarrow \infty$.

In addition, for the angular phase, jumps larger than unity are observed in the magnetization curve in the parameter region d in Fig. 2 and Fig. 3d. This behavior in the high-spin limit corresponds to the first order phase transition $\Phi_\angle \longleftrightarrow \Phi_\perp$. In classical theory, this transition is of the second order and the region d is absent. Moreover, jumps $\Delta S^z = 1$ in the magnetization curve are not equidistant in the region of the concentration of jumps (below the thick line in Fig. 2) (see Fig. 3c); some of these jumps even merge together (see Fig. 3d). In the latter case, which corresponds to the narrow region d in Fig. 2, the magnetization pattern is as follows. Several first jumps occur with $\Delta S^z = 1$; then, a jump (always one) follows with $\Delta S^z > 1$, and the equidistant jumps with $\Delta S^z = 1$ finally appears. In terms of a spin-flop analogue, this behavior indicates that the $\Phi_\angle \longleftrightarrow \Phi_\perp$ transition is of the first order, which is impossible in classical model (3). Figure 5 shows a more detailed structure of the region d for $2S = 64$. The parallelogram region in the (b, β) diagram (region d in Fig. 2) corresponds to the transition from the state with

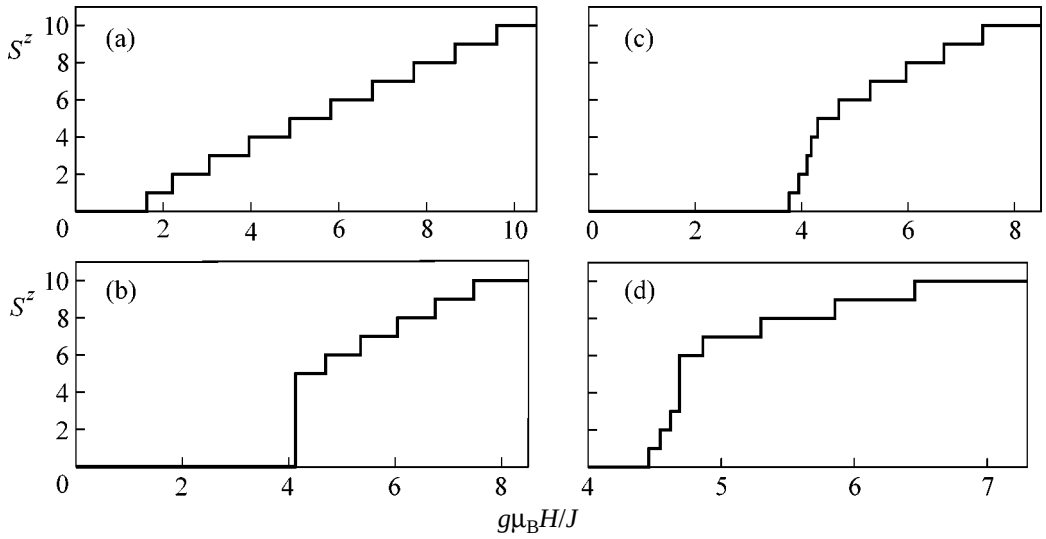

Fig. 3. Field dependence of S^z for $2S = 10$ in four characteristic regions marked in Fig. 2 by the following respective letters: (a) almost exchange behavior, $b = 0.1$ and $\beta = -0.2$; (b) merging of jumps, an analogue of the spin-flop transition, $b = 0.515$ and $\beta = 0.1$; (c) strong concentration of jumps, an analogue of the behavior in the $\Phi_\angle$ phase, $b = 0.56$ and $\beta = -0.1$; and (d) jump with $\Delta S^z > 1$ from the state with $S^z \neq 0$, an analogue of the first-order phase transition $\Phi_\angle \longleftrightarrow \Phi_\perp$, $\beta = -0.09$ and $b = 0.7$; for more details, see Fig. 5.

$S^z \neq 0$ to the state with $S^z + \Delta S^z$, where $\Delta S^z > 1$. In this case, regions with S^z and $S^z \pm 1$ adjoin each other, and regions with the same ΔS^z values join at points. This structure is responsible for the sawtooth shape of the curves with $\Delta S^z >$ const in Fig. 5. However, according to the contours in this figure and the plot in the inset, the jump value decreases rapidly when moving from the separation line between the states with $\Delta S^z = 1$ and $\Delta S^z > 1$ towards negative β values.

Results and discussion. Thus, the behavior of step quantum magnetization curves for a pair of spins with antiferromagnetic interaction and easy-axis anisotropy is complicated and depends on the ratio of two anisotropy constants of different origins in Hamiltonian (1). When single-ion anisotropy dominates, single jumps can merge with each other with the formation of a jump

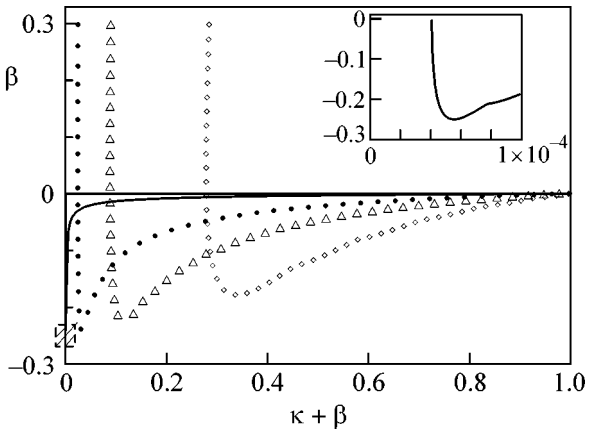

Fig. 4. Lines separating the spin-flop and angular phases for $2S = (\diamond)$ 8, $(\triangle)$ 16, and $(\bullet)$ 32. The solid line corresponds to $2S = 256$. The dashed rectangle is the region of the solid-line minimum. The inset shows this region and the section of the line near the ordinate axis for $2S = 256$.

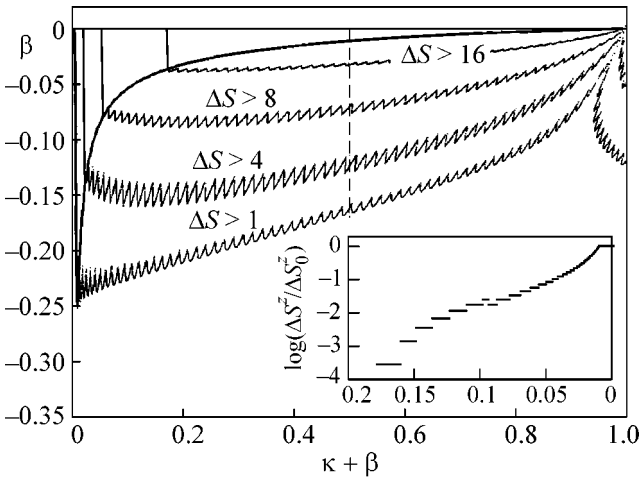

Fig. 5. Lines separating regions with a fixed jump value in the $\Phi_\angle \longleftrightarrow \Phi_\perp$ transition for $2S = 64$. Above the thick line, the jump by $\Delta S^z > 1$ occurs from the $S^z = 0$ state (cf. the corresponding lines in Figs. 2 and 4). In regions located below the thick line, the jump by ΔS^z that exceeds the value given on the right-hand side of the corresponding inequality occurs from the state with $S^z > 0$. The inset shows the section of the plot for $\kappa + \beta = 0.5$ (by the dashed vertical straight line). The ordinate axis shows the logarithm of the jump value normalized to $\Delta S_0^z \equiv \Delta S^z|_{\beta = 0}$.

by $\Delta S^z > 1$. In the opposite case, where exchange anisotropy dominates, all jumps of S^z occur by unity, but they are concentrated in a narrow field range. Analogues are found in the properties of the solutions of the quantum problem and the corresponding classical problem of the spin-flop transition even for low spins $S \sim 5$. These analogues can be suitable as the initial point in analysis of experiments and effects of other interactions. Such an analysis is beyond the scope of this brief report. At the same time, there are quantitative differences in the behaviors of the quantum system and its classical analogue. These differences are particularly substantial in the field range where the transition occurs from $\Delta S^z = 1$ to $\Delta S^z = 2$, because quantum effects that are *free* of $1/S$ smallness are manifested in this range. This surprising property is likely attributed to the fact that the quantum model with low anisotropy has a singlet ground state that differs strongly from the classical Néel state. Thus, the region of the pure quantum behavior for $S \longrightarrow \infty$ is found for the system. Similar effects are possible in the physics of antiferromagnetism. It is sufficient to mention the Haldane hypothesis that the ground states for integer and half-integer spins are different even in the $S \longrightarrow \infty$ limit [12]. Thus, the simple model considered above for two spins again shows that antiferromagnets can exhibit substantially quantum properties even for high spins.

REFERENCES

1. W. Wernsdorfer, Adv. Chem. Phys. **118**, 99 (2001).
2. R. Skomski, J. Phys.: Condens. Matter **15**, R841 (2003).
3. W. Wernsdorfer, N. Aliaga-Alcalde, D. Hendrickson, and G. Christou, Nature **416**, 406 (2002).
4. M. N. Leuenberger and D. Loss, Nature **416**, 789 (2001).
5. Y. Shapira and V. Bindilatti, J. Appl. Phys. **92**, 4155 (2002).
6. W. Wernsdorfer *et al.*, Phys. Rev. B **65**, 180403(R) (2002).
7. R. S. Edwards *et al.*, Polyhedron **22**, 1911 (2003).
8. O. Waldmann, Phys. Rev. B **61**, 6138 (2000).
9. A. S. Borovik-Romanov, in *Antiferromagnetism. Advances in Science* (Akad. Nauk SSSR, Moscow, 1962), p. 70 [in Russian].
10. K. P. Belov, A. K. Zvezdin, A. M. Kadomtseva, and R. Z. Levitin, *Orientational Transitions in Rare-Earth Magnets* (Nauka, Moscow, 1980) [in Russian].
11. V. G. Bar'yakhtar and B. A. Ivanov, Sov. Sci. Rev., Sect. A **6**, 404 (1985).
12. F. D. M. Haldane, Phys. Rev. Lett. **50**, 1153 (1983).

Translated by R. Tyapaev

JETP Letters, Vol. 81, No. 7, 2005, pp. 326–330. Translated from Pis'ma v Zhurnal Éksperimental'noĭ i Teoreticheskoĭ Fiziki, Vol. 81, No. 7, 2005, pp. 410–414.

Formation of the Incommensurate Ordered Phase in TaC_y Carbide

V. N. Lipatnikov and A. A. Rempel

Institute of Solid-State Chemistry, Ural Division, Russian Academy of Sciences, ul. Pervomaĭskaya 91, Yekaterinburg, 620219 Russia

e-mail: lipatnikov@ihim.uran.ru

Received February 14, 2005; in final form, March 1, 2005

Structural neutron diffraction studies indicate that only one ordered phase arises after the disorder–order transition in nonstoichiometric cubic tantalum carbide TaC_y. This phase arises in the composition range $y = 0.79$–0.89 due to long-term annealing with a decrease in temperature from 1600 to 300 K. It is incommensurate in the $[1–11]_{B1}$ direction, but it is close to commensurate M_6C_5 structures ($C2/m$ and $P3_1$ space groups) in mutual arrangement of atoms and vacancies in nonmetallic $(1–11)_{B1}$ planes. The disorder–order transition channel that is associated with the formation of the incommensurate superstructure in TaC_y carbide includes two arms $\mathbf{k}_5^{(6)} \approx 0.473\mathbf{b}_2$ and $\mathbf{k}_5^{(5)} = -\mathbf{k}_5^{(6)}$ of the $\{\mathbf{k}_5\}$ star and arms of the $\{\mathbf{k}_4\}$ and $\{\mathbf{k}_3\}$ stars. The translation period of the incommensurate phase in the $[1–11]_{B1}$ direction is 8.9–9.1 nm, which is larger than that in the commensurate phase M_6C_5 by a factor of about 18. © *2005 Pleiades Publishing, Inc.*

PACS numbers: 61.12.Gz, 61.50.Ks, 61.66.Fn, 61.72.Ji, 64.70.Rh

Atom–vacancy ordering often occurs in M–X systems (M = Ti, Zr, Hf, V, or Nb; X = C, N, or O) in which cubic compounds MX_y are formed with high nonstoichiometry of the nonmetallic sublattice ($MX_{y\square 1-y}$, where $0.5 \le y \le 1$ and □ is the structural vacancy) [1]. Experimental and theoretical results that were systematized in [1, 2] show that the ordering of nonstoichiometric cubic carbides MC_y is accompanied by the formation of commensurate superstructures of the M_2C, M_3C_2, M_6C_5, and M_8C_7 types with various symmetries. Incommensurate superstructures have not yet been observed in carbide-forming M–C systems containing transition *d* metals of Groups IV and V (M = Ti, Zr, Hf, V, or Nb).

Tantalum carbide TaC_y ($TaC_{y\square 1-y}$), which is a strongly nonstoichiometric compound [1, 2], is a poorly studied carbide. It has the *B*1 cubic structure and a wide homogeneity range from $TaC_{0.71}$ to $TaC_{1.00}$. A high concentration of structural vacancies □ in the nonmetallic sublattice of TaC_y provides the possibility of ordering this compound. Available information on the effect of low-temperature annealing on the basic-lattice constant, magnetic susceptibility, and specific heat of TaC_y [3–5] is indirect evidence of its ordering. Electron diffraction study [6] of $TaC_{0.83}$ carbide revealed a diffuse band whose geometry corresponds to M_6C_5 ordering with a low order degree. The thermodynamic calculation [7] of disorder–order transitions in TaC_y that was performed by the order-parameter functional method showed that the M_6C_5 superstructure is the only possible ordered phase in this carbide. The symmetry and commensurability or incommensurability of the possible superstructure were not discussed in [7].

In this work, the structure of ordered tantalum carbide is studied by the neutron and x-ray diffraction methods. TaC_y samples with various carbon contents ($0.70 \le y \le 1.00$) over the entire range of the homogeneity of the basic cubic phase were synthesized by solid-phase vacuum sintering of Ta and C powders at a temperature of 2000 K. After synthesis, samples were subjected to thermal treatment in three different regimes. Regime (a)—quenching from 1900–2000 K with a cooling rate of about 200 K/min—was used to obtain samples in a disordered state. Regimes (b) and (c)—annealing with a decrease in temperature from 1600 to 750 K over 60 and 120 h, respectively—were used to obtain samples in an equilibrium ordered state with different order degrees. Preliminary structural certification of the samples was carried out by the x-ray method with $CuK\alpha_{1,2}$ radiation. The structure of the ordered phase was analyzed by the neutron diffraction method ($\lambda = 0.1694$ nm) in the step scanning mode with $\Delta(2\theta) = 0.1°$ for 2θ angles from 12° to 90°. To reveal weak superstructure reflections, large accumulation was performed at each scanning step. The presence of background with an intensity of about 5000 pulses gave rise to parasitic reflections from radiation with wavelengths $\lambda/2$ and $\lambda/3$. These reflections correspond to the structural reflections $(200)_{B1}$, $(220)_{B1}$, and $(222)_{B1}$, and

their intensity is about 0.5% of the intensity of the main reflections.

Figure 1 shows typical spectra of the samples of nonstoichiometric carbide TaC_y for 2θ angles from 10° to the $(200)_{B1}$ structure reflection. It is the range where reflections are observed in addition to the $(111)_{B1}$ structure reflection. The intensity of the $(111)_{B1}$ reflection is low and is on the order of the intensity of superstructure reflections, because it is proportional to $(f_{Ta} - f_C)^2$ and the amplitudes $f_{Ta} = 0.70 \times 10^{-12}$ cm and $f_C = 0.665 \times 10^{-12}$ cm of the atomic scattering of tantalum and carbon, respectively, are close to each other. The superstructure reflections whose intensity depends on the thermal treatment regime are observed in the spectra of annealed tantalum carbide in the composition range $TaC_{0.79}$–$TaC_{0.89}$. Weak superstructure reflections are also observed for quenched carbide $TaC_{0.83}$ (*a*) (Fig. 1). A quenching rate of 200 K/min is likely lower than the ordering rate and, thereby, it appears to be insufficient for conserving the disordered state of tantalum carbide. X-ray diffraction analysis indicates that the constant of the basic cubic lattice of the TaC_y samples ($0.79 \le y \le 0.89$) increases slightly after annealing. A similar increase in the basic lattice constant was previously observed for carbides NbC_y [3], ThC_y [8], TiC_y [9–11], and VC_y [12].

The superstructure reflections are appreciably wider than the $(111)_{B1}$ structure reflection, their intensity decreases rapidly when the diffraction angle 2θ increases, and they are hardly observed for 2θ > 50°. This behavior indicates that the domains of the ordered phase of tantalum carbide are much smaller than the grains of disordered carbide with the basic structure *B*1. The features discussed above imply that a structure with perfect long-range order is not formed in TaC_y carbide even after long-term annealing, although ordering occurs quite rapidly.

The wave vectors that bound the first Brillouin zone correspond to the angular range 2θ = 19°–25° in the neutron diffraction pattern of tantalum carbide. The presence of the superstructure reflections in this range indicates that static concentration waves whose wave vectors lie near the boundaries of the first Brillouin zone appear in the crystal. According to [1, 2], the ordering of nonstoichiometric monocarbides of transition metals of Group V is accompanied by the formation of M_6C_5 superstructures with the $C2/m$, $P3_1$, and $C2$ space groups. The formation of these superstructures is attributed to the distortion of the symmetry of the basic lattice over the wave vector stars $\{\mathbf{k}_9\}$, $\{\mathbf{k}_4\}$, and $\{\mathbf{k}_3\}$. The channel of the disorder–order transition that is associated with the formation of the monoclinic ($C2$ space group) superstructure M_6C_5 includes also the arms of the $\{\mathbf{k}_0\}$ star (hereafter, the stars and their arms are enumerated according to [1, 13]). The positions of the superstructure reflections for these stars are calculated for the basis cubic lattice whose period a_{B1} = 0.4428 nm corresponds to $TaC_{0.83}$ carbide. The comparison of the positions of the calculated and observed superstructure reflections indicates that neutron diffraction patterns include reflections associated with the $\{\mathbf{k}_4\}$ and $\{\mathbf{k}_3\}$ stars, but they do not include reflections associated with the $\{\mathbf{k}_0\}$ star. Analysis of neutron diffraction patterns also shows that reflections at angles 2θ = 19.0°, 37.0°, 49.3°, 59.6°, etc., i.e., reflections that correspond to the $\{\mathbf{k}_9\}$ star of the nonmetallic fcc sublattice, are absent in the spectra of ordered carbide TaC_y. These reflections in the TaC_y diffraction spectra are split into two superstructure reflections (satellites), e.g., 2θ ~ 18.0° and 20.5° (see Fig. 1).

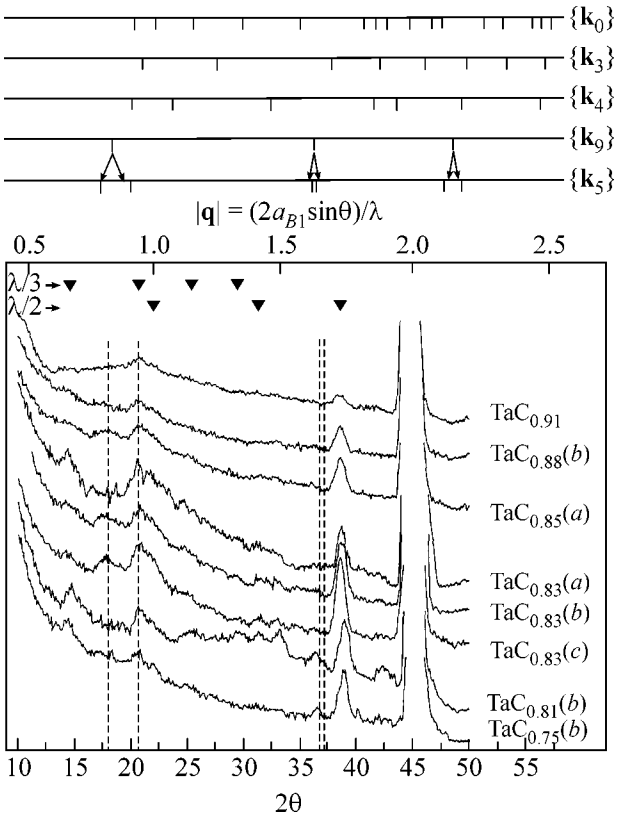

Fig. 1. Neutron diffraction patterns of tantalum carbide TaC_y in various structural states after thermal treatment in the (*a*), (*b*), and (*c*) regimes described in the text. The upper panel shows the position of reflections associated with the $\{\mathbf{k}_0\}$, $\{\mathbf{k}_3\}$, $\{\mathbf{k}_4\}$, $\{\mathbf{k}_9\}$, and $\{\mathbf{k}_5\}$ stars, as well as the splitting of reflections that correspond to the $\{\mathbf{k}_9\}$ star and are observed in commensurate superstructures of the M_6C_5 type into experimental superstructure reflections associated with the $\{\mathbf{k}_5\}$ star (the positions of the latter reflections are shown by the dashed lines). The neutron wavelength is λ = 0.1694 nm, the reflection positions are calculated for TaC_y tantalum carbide with a basic-cubic-lattice period of a_{B1} = 0.4428 nm, and symbols ▼ indicate the positions of the reflections attributed to radiation with wavelengths λ/2 and λ/3.

Complete and partially defective planes alternate in the nonmetallic sublattice of superstructures of the

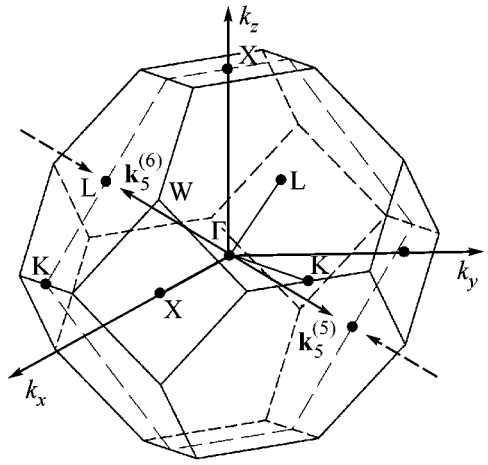

Fig. 2. Positions of the superstructure vectors $\mathbf{k}_5^{(6)}$ and $-\mathbf{k}_5^{(6)} \equiv \mathbf{k}_5^{(5)}$ in the (110) section of the first Brillouin zone of the fcc lattice [the (110) section is shown by dashed lines]. The superstructure vectors shown by dashes are formed by the reciprocal-lattice sites nearest to the Γ = (0 0 0) site. The presence of two incommensurate superstructure vectors $\mathbf{k}_5^{(j)}$ with $\mu_5 \approx 0.473$ near the point L = (1/2 –1/2 1/2), which corresponds to the commensurate vector $\mathbf{k}_5^{(3)}$, leads to the appearance of two close superstructure reflections at $2\theta \approx 18.0°$ and 20.5° in the diffraction spectra of the polycrystalline samples.

M_6C_5 type (the $C2/m$, $P3_1$, and $C2$ space groups) in the $[1\bar{1}1]_{B1}$ direction (or in the equivalent directions $[111]_{B1}$, $[\bar{1}11]_{B1}$, and $[11\bar{1}]_{B1}$, depending on the orientation of the unit cell). All sites of the complete planes are occupied by carbon atoms, whereas some sites in the defective planes are vacant. The alternation of complete and defective nonmetallic atomic planes $(1\bar{1}1)_{B1}$ in ordered M_6C_5 structures is caused by the presence of the arm $\mathbf{k}_9^{(3)}$ of the $\{\mathbf{k}_9\}$ star in the channels of the corresponding disorder–order transitions [14]. The $\{\mathbf{k}_9\}$ star ensures the commensurability of all three structures, because the corresponding interplanar spacing coincides with one of the interplanar distances of the basic cubic structure $B1$.

Satellites into which reflections corresponding to the $\{\mathbf{k}_9\}$ star are split can be referred to the $\{\mathbf{k}_5\}$ star. The arms of the $\{\mathbf{k}_5\}$ star are collinear to the arms of the $\{\mathbf{k}_9\}$ star, but they do not reach the boundary of the first Brillouin zone. Their length is determined by the parameter $0 < \mu_5 < 1/2$ (Fig. 2). The positions of the $\mathbf{k}_5^{(j)}$ arms can generally vary from zero of the reciprocal space (Brillouin zone center) to the points L = (1/2 1/2 1/2) at the boundary of the first Brillouin zone, which correspond to the arms of the $\{\mathbf{k}_9\}$ star. The presence of the arms of the $\{\mathbf{k}_5\}$ star in the transition channel actually means that the superstructure of tantalum carbide is incommensurate.

The parameter μ_5 can be determined from experimental neutron diffraction spectra (see Fig. 1). The $\mathbf{k}_9^{(3)} = \mathbf{b}_2$ arm is collinear to the $\mathbf{k}_5^{(6)} = \mu_5\mathbf{b}_2 = \{\mu_5, -\mu_5, \mu_5\}$ arm, where $\mathbf{b}_2 = \{1\text{–}11\}$. Moreover, there is the opposite superstructure vector $-\mathbf{k}_5^{(6)} = \mathbf{k}_5^{(5)}$. The $\mathbf{k}_5^{(5)}$ vector is not equivalent to the $\mathbf{k}_5^{(6)}$ vector, and it enters into the phase transition channel along with the $\mathbf{k}_5^{(6)}$ vector. The superstructure diffraction vectors $\mathbf{q}_{i,5}$ that are associated with the $\{\mathbf{k}_5\}$ star and that are generated by the structure sites $\mathbf{H}_i$ are equal to $(\mathbf{H}_i + \mathbf{k}_5^{(j)})$, where $\mathbf{k}_5^{(j)}$ are the arms of the $\{\mathbf{k}_5\}$ star that enter into the transition channel. Therefore, $\mathbf{q}_{i,5} = (\mathbf{H}_i \pm \mathbf{k}_5^{(6)})$. The first superstructure vector that is generated by the (0 0 0) site coincides with the $\mathbf{k}_5^{(6)}$ wave vector, and its modulus is $|\mathbf{q}_{1,5}| = |\mathbf{k}_5^{(6)}| = \mu_5\sqrt{3}$. The length of the diffraction vector can be expressed as $\mathbf{q}_{i,5} = (2a_{B1}\sin\theta_{i,5})/\lambda$. Therefore,

$$\mu_5 = (2a_{B1}\sin\theta_{1,5})/\sqrt{3}\lambda. \qquad (1)$$

The superstructure vector with a length of $|\mathbf{k}_5^{(6)}|$ for ordered $TaC_{0.83}$ carbide (c) is observed at diffraction angle $2\theta_{1,5} \cong 18.0°\text{–}18.06°$. Calculation for this angle yields $\mu_5 \approx 0.472\text{–}0.474$. For all superstructure vectors that are associated with the $\{\mathbf{k}_5\}$ star, the average parameter μ_5 is equal to 0.473. Similar calculations show that, within the diffraction experiment accuracy, the parameter μ_5 is the same for ordered carbides TaC_y with another carbon content; i.e., in the first approximation, $\mu_5 \approx 0.473$ for any carbon content in TaC_y. Thus, the disorder–order transition channel that is associated with the formation of the incommensurate ordered phase in TaC_y includes the arms $\mathbf{k}_5^{(6)} \approx 0.473\mathbf{b}_2$ and $\mathbf{k}_5^{(5)} = -\mathbf{k}_5^{(6)}$ of the $\{\mathbf{k}_5\}$ star (see Fig. 2) and the arms of the $\{\mathbf{k}_4\}$ and $\{\mathbf{k}_3\}$ stars.

According to the symmetry analysis, the superstructure of tantalum carbide differs from the known M_6C_5 superstructures (the $C2/m$ and $P3_1$ space groups) that are formed via the disorder–order transition channels containing the arms of the $\{\mathbf{k}_9\}$, $\{\mathbf{k}_4\}$, and $\{\mathbf{k}_3\}$ stars. The vectors of the $\{\mathbf{k}_9\}$ star ensure both the commensurability of these superstructures and the sequential alternation of complete and defective nonmetallic atomic planes $(1\bar{1}1)_{B1}$, and the vectors of the $\{\mathbf{k}_4\}$ and $\{\mathbf{k}_3\}$ stars determine the mutual arrangement of vacant

sites and sites occupied by carbon atoms. The disorder–order transition channel that is associated with the formation of the superstructure in TaC_y contains the arms of the $\{\mathbf{k}_5\}$ star with $\mu_5 \approx 0.473$ instead of the arms of the $\{\mathbf{k}_9\}$ star. For this μ_5 value, any interplanar distance of the superstructure of TaC_y carbide does not coincide with the interplanar distances of the basic cubic structure $B1$. Therefore, the ordered phase found for nonstoichiometric TaC_y carbide is incommensurate in the $[1\bar{1}1]_{B1}$ direction or in the equivalent directions $[111]_{B1}$, $[\bar{1}11]_{B1}$, and $[11\bar{1}]_{B1}$, but it is close to commensurate M_6C_5 structures ($C2/m$ and $P3_1$ space groups) in the mutual arrangement of atoms and vacancies in the nonmetallic $(1\bar{1}1)_{B1}$ planes.

Let us consider functions that describe the probability of the presence of a carbon atom in a site of a nonmetallic $(1\bar{1}1)_{B1}$ plane, i.e., the carbon filling factor $P^{(1-11)}$ of the nonmetallic $(1\bar{1}1)_{B1}$ planes in MC_y carbide with any long-range order degree η. Taking into account the distribution functions for commensurate M_6C_5 superstructures [1, 14], we express the filling factor $P_{\text{com}}^{(1-11)}$ as

$$P_{\text{com}}^{(1-11)} = y - (\eta_9/6)\cos(2\pi\mu_9 z). \quad (2)$$

Here, z is the ordinal number of a nonmetallic $(1\bar{1}1)_{B1}$ plane, i.e., it is an integer; η_9 is the long-range order parameter corresponding to the $\{\mathbf{k}_9\}$ star; and $\mu_9 = 1/2$. According to Eq. (2), nonmetallic atomic $(1\bar{1}1)_{B1}$ planes with maximum $P_{\text{max}}^{(1-11)}$ and minimum $P_{\text{min}}^{(1-11)}$ filling factors alternate in the $[1\bar{1}1]_{B1}$ direction in commensurate M_6C_5 superstructures. For an incommensurate order structure close to M_6C_5, the expression for the C-atom filling factor of nonmetallic $(1\bar{1}1)_{B1}$ planes in MC_y carbide is similar:

$$P_{\text{inc}}^{(1-11)} = y - (\eta_5/6)\cos(2\pi\mu_5 z). \quad (3)$$

Note that functions (2) and (3) have a physical meaning only in $(1\bar{1}1)_{B1}$ planes. It follows from these formulas that the maximum and minimum filling factors of nonmetallic$(1\bar{1}1)_{B1}$ planes for carbon atoms are equal to $P_{\text{max}}^{(1-11)} = y + \eta/6$ and $P_{\text{min}}^{(1-11)} = y - \eta/6$, respectively, where $\eta = \eta_9$ and η_5 for the commensurate and incommensurate superstructures, respectively.

The maxima and minima of the function $P^{(1-11)}$ for the incommensurate superstructure do not coincide with nonmetallic $(1\bar{1}1)_{B1}$ planes. Therefore, the carbon filling factor for these planes is intermediate between $P_{\text{max}}^{(1-11)}$ and $P_{\text{min}}^{(1-11)}$. In other words, the concentration wave corresponding to the $\{\mathbf{k}_5\}$ star has maxima and minima that do not coincide with nonmetallic $(1\bar{1}1)_{B1}$ planes. Every second nonmetallic $(1\bar{1}1)_{B1}$ plane in the commensurate M_6C_5 superstructure has the maximum filling factor for C atoms, whereas only every 18th nonmetallic $(1\bar{1}1)_{B1}$ plane (18th, 37th, 54th, 73rd, etc.) is maximally filled with C atoms in incommensurate tantalum carbide. Thus, the translation period in the $[1\bar{1}1]_{B1}$ direction in incommensurate ordered tantalum carbide is equal to 8.9–9.1 nm, which is larger than the value $(2\sqrt{3})a_{B1}/3 = 0.5112$ nm for the commensurate M_6C_5 phase by a factor of about 18. The translation period depends on the tantalum carbide composition and thermal-treatment conditions.

Noncoincidence of the maxima and minima of the concentration waves with the $(1\bar{1}1)_{B1}$ planes of the nonmetallic sublattice means that the probabilities of filling carbon and vacant sites in incommensurate ordered carbide Ta_6C_5 ($TaC_{0.83}$) appreciably differ from 1 and 0, respectively. As a result, the degrees of the long- and short-range orders in ordered tantalum carbide are far from the maximum possible values.

For the same long-range order parameters $\eta_9 = \eta_5 = \eta$, the difference between the filling factors of nonmetallic $(1\bar{1}1)_{B1}$ planes in the incommensurate and commensurate superstructures is expressed as

$$P_{\text{inc}}^{(1-11)} - P_{\text{com}}^{(1-11)} = -(\eta/3)\sin[\pi z(\mu_9 + \mu_5)]\sin[\pi z(\mu_9 - \mu_5)]. \quad (4)$$

Let us estimate at which $(1\bar{1}1)_{B1}$ plane of the nonmetallic sublattice the probability $P_{\text{inc}}^{(1-11)}$ is equal to the probability $P_{\text{com}}^{(1-11)}$; i.e., $P_{\text{inc}}^{(1-11)} - P_{\text{com}}^{(1-11)} = 0$. In this case, substituting μ_9 and μ_5 values into Eq. (4), we obtain $z \approx 37m$, where $m = 0, 1, 2, \ldots$. Thus, the filling factors of nonmetallic $(1\bar{1}1)_{B1}$ planes for carbon atoms in the incommensurate and commensurate M_6C_5 superstructures coincide with each other in every 37th plane.

Another explanation of the distribution of carbon atoms and vacancies in ordered tantalum carbide seems to be possible. The ordered structure of nonstoichiometric carbide TaC_y can be represented as sequences $[(CD)_nC]_\infty$ or $[(CD)_nD]_\infty$ of alternating complete C and ordered defective D nonmetallic planes, i.e., as a long-range periodic structure. However, the parameter μ_5 for the long-range periodic structure $[(CD)_nC]_\infty$ or $[(CD)_nD]_\infty$ must depend on the content of TaC_y carbide, while such a dependence is not revealed within the accuracy of the diffraction experiment in this work.

This incommensurability of the structure also means the absence of the exact stoichiometric composition of the ordered phase. In particular, this property

explains a weak dependence of the intensity of superstructure reflections on the composition of TaC_y tantalum carbide (see Fig. 1).

The observation of only one ordered phase over the entire homogeneity range of TaC_y carbide is consistent with the calculation [7] of the phase diagram of the Ta–C system. According to that calculation, only one superstructure is possible in TaC_y carbide, and the homogeneity range of this superstructure at T = 300–800 K is $TaC_{0.81–0.83}$–$TaC_{0.89–0.92}$. The formation of an incommensurate superstructure is experimentally observed for the composition range from $TaC_{0.79}$ to $TaC_{0.89}$, which corresponds to the estimate obtained in [7] for the position and width of the homogeneity range of the ordered phase of tantalum carbide.

Thus, the above investigation indicates that only one ordered phase is formed over the entire homogeneity range $TaC_{0.71}$–$TaC_{1.00}$ of disordered tantalum carbide. This phase is incommensurate in the $[1–11]_{B1}$ direction, but it is close to M_6C_5 superstructures in the mutual arrangement of C atoms and □ vacancies. Only commensurate superstructures have been previously detected in other nonstoichiometric carbides and nitrides.

We are grateful to A.I. Gusev for stimulating discussion. This work was supported by the Russian Foundation for Basic Research (project no. 03-03-32031a).

REFERENCES

1. A. I. Gusev, A. A. Rempel, and A. J. Magerl, *Disorder and Order in Strongly Nonstoichiometric Compounds: Transition Metal Carbides, Nitrides, and Oxides* (Springer, Berlin, 2001).
2. A. I. Gusev and A. A. Rempel, *Nonstoichiometry, Disorder, and Order in Solids* (Ural. Otd. Ross. Akad. Nauk, Yekaterinburg, 2001) [in Russian].
3. V. N. Lipatnikov, A. A. Rempel, and A. I. Gusev, Izv. Akad. Nauk SSSR, Neorg. Mater. **26**, 2522 (1990).
4. A. I. Gusev, A. A. Rempel, and V. N. Lipatnikov, Phys. Status Solidi A **106**, 459 (1988).
5. V. N. Lipatnikov, A. A. Rempel, and A. I. Gusev, Fiz. Tverd. Tela (Leningrad) **31** (10), 285 (1989) [Sov. Phys. Solid State **31**, 1818 (1989)].
6. J. D. Venables and M. H. Meyerhoff, NBS Spec. Publ. **364**, 583 (1972).
7. A. I. Gusev, Usp. Fiz. Nauk **170**, 3 (2000) [Phys. Usp. **43**, 1 (2000)].
8. R. Lorenzelli and I. de Dieuleveult, J. Nucl. Mater. **29**, 349 (1969).
9. V. Moisy-Maurice, N. Lorenzelli, C. H. de Novion, and P. Convert, Acta Metall. **30**, 1769 (1982).
10. S. Tsurekawa and H. Yoshihaga, J. Jpn. Inst. Met. **56**, 133 (1992).
11. A. N. Emel'yanov, Teplofiz. Vys. Temp. **28**, 269 (1990).
12. T. Athanassiadis, N. Lorenzelli, and C. H. de Novion, Ann. Chum. France **12**, 129 (1987).
13. O. V. Kovalev, *Irreducible Representations of the Space Groups* (Akad. Nauk Ukr. SSR, Kiev, 1961; Gordon and Breach, New York, 1965).
14. A. I. Gusev and A. A. Rempel, J. Phys. C: Solid State Phys. **20**, 5011 (1987).

Translated by R. Tyapaev

JETP Letters, Vol. 81, No. 7, 2005, pp. 331–334. Translated from Pis'ma v Zhurnal Éksperimental'noĭ i Teoreticheskoĭ Fiziki, Vol. 81, No. 7, 2005, pp. 415–418.

Phonon Localization in Ge Nanoislands and Its Manifestation in Raman Spectra

D. A. Orekhov, V. A. Volodin, M. D. Efremov, A. I. Nikiforov, V. V. Ul'yanov, and O. P. Pchelyakov

Institute of Semiconductor Physics, Siberian Division, Russian Academy of Sciences, pr. Akademika Lavrent'eva 13, Novosibirsk, 630090 Russia

e-mail: volodin@isp.nsc.ru

Received February 21, 2005

Multilayer structures with germanium nanoislands that are formed on the silicon (111) surface upon submonolayer deposition by molecular-beam epitaxy have been investigated using Raman spectroscopy. To interpret the experimental Raman spectra, numerical calculations of the spectra have been performed for nanoislands containing from several to several hundred germanium atoms. The calculations demonstrate that the in-plane sizes of nanoislands (with sizes less than 2–3 nm) substantially affect the frequencies of phonons localized in these nanoislands. The experimental Raman spectra confirm the occurrence of the quantum size effect. © *2005 Pleiades Publishing, Inc.*

PACS numbers: 63.22.+m, 78.30.–j, 81.15.Hi

By now, the Stranski–Krastanov mechanism is well-understood and widely used for the formation of germanium quantum dots (QDs) in silicon (see [1] and references therein). Approaches to the formation of germanium QDs without forming a wetting layer have also been developed recently, such as the growth of germanium on ultrathin silicon oxide [2, 3] or the formation of Ge clusters at submonolayer coverage [4, 5]. From direct measurements by scanning tunneling microscopy, it is known that, in the initial stage of deposition, germanium forms triangular nanoislands from one to three bilayers thick (depending on the deposition rate) on the reconstructed Si(111)-(7×7) surface [6]. Similar to the electron spectrum, the phonon spectrum of a QD must represent a set of discrete modes determined by size quantization. Therefore, rapid and nondestructive Raman scattering spectroscopy is an informative technique for studying the properties of semiconductor nanoobjects [7–9].

An experimental sample was manufactured on a Si(111) substrate using molecular beam epitaxy. A silicon buffer layer 50 nm thick was grown on a conventionally cleaned substrate at a temperature of 700°C. According to high-energy electron diffraction data, the silicon surface was (7×7) reconstructed. Next, Ge was grown at a temperature of 400°C to an effective thickness of 0.3 bilayer (BL). One Ge bilayer contains 1.44×10^{15} atom/cm^2. The Ge islands formed were covered from above by a Si layer 4 nm thick at the same growth temperature of 400°C. In this way, 20 periods of such a structure were grown. The deposition rate was 1.5 BL/min for both germanium and silicon. The samples obtained were studied using Raman spectroscopy. The spectra were measured at room temperature on an automated setup based on a DFS-52 spectrometer (LOMO, St. Petersburg) using the 514.5-nm Ar laser line (2.41 eV). A quasi-backscattering geometry was used, the incident light was polarized along the $\langle 01\bar{1}\rangle$ crystallographic direction, and the scattered light polarization was not analyzed.

The Raman spectra of the sample with germanium nanoislands and the Si(111) substrate are shown in Fig. 1 in the region of vibrational frequencies of both Ge–Ge and Si–Ge bonds. Features near 305 cm^{-1} that are associated with two-phonon scattering from transverse acoustic (TA) phonons in silicon [10] are seen in both spectra. The spectra of the sample with germanium nanoislands exhibit a Raman peak with a maximum at ~280–290 cm^{-1}, which is absent in the substrate spectrum. The inset in the figure shows the Raman spectrum of germanium nanoislands (minus the substrate signal). The spectrum also exhibits peaks from scattering by Ge–Si bond vibrations (~420 cm^{-1}).

Numerical simulation was carried out to analyze the experimental Raman spectra. The natural frequencies and eigenvectors of vibrations in Ge/Si heterostructures were calculated in the Born model using the approximation of cyclic boundary conditions. Next, the Raman spectra were calculated from the obtained data using the Wolkenstein bond polarizability model [7, 9, 11]. The force constants of germanium bonds in the Born model were determined by fitting the calculated phonon dispersion in the bulk material to the experimental data of slow neutron scattering [12]. Since the phonon dispersions for germanium and silicon are very

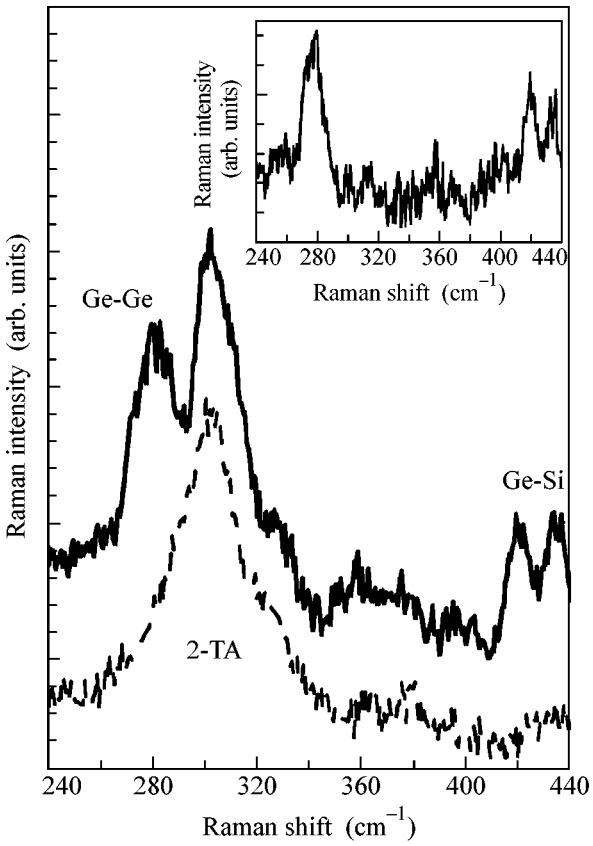

Fig. 1. Raman spectra of the (solid line) sample with germanium nanoislands and (dashed line) silicon (111) substrate. The inset shows the contribution from nanoislands (the signal from the substrate is subtracted).

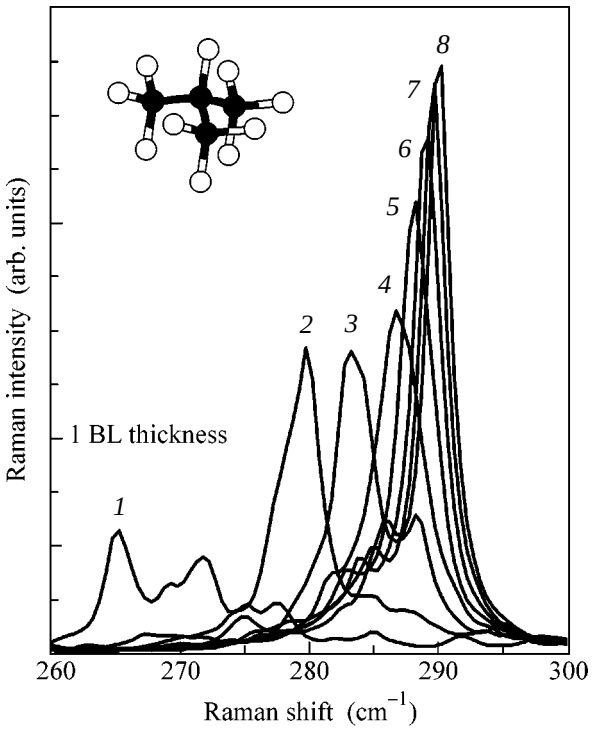

Fig. 2. Calculated Raman spectra of germanium nanoislands one bilayer in height. The numbers at the curves indicate the in-plane size of nanoislands in terms of the number of unit cells (see explanations in text). The inset shows the configuration of an island corresponding to spectrum *1*. Germanium atoms are shown in black color.

similar, the mass substitution method was used to construct Ge/Si heterostructures. The ratio of the derivatives of bond polarizabilities for germanium and silicon was determined from the ratios of Raman intensities for germanium and silicon normalized to the scattering volume. Computational details are described more comprehensively in [3, 13].

The calculated spectra are given in Figs. 2 and 3. The calculations were performed for islands of a triangular shape specified by the symmetry of the reconstructed (111)-(7 × 7) surface. The crystal structure of the smallest islands for a thickness of 1 and 2 BL is given in the insets of the figures. Germanium atoms are shown in black. In our work, a four-atomic germanium cluster shown schematically in black in the inset of Fig. 2 was taken as a unit cell.

The Raman peak of bulk germanium that is associated with scattering by optical phonons is located at 302 cm^{-1}. It is known that the effects of localization in a planar layer reduce the optical phonon frequencies. The effects of lateral localization on the frequencies of optical vibrations are clearly seen in Figs. 2 and 3. The frequencies of localized optical phonons decrease with the lateral sizes of nanoislands. A comparative analysis of the experimental and calculated spectra can give information on the lateral sizes of germanium nanoislands.

It is known that mechanical compressions can lead to an increase in the frequency of Ge–Ge bond vibrations. At a mismatch in the lattice constants of approximately 4%, the shift for transverse optical (TO) modes can reach 10 cm^{-1}. The effect of mechanical stresses was disregarded in the calculated Raman spectra, and the inclusion of mechanical stresses would lead to a shift of peaks (by 10 cm^{-1}) toward the high-frequency region. If the germanium nanoislands 1 and 2 BL thick had in-plane sizes of 7–8 unit cells (about 3 nm, approximately), peaks at 300–305 cm^{-1} would be observed experimentally. Unfortunately, this frequency range in the experimental spectra corresponds to a two-phonon peak from the substrate and, therefore, cannot be clearly resolved. However, when the substrate signal is subtracted from the spectrum (inset in Fig. 1), the signal is virtually absent at these frequencies. Thus, the following two assumptions are possible: first, mechanical stresses in nanoislands are completely relaxed or, second, almost all nanoislands have lateral sizes of 1 to 3 unit cells. It is known that the relaxation of mechanical stresses starts at the deposition of germanium with

a thickness of approximately 4 BL or more. Therefore, the second assumption is more probable.

The results obtained from the analysis of the Raman data are in qualitative agreement with the direct data obtained using scanning tunneling microscopy (STM). The dependence of the number of germanium atoms contained in the first, second, and third bilayers on the deposition rate (in the range from 10^{-3} to 10^{-2} BL/min) is given in [14]. The extrapolation of the dependences obtained in that work to the region of deposition rates that are two orders of magnitude higher shows that germanium could form nanoislands only 1 and 2 BL in thickness. It seems that nanoislands 3 BL thick have no time to be formed at such relatively high deposition rates. The dependence of the density of germanium nanoislands on the deposition rate (in the range from 10^{-3} to 10^{-2} BL/min at a deposition temperature of 400°C and coverage of 0.3–0.5 BL) is also given in [14]. The extrapolation of this dependence to a deposition rate of 1.5 BL/min used in our work yields a value of 10^{13} cm^{-2} for the density of nanoislands. Approximately 4×10^{14} atoms/cm^2 are contained in 0.3-BL germanium, and simple estimates show that one nanoisland contains several tens of atoms on the average. The smallest germanium clusters that are used in our calculations (shown in Figs. 2 and 3) contain 4 and 13 germanium atoms, respectively. It seems that nanoislands containing from several to hundred germanium atoms contribute to the wide experimental peak (Fig. 1), which coincides with the estimate. Actually, according to the analysis of the direct STM data (for deposition rates lower by approximately two orders of magnitude), it may be assumed that the sizes of Ge nanoislands at conventional MBE rates do not exceed half the cell of the (7×7) surface structure [6, 14]. As an example, we present an STM image of germanium nanoislands obtained after deposition of 0.4-BL Ge at 350°C (Fig. 4). Along with fairly large triangular islands, a multitude of clusters with sizes of 2–3 nm are seen in the figure.

An analysis of the vibrational eigenvectors shows that TO-like modes are mainly active in the Raman spectra, although transverse and longitudinal modes are already rather strongly mixed in the case of small nanoislands. The longitudinal optical modes are almost not localized in small germanium clusters because of mixing with longitudinal acoustic modes in silicon, which have the same frequencies. Since we used cyclic boundary conditions, phonons were calculated for a periodic array of nanoislands rather than for a separate nanoisland. In this case, the mutual effects of neighboring nanoislands on the phonon frequencies were negligibly small even when the distances between them were equal to two to three lattice constants or more.

Thus, according to the analysis of Raman spectra, it may be concluded that, for a coverage of 0.3 BL, a temperature of 400°C, and a deposition rate of 1.5 BL/min, germanium forms nanoislands with in-plane sizes of less than 3 nm on the (7×7) reconstructed silicon (111) surface. A shift in the frequency of optical modes in Ge nanoislands was observed experimentally, and it can be

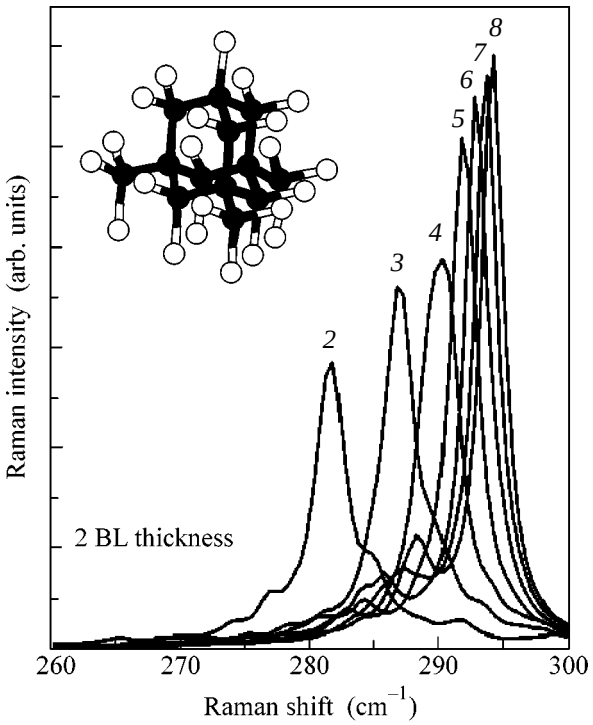

Fig. 3. Calculated Raman spectra of germanium nanoislands two bilayers in height. The numbers at the curves indicate the in-plane size of nanoislands in terms of the number of unit cells. The inset shows the configuration of an island corresponding to spectrum *2*. Germanium atoms are shown in black.

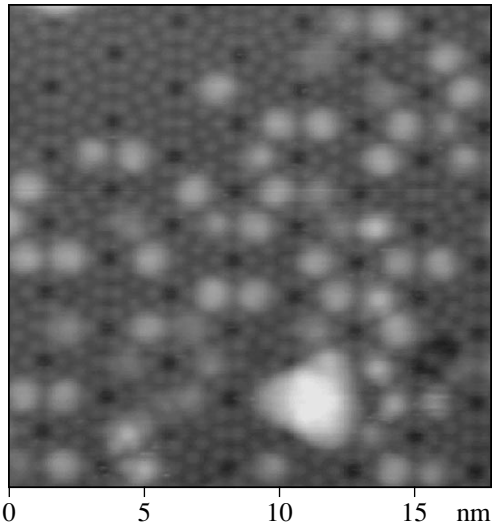

Fig. 4. STM image of the Si(111) surface with Ge clusters in half-cells of the (7×7) surface structure after the deposition of 0.4-BL Ge at a temperature of 350°C and a deposition rate of 6×10^{-3} BL/min.

explained by the effect of phonon localization in nanoislands.

We are grateful to S.A. Teys for presenting the STM image, useful consultations concerning the analysis of STM data, and stimulating discussions. This work was supported by the Russian Foundation for Basic Research, project no. 03-02-16506, and the Council of the President of the Russian Federation for Support of Young Russian Scientists and Leading Scientific Schools, project no. NSh-533.2003.2.

REFERENCES

1. O. P. Pchelyakov, Yu. B. Bolkhovityanov, A. V. Dvurechenskiĭ, *et al.*, Fiz. Tekh. Poluprovodn. (St. Petersburg) **34**, 1281 (2000) [Semiconductors **34**, 1229 (2000)].
2. A. A. Shklyaev, M. Shibata, and M. Ichikawa, Phys. Rev. B **62**, 1540 (2000).
3. V. A. Volodin, M. D. Efremov, A. I. Nikiforov, *et al.*, Fiz. Tekh. Poluprovodn. (St. Petersburg) **37**, 1220 (2003) [Semiconductors **37**, 1190 (2003)].
4. N. D. Zakharov, G. E. Cirlin, P. Werner, *et al.*, in *Proceedings of 9th International Symposium on Nanostructures: Physics and Technology* (St. Peterburg, Russia, 2001), p. 21.
5. V. A. Volodin, D. A. Orehov, M. D. Efremov, *et al.*, in *Proceedings of 10th International Symposium on Nanostructures: Physics and Technology* (St. Petersburg, Russia, 2002), p. 179.
6. S. A. Teys and B. Z. Olshanetsky, Phys. Low-Dimens. Semicond. Struct., No. 1/2, 37 (2002).
7. *Light Scattering in Solids V Superlattices and Other Microstructures*, Ed. by M. Cardona and G. Günterodt (Springer, Berlin, 1989).
8. M. D. Efremov, V. A. Volodin, V. A. Sachkov, *et al.*, Pis'ma Zh. Éksp. Teor. Fiz. **70**, 73 (1999) [JETP Lett. **70**, 75 (1999)].
9. M. D. Efremov, V. A. Volodin, V. V. Preobrazhenskii, *et al.*, *Trends in Nanotechnology Research* (Nova Sci., New York, 2004).
10. P. A. Temple and C. E. Hathaway, Phys. Rev. B **7**, 3685 (1973).
11. M. Vol'kenshteĭn, Dokl. Akad. Nauk SSSR **32**, 185 (1941).
12. G. Nelin and G. Nilsson, Phys. Rev. B **5**, 3151 (1972).
13. V. A. Sachkov, V. V. Bolotov, V. A. Volodin, and M. D. Efremov, Preprint No. 2000-01, ISMÉ SO RAN (Inst. of Sensor Microelectronics, Siberian Division, Russian Academy of Sciences, Novosibirsk, 2000).
14. S. A. Teys, K. N. Romanyuk, A. B. Talochkin, *et al.*, in *Proceedings of 12th International Conference on STM and Related Techniques* (2003), p. 775.

Translated by A. Bagatur'yants

JETP Letters, Vol. 81, No. 7, 2005, pp. 335–341. From Pis'ma v Zhurnal Éksperimental'noĭ i Teoreticheskoĭ Fiziki, Vol. 81, No. 7, 2005, pp. 419–425.

The Current Phase Relation in Josephson Tunnel Junctions¶

A. A. Golubov[1] and M. Yu. Kupriyanov[2]

[1] *Faculty of Science and Technology, University of Twente, The Netherlands*
e-mail: a.golubov@tnw.utwente.nl
[2] *Nuclear Physics Institute, Moscow State University, Moscow, 119992 Russia*
e-mail: mkupr@pn.sinp.msu.ru

Received March 4, 2005

The $J(\varphi)$ relation in SFIFS, SNINS, and SIS tunnel junctions is studied. A method for the analytical solution of linearized Usadel equations has been developed and applied to these structures. It is shown that the Josephson current across the structure has a sum of $\sin\varphi$ and $\sin 2\varphi$ components. Two different physical mechanisms are responsible for the sign of $\sin 2\varphi$. The first one is the depairing by current, which contributes positively to the $\sin 2\varphi$ term, while the second one is the finite transparency of SF or SN interfaces, which provides the negative contribution. In SFIFS junctions, where the first harmonic vanishes at the 0–π transition, the calculated second harmonic fully determines the $J(\varphi)$ curve. © *2005 Pleiades Publishing, Inc.*

PACS numbers: 74.50.+r, 74.80.Dm, 75.30.Et

It is well known that tunnel SIS Josephson junctions have a sinusoidal current–phase relation, while, with a decrease in the barrier transparency, deviations from $\sin\varphi$ take place (see [1, 2] for a review). The sign of second harmonic is important for many applications, in particular, in junctions with a more complex structure such as SNINS or SFIFS, where N is a normal metal and F is a weak metallic ferromagnet [2–4]. To analyze this problem self-consistently, one should go beyond the usual "rigid boundary conditions" (RBC) approximation.

The RBC method is an effective tool used extensively earlier for theoretical study of the proximity and Josephson effects [1, 2]. This method is based on the assumption that all nonlinear and nonequlibrium effects in a Josephson structure are located in a "weak link" connecting two superconducting electrodes. The back influence of these effects on superconductivity in the electrodes is neglected. The RBC approximation is valid if a junction has the constriction geometry. The quantitative criteria for the validity of RBC for planar SIS tunnel junctions, SS'S sandwiches, and variable thickness bridges were studied only numerically for some parameter ranges [2]. The main technical difficulty in formulating the analytical criteria of RBC validity is to find the solution to equations describing the perturbation of the superconducting state in S electrodes. In this paper, we will attack this problem by finding the solution to the linearized Usadel equations [5]. We will also use this solution to formulate the corrections to previous results obtained in the RBC approximation.

¶ This article was submitted by the authors in English.

JUNCTION MODEL

Let us consider a structure of the SFIFS type, where, for simplicity, the parameters of the SF bilayers are equal to each other. We assume that the S layers are bulk and that the dirty limit conditions are fulfilled in the S and F metals. We assume further that F metals are weak monodomain ferromagnets with a zero electron–phonon interaction constant and that the FS interfaces are not magnetically active. We will restrict ourselves to the case of parallel orientation of the exchange fields H in the ferromagnets. The results obtained for SFIFS junctions cross over to SNINS and SIS in the corresponding limits.

Under the above assumptions, the problem is reduced to the solution of the one-dimensional Usadel equations [5, 6] in S and F layers and the matching of these solutions by the appropriate boundary conditions [7]. We choose the x axis perpendicular to the plane of the interfaces with the origin at the central barrier I and introduce indexes L (left), R (right), and I for description of the materials and interface parameters of the SFIFS structure located on the left and right sides of the central barrier and at this central barrier, respectively.

The Usadel functions G and F obey the normalization condition $G_\omega^2 + F_\omega F_{-\omega}^* = 1$, which allows for the following parameterization in terms of the new function Φ:

$$G_\omega = \frac{\tilde{\omega}}{\sqrt{\tilde{\omega}^2 + \Phi_\omega \Phi_{-\omega}^*}}, \quad F_\omega = \frac{\Phi_\omega}{\sqrt{\tilde{\omega}^2 + \Phi_\omega \Phi_{-\omega}^*}}. \quad (1)$$

0021-3640/05/8107-0335$26.00

The quantity $\tilde{\omega} = \omega + iH$ corresponds to the general case when the exchange field H is present. However, in the S layers, $H = 0$, and we have simply $\tilde{\omega} = \omega$.

The Usadel equations [5] in the S and F layers have the form

$$\xi_S^2 \frac{\pi T_c}{\pi G_S} \frac{\partial}{\partial x}\left[G_S^2 \frac{\partial}{\partial x}\Phi_S\right] - \Phi_S = -\Delta, \quad (2)$$

$$\xi_F^2 \frac{\pi T_c}{\tilde{\omega} G_F} \frac{\partial}{\partial x}\left[G_F^2 \frac{\partial}{\partial x}\Phi_F\right] - \Phi_F = 0, \quad (3)$$

where $G_\omega = \tilde{\omega}/\sqrt{\tilde{\omega}^2 + \Phi_\omega \Phi^*_{-\omega}}$, $\tilde{\omega} = \omega + iH$ in a ferromagnet (H is the exchange field), $\tilde{\omega} = \omega$ in S and N metals, T_c and Δ are the critical temperature and the pair potential in a superconductor, $\omega = \pi T(2n + 1)$ are the Matsubara frequencies, and $\xi_{S(F)}$ are the coherence lengths related to the diffusion constants $D_{S(F)}$ as $\xi_{S(F)} = \sqrt{D_{S(F)}/2\pi T_c}$. The pair potential satisfies the self-consistency equations

$$\Delta \ln\frac{T}{T_c} + \pi T \sum_{\omega=-\infty}^{\infty} \frac{\Delta - G_S \Phi_S \operatorname{sgn}\omega}{|\omega|} = 0. \quad (4)$$

In the case of an SFIFS tunnel junction in the quasi-one-dimensional geometry, the boundary conditions at the junction plane ($x = 0$) read

$$\xi_F \frac{G_{F,L}^2}{\tilde{\omega}_L} \frac{\partial}{\partial x}\Phi_{F,L} = \xi_F \frac{G_{F,R}^2}{\tilde{\omega}_R} \frac{\partial}{\partial x}\Phi_{F,R}, \quad (5)$$

$$\gamma_{BI} \frac{\xi_F G_{FL,R}}{\tilde{\omega}_L} \frac{\partial}{\partial x}\Phi_{FL,R} = \pm G_{F,R}\left(\frac{\Phi_{F,R}}{\tilde{\omega}_R} - \frac{\Phi_{F,L}}{\tilde{\omega}_L}\right), \quad (6)$$

with

$$\gamma_{BI} = R_N \mathcal{A}_I / \rho_F \xi_F,$$

where the indices L and R refer to the left- and right-hand sides of the junction, respectively, and R_N and $\mathcal{A}_I$ are the normal resistance and the area of FIF interface.

The boundary conditions at the SF interfaces ($x = \mp d_F$) have the form [7]

$$\frac{\xi_S G_{S,k}^2}{\omega} \frac{\partial}{\partial x}\Phi_{S,k} = \gamma \frac{\xi_F G_{F,k}^2}{\tilde{\omega}_k} \frac{\partial}{\partial x}\Phi_{F,k}, \quad (7)$$

$$\pm\gamma_B \frac{\xi_F G_{F,k}}{\tilde{\omega}_k} \frac{\partial}{\partial x}\Phi_{F,k} = G_{S,k}\left(\frac{\Phi_{S,k}}{\omega} - \frac{\Phi_{F,k}}{\tilde{\omega}_k}\right), \quad (8)$$

$$\text{with } \gamma_B = R_B \mathcal{A}_B / \rho_F \xi_F, \quad \gamma = \rho_S \xi_S / \rho_F \xi_F,$$

where R_B and $\mathcal{A}_B$ are the resistance and the area of the SF interfaces; $\rho_{S(F)}$ is the resistivity of the S (F) layer; $k = L, R$. Both of these conditions ensure continuity of the supercurrent.

We will also suppose that, due to the low transparency of the FIF interface, the Josephson current is much smaller than the depairing current of superconducting electrodes, meaning that the suppression of superconductivity in the interior of the electrodes can be neglected and, at $x \longrightarrow \pm\infty$,

$$|\Phi_{S,k}| = \Delta_0, \quad (9)$$

where Δ_0 is the magnitude of the bulk order parameter.

LIMIT OF SMALL F LAYER THICKNESS

In this limit

$$d_F \ll \min\left(\xi_F, \sqrt{\frac{D_F}{2H}}\right) \quad (10)$$

the gradients in (3) are small and, in the second approximation of d_F/ξ_F, the solution of (3) has the form

$$\Phi_{F,k} = A_k + B_k \frac{x}{\xi_F} + \frac{x^2}{2} \frac{\tilde{\omega}_k A_k}{\pi T_c \xi_F^2 G_{F,k}},$$
$$G_{F,k}^2 = \frac{\tilde{\omega}_R^2}{\tilde{\omega}_R^2 + A_k^2(\omega)}. \quad (11)$$

Integration constants $\tilde{A}$ and $\tilde{B}$ in (11) can be found from boundary conditions at $x = 0$,

$$\frac{G_{F,L}^2}{\tilde{\omega}_L} B_L = \frac{G_{F,R}^2}{\tilde{\omega}_R} B_R = \frac{G_{F,L} G_{F,R}}{\gamma_{BI}}\left(\frac{A_R}{\tilde{\omega}_R} - \frac{A_L}{\tilde{\omega}_L}\right) \quad (12)$$

and at $x = \pm d_F$,

$$A_k = A_{0,k} \mp \gamma_B \frac{G_{F,k}}{G_{S,k} + \tilde{\omega}_k \gamma_{BM}/\pi T_c} B_k, \quad (13)$$

$$A_{0,k} = \frac{\tilde{\omega}_{R,L} \Phi_{S,k} G_{S,k}}{\omega(G_{S,k} + \tilde{\omega}_k \gamma_{BM}/\pi T_c)}, \quad \gamma_{BM} = \gamma_B \frac{d_F}{\xi_F}. \quad (14)$$

Expression (13) is valid if $\gamma_B \ll \gamma_{BI}$. Substitution of (11) and (13) into the boundary condition at $x = \pm d_F$ leads to

$$\xi_S \frac{\partial}{\partial x}\Phi_{S,k} = \pm\gamma_M \frac{G_{F,k}}{G_{S,k}^2} \frac{\omega}{\pi T_c} A_k + \gamma \frac{\omega G_{F,k}^2}{\tilde{\omega}_k G_{S,k}^2} B_k, \quad (15)$$

where $\gamma_M = \gamma d_F/\xi_F$, and we reduce boundary problem (2)–(9) to the solution of Eqs. (2), (4) in the S layers with boundary conditions (9), (15). At $H = 0$ and $(\gamma_{BI} d/\xi_F) \gg 1$, expression (15) reduces to the known result for the SN bilayer [8].

LINEARIZED USADEL EQUATIONS

Following the RBC approximation, we will start with the assumption that the suppression of superconductivity in the S layer is weak and that the solution of

the Usadel equations in the superconductor has the form

$$\Phi_{S,k}(\omega) = \Delta_{0,k} + \Phi_{1,k}, \quad \Delta = \Delta_{0,k} + \Delta_{1,k}, \tag{16}$$

$$G_{S,k} = G_0 + G_{1,k}, \quad G_0 = \frac{\omega}{\sqrt{\omega^2 + \Delta_0^2}},$$
$$G_{1,k} = -\frac{G_0}{\omega^2 + \Delta_0^2}\frac{[\Delta_{0,k}^*\Phi_{1,k} + \Delta_{0,k}\Phi_{1,k}^*]}{2}, \tag{17}$$

where $\Delta_{0,k} = \Delta_0\exp\{\pm i\varphi/2 + iUx/\xi_S\}$, φ is the order parameter phase difference across the barrier, and the coefficient U describes the linear growth of the phase difference due to the supercurrent in the electrodes. Corrections to Δ_0 and $\Phi_{S,k}$ are supposed to be small:

$$|\Delta_{1,k}| \ll \Delta_0, \quad |\Phi_{1,k}| \ll \Delta_0. \tag{18}$$

The approximation is valid if the right-hand side of Eq. (15) is also small, so that

$$\xi_S\frac{\partial}{\partial x}\Phi_{1,k} = \Xi_k(\omega), \tag{19}$$

$$\Xi_k(\omega) = \pm\gamma_M\frac{\omega G_{F0,k}A_{0,k}}{\pi T_c G_0^2} + \gamma\frac{\omega G_{F0,k}^2 B_k}{\tilde{\omega}_k G_0^2},$$
$$G_{F0,k} = \frac{\omega\vartheta_k}{\sqrt{\omega^2\vartheta_k^2 + \Delta_0^2 G_0^2}}, \tag{20}$$

where $\vartheta_k = (G_0 + \tilde{\omega}_k\gamma_{BM}/\pi T_c)$ and $|\Xi(\omega)| \ll \Delta_0$. From the structure of the linearized Usadel equations boundary conditions (19), it follows that there are first-order corrections only to the magnitudes Θ and Δ_1 of functions Φ_1 and $\Delta_{1,k}$, respectively, while the phases of all of these functions coincide with those of $\Delta_{0,k}$. In this case,

$$\tilde{\Phi}_{1,k} = \Theta\exp\left\{\pm i\frac{\varphi}{2}\right\}, \quad \Delta_{1,k} = \Delta_1\exp\left\{\pm i\frac{\varphi}{2}\right\} \tag{21}$$

and, due to the symmetry of the structure, we have

$$\tilde{\omega}_R = \tilde{\omega}_L = \tilde{\omega}, \quad G_{F0,k} = G_{F0}, \quad \vartheta_k = \vartheta,$$
$$\frac{A_{0,k}}{\Delta_0} = C_0\exp\left\{\pm i\frac{\varphi}{2}\right\}, \quad C_0 = \frac{\tilde{\omega}G_0}{\omega\vartheta}, \tag{22}$$

$$\Xi_k(\omega) = \frac{G_{F0}}{G_0\vartheta}\left[\pm\gamma_M\frac{\tilde{\omega}}{\pi T_c}\cos\frac{\varphi}{2}\right.$$
$$\left. + i\left(\gamma_M\frac{\tilde{\omega}}{\pi T_c} + 2\frac{\gamma}{\gamma_{BI}}G_{F0}\right)\sin\frac{\varphi}{2}\right]. \tag{23}$$

To write (23), we also used the fact that, in the first order with respect to $|\Xi(\omega)|$, the magnitudes of the functions $\Phi_{S,k}$ in (13) equal Δ_0 and that $G_S = G_0$.

Substituting (16), (21) into (2), (3), we arrive at the following boundary problem for Θ and Δ_1:

$$-\xi_S^2\frac{\pi T_c}{\sqrt{\omega^2 + \Delta_0^2}}\frac{\partial^2}{\partial x^2}\Theta + \Theta = \Delta_1, \tag{24}$$

$$\Delta_1\left[\ln\frac{T}{T_c} + \pi T\sum_{\omega=-\infty}^{\infty}\frac{1}{|\omega|}\right] - \pi T\sum_{\omega=-\infty}^{\infty}\frac{\omega\Theta G_0}{(\omega^2 + \Delta_0^2)} = 0, \tag{25}$$

$$\xi_S\frac{\partial}{\partial x}\Theta(\pm d_F) = \left[\mathrm{Re}\,\Xi_k(\omega)\cos\frac{\varphi}{2} \pm \mathrm{Im}\,\Xi_k(\omega)\sin\frac{\varphi}{2}\right], \tag{26}$$

$$\Xi(\pm\infty) = 0. \tag{27}$$

Due to the symmetry of the problem, it is enough to solve Eqs. (24)–(27) only in one of the electrodes, namely, for $x \geq d_F$. Using the equation for $\Delta_0(T)$,

$$\ln\frac{T}{T_c} + \pi T\sum_{\omega=-\infty}^{\infty}\frac{1}{|\omega|} = \pi T\sum_{\omega=-\infty}^{\infty}\frac{1}{\sqrt{\omega^2 + \Delta_0^2}} \tag{28}$$

and the symmetry relation $\Theta(\omega) = \Theta(-\omega)$, we can rewrite the self-consistency equation in the form

$$\Delta_1\Sigma_2 = \pi T\sum_{\omega>0}^{\infty}\frac{\pi T_c\omega^2}{(\omega^2 + \Delta_0^2)^2}\xi_S^2\frac{\partial^2}{\partial x^2}\Theta, \tag{29}$$

$$\Sigma_2 = \pi T\sum_{\omega>0}\frac{\Delta_0^2}{(\omega^2 + \Delta_0^2)^{3/2}}. \tag{30}$$

The solution of (24), (29) is

$$\Delta_1 = \sum_{\Omega>0}^{\infty}\delta_\Omega\exp\left(-q_\Omega\frac{x - d_F}{\xi_S}\right),$$
$$\Theta = \sum_{\Omega>0}^{\infty}\frac{\delta_\Omega\sqrt{\omega^2 + \Delta_0^2}}{\sqrt{\omega^2 + \Delta_0^2 - \pi T_c q_\Omega^2}}\exp\left(-q_\Omega\frac{x - d_F}{\xi_S}\right), \tag{31}$$

where the coefficients δ_Ω and q_Ω satisfy the equation

$$\Sigma_2 = \pi T\sum_{\omega>0}^{\infty}\frac{\omega^2}{(\omega^2 + \Delta_0^2)^{3/2}}\frac{q_\Omega^2\pi T_c}{\sqrt{\omega^2 + \Delta_0^2} - \pi T_c q_\Omega^2}, \tag{32}$$

$$\sum_{\Omega>0}^{\infty}\frac{q_\Omega\delta_\Omega}{(\sqrt{\omega^2 + \Delta_0^2} - \pi T_c q_\Omega^2)} = -\frac{\Delta_0 P(\varphi, \omega)}{\sqrt{\omega^2 + \Delta_0^2}} \tag{33}$$

and $P(\varphi, \omega) = \mathrm{Re}\,\Xi_R(\omega)\cos(\varphi/2) + \mathrm{Im}\,\Xi_R(\omega)\sin(\varphi/2)$. Multiplying Eq. (33) by $\omega^2(\omega^2 + \Delta_0^2)^{-3/2}$, summing both sides of this equation over ω, and making use of (32),

one can transform (33) into a system of equations for the coefficients δ_Ω, which yields

$$\delta_\Omega = -\pi T \frac{\pi T_c \Delta_0 \Omega^2 q_\Omega}{\Sigma_2 (\Omega^2 + \Delta_0^2)^2} \Lambda(\Omega, \varphi), \tag{34}$$

where

$$\Lambda(\Omega, \varphi) = \left[\gamma_M K_1(\Omega) + \frac{\gamma}{\gamma_{BI}} K_2(\Omega)(1 - \cos\varphi) \right],$$

$$K_1(\Omega) = \frac{\Omega}{\pi T_c G_0} \sqrt{\frac{\sqrt{p^2 + q^2} + p}{2(p^2 + q^2)}}, \tag{35}$$

$$K_2(\Omega) = \frac{pG_0 + (Hq + p\Omega)\gamma_{BM}/\pi T_c}{G_0 (p^2 + q^2)},$$

$$q = 2\gamma_{BM} \frac{H}{\pi T_c} \left(\gamma_{BM} \frac{\Omega}{\pi T_c} + G_0 \right), \tag{36}$$

$$p = 1 + \frac{\Omega^2 - H^2}{(\pi T_c)^2} \gamma_{BM}^2 + 2G_0 \frac{\Omega}{\pi T_c} \gamma_{BM}. \tag{37}$$

Here, $\Omega = \pi T(2m + 1)$ are the Matsubara frequencies.

As a result, the solution of boundary problem (24)–(27) has the form

$$\Delta_1 = -\pi T \sum_{\Omega > 0} \frac{\pi T_c \Delta_0 \Omega^2 q_\Omega \exp\left(-q_\Omega \frac{x - d_F}{\xi_S} \right)}{\Sigma_2 (\Omega^2 + \Delta_0^2)^2} \Lambda(\Omega, \varphi), \tag{38}$$

$$\Theta = -\pi T \sum_{\Omega > 0} \frac{\pi T_c \Delta_0 \Omega^2 q_\Omega \Lambda(\Omega, \varphi) \exp\left(-q_\Omega \frac{x - d_F}{\xi_S} \right)}{\Sigma_2 (\Omega^2 + \Delta_0^2)^2 (1 - \pi T_c q_\Omega^2 G_0/\omega)}. \tag{39}$$

In particular, at $x = d_F$, from (38) and (39) we have

$$\frac{\Theta(d_F)}{\Delta_0} = -\gamma_M \Sigma_{F1} - \frac{\gamma}{\gamma_{BI}} \Sigma_{F2}(1 - \cos\varphi), \tag{40}$$

$$\Sigma_{F1} = \pi T \sum_{\Omega > 0} \frac{\pi T_c \Omega^2 q_\Omega K_1(\Omega)}{\Sigma_2 (\Omega^2 + \Delta_0^2)^2 (1 - \pi T_c q_\Omega^2 G_0/\omega)}, \tag{41}$$

$$\Sigma_{F2} = \pi T \sum_{\Omega > 0} \frac{\pi T_c \Omega^2 q_\Omega K_2(\Omega)}{\Sigma_2 (\Omega^2 + \Delta_0^2)^2 (1 - \pi T_c q_\Omega^2 G_0/\omega)}. \tag{42}$$

To calculate sums (41) and (42), one needs to know the expression for the coefficients q_Ω, which can in general be obtained from numerical solution of Eq. (32). Since the main contribution to sums (41), (42) comes from large Ω, the asymptotic behavior of q_Ω at large Ω can be used:

$$q_\Omega^2 = \alpha \frac{\sqrt{\Omega^2 + \Delta_0^2}}{\pi T_c}, \quad \alpha = 1 - \frac{\pi T^2}{\Omega T_c} \ln \frac{\sqrt{\Omega^2 + \Delta_0^2}}{\pi T}. \tag{43}$$

The method developed is valid if the following condition is fulfilled:

$$\left(\gamma_M + \frac{\gamma}{\gamma_{BI}} \right) \max\left\{ 1, \ln\left[\frac{H^2 + (\pi T_c)^2}{\min\{\gamma_{BM}^2, \gamma_M^2\} (\pi T)^2} \right] \right\} \ll 1, \tag{44}$$

$$\gamma_B \ll \gamma_{BI}.$$

Therefore, for the function $\Phi_{S,k}$ in Eq. (14), we get

$$\Phi_{S,k} = (\Delta_0 + \Theta(d_F)) \exp\{\mp i\varphi/2\}, \tag{45}$$

and, substituting (45) into (13), we finally obtain

$$A_k = \left[\Delta_0 + \frac{\omega \mu C_0}{\tilde{\omega}} \Theta(d_F) \right] C_0 \exp\{\pm i\varphi/2\} \mp 2i \frac{\gamma_B}{\gamma_{BI}} \frac{\tilde{\omega} G_0 G_{F0} \Delta_0}{\omega \vartheta^2} \sin\frac{\varphi}{2}, \tag{46}$$

$$\mu = 1 + G_0 \tilde{\omega} \gamma_{BM}/\pi T_c. \tag{47}$$

From the structure of coefficients $\tilde{A}_{R,L}$, we see that the corrections to the supercurrent across the SFIFS tunnel junction leads not only to the reduction of the critical current of the structure but also to changes in the $J_s(\varphi)$ relation.

$J_s(\varphi)$ RELATION

Using the standard expression for the supercurrent [11], boundary condition (6), and Eq. (46), we can write down the supercurrent I across the SFIFS junction in the form

$$I = (J_0 + J_{11}) \sin\varphi + J_{12} \sin 2\varphi, \tag{48}$$

where

$$J_0 = \frac{\pi T}{e R_N} \sum_{\omega = -\infty}^{\infty} \frac{\Delta_0^2 C_0^2}{\tilde{\omega}^2 + C_0^2 \Delta_0^2}, \quad C_0 = \frac{\tilde{\omega} G_0}{\omega \vartheta}, \tag{49}$$

$$J_{11} = -\frac{2\pi T}{e R_N} \sum_{\omega = -\infty}^{\infty} \frac{\Delta_0^2 C_0^2}{(\tilde{\omega}^2 + C_0^2 \Delta_0^2)^2} \left[\gamma_M \frac{\tilde{\omega} \omega C_0 \mu}{0} \Sigma_{F1} + \frac{\gamma_B}{\gamma_{BI}} \frac{\tilde{\omega}^2 G_{F0}}{\vartheta} + \frac{\gamma}{\gamma_{BI}} \frac{\tilde{\omega} \omega C_0 \mu}{\Delta_0} \Sigma_{F2} \right], \tag{50}$$

$$J_{12} = -\frac{\pi T}{e R_N} \sum_{\omega = -\infty}^{\infty} \frac{\Delta_0^2 C_0^3}{(\tilde{\omega}^2 + C_0^2 \Delta_0^2)^2} \times \left[\frac{\gamma_B}{\gamma_{BI}} \frac{G_{F0} \Delta_0^2 C_0}{\vartheta} - \frac{\gamma}{\gamma_{BI}} \frac{\tilde{\omega} \omega \mu \Sigma_{F2}}{\Delta_0} \right]. \tag{51}$$

Expression (49) has been obtained previously in [9–11]. The φ-independent correction to it, J_{11}, is negative and describes the suppression of the $\sin\varphi$ component of the supercurrent. The first term in Eq. (50), which is

proportional to γ_M, takes into account the suppression of superconductivity in the S electrodes due to the proximity of the thin F layer. The last two terms, which are proportional to γ_{BI}^{-1}, describe the suppression of superconductivity by the current across the junction. The larger γ_B and γ are, the weaker the superconductivity induced into the F layer and the stronger the influence of this effect.

The sign of the second harmonic J_{12} depends on the relation between γ_B and γ. At $\gamma_B = 0$, it is positive and $J(\varphi)$ relation (48) has a maximum at $\varphi = \varphi_{max} < \pi/2$. Such a shift was predicted earlier near T_c for SIS tunnel junctions and is due to the suppression of superconductivity near the barrier by a supercurrent [12]. An increase in γ_B leads to additional phase shifts at both SF interfaces and provides the mechanism for the shift of φ_{max} into the region $\varphi > \pi/2$. As a result, at sufficiently large γ_B, the amplitude J_{12} changes its sign and φ_{max} shifts to $\varphi > \pi/2$. Such a competition between suppression by a supercurrent and by the proximity effect was first analyzed in the SNS junctions [13] at $T \approx T_c$. This fact is in full agreement with the results of numerical calculations summarized in [2].

The physical reason for different signs of J_{12} can be easily understood if we consider the two cases separately. Suppose first that γ_B is finite. In this case, the SFIFS structure may be considered a system of three Josephson junctions in series, as shown schematically in Fig. 1. For rough estimates, one can assume that the phase χ of $\Phi_{F,k}$ does not depend on ω. Demanding the equality of the currents across FIF and FS interfaces and taking into account that $I_C \propto \gamma_{BI}^{-1} \ll I_{C1} \propto \gamma_B^{-1}$ for χ, we will have

$$\chi = \varphi/2 - \frac{I_C}{I_{C1}}\sin 2\chi.$$

Substituting this χ into the expression for the supercurrent across the FIF interface, we get

$$I = I_C \sin\left(\varphi - \frac{I_C}{I_{C1}}\sin\varphi\right) \approx I_C\left(\sin\varphi - \frac{\gamma_B}{\gamma_{BI}}\sin 2\varphi\right).$$

Therefore, with increasing γ_B, the phase partly jumps at the FS interfaces, leading to a continuous crossover from the Josephson effect lumped at $x = 0$ to the phase drop distributed at $|x| \le d_F$. In full agreement with the theory of double barrier devices [2], this crossover results in the appearance of a second harmonic in $J_S(\varphi)$ with a negative sign, which provides for a maximum $J_S(\varphi)$ achieved at $\varphi \ge \pi/2$.

If $\gamma_B = 0$, the structure is always lumped at $x = 0$ and the main effect is the suppression of superconductivity by a supercurrent in the vicinity of the FIF interface, as

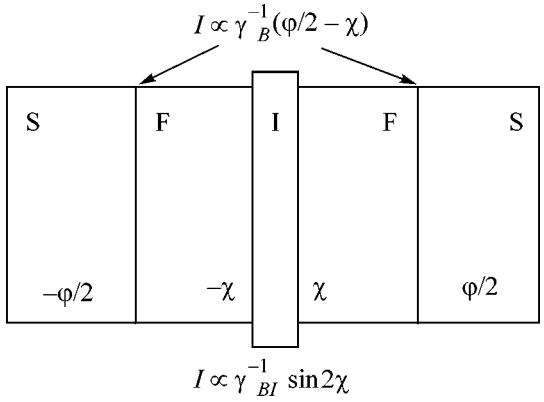

Fig. 1. The phase distribution in a SFIFS junction.

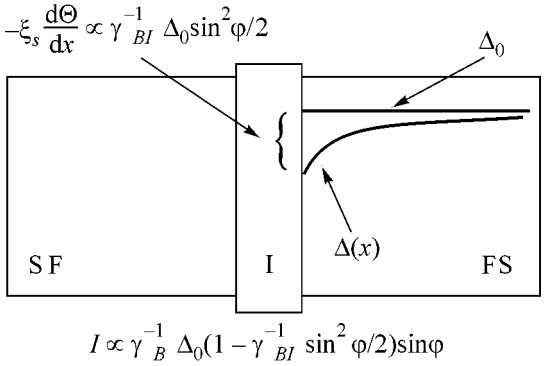

Fig. 2. Depairing by current near the tunnel barrier.

shown schematically in Fig. 2. The resulting contribution to the full current is

$$I_\omega \propto \gamma_{BI}^{-1}\left(\Delta_0 - \xi_S\frac{\partial\Theta}{\partial x}\right)\sin\varphi \propto \frac{\Delta_0}{\gamma_{BI}}\left(1 - \frac{\sin^2\frac{\varphi}{2}}{\gamma_{BI}}\right)\sin\varphi. \quad (52)$$

It follows directly from (52) that the amplitude of the second harmonic is positive.

The competition of the above two mechanisms of $I(\varphi)$ deformation is clearly seen from Eq. (51).

General expressions (49)–(51) can be simplified in several limiting cases.

In the symmetric SNINS tunnel junctions, $H = 0$ in both electrodes and, in the first approximation from (49), the earlier result from [8] is reproduced:

$$J_0 = \frac{2\pi T}{eR_N}\sum_{\omega \ge 0}^{\infty}\frac{\Delta_0^2}{(\omega^2 + \Delta_0^2)\Theta(\omega)},$$

$$\Theta(\omega) = (1 + 2G_0\omega\gamma_{BM}/\pi T_c + (\omega\gamma_{BM}/\pi T_c)^2)$$

while (50) and (51) reduce to

$$J_{11} = -\frac{4\pi T}{eR_N}\left[\gamma_M\Sigma_4 + \frac{\gamma_B}{\gamma_{BI}}\Sigma_5 + \frac{\gamma}{\gamma_{BI}}\Sigma_6\right],$$

$$J_{12} = -\frac{2\pi T}{eR_N}\left[\frac{\gamma_B}{\gamma_{BI}}\Sigma_7 - \frac{\gamma}{\gamma_{BI}}\Sigma_6\right],$$

where

$$\Sigma_4 = \sum_{\omega>0}^{\infty}\frac{\Delta_0 G_0\vartheta\mu\Delta_{F1}}{(\omega^2+\Delta_0^2)\Theta^2(\omega)},$$

$$\Sigma_5 = \sum_{\omega>0}^{\infty}\frac{\Delta_0^2\vartheta^2}{(\omega^2+\Delta_0^2)\Theta^{5/2}(\omega)},$$

$$\Sigma_6 = \sum_{\omega>0}^{\infty}\frac{G_0\Delta_0\vartheta\mu\Sigma_{F2}}{(\omega^2+\Delta_0^2)\Theta^2(\omega)},$$

$$\Sigma_7 = \sum_{\omega>0}^{\infty}\frac{\Delta_0^4}{(\omega^2+\Delta_0^2)^2\Theta^{5/2}(\omega)},$$

and $G_0 = \omega/\sqrt{\omega^2+\Delta_0^2}$.

In the limit $\gamma \longrightarrow 1$, H, γ_M, γ_B, $\gamma_{BM} \longrightarrow 0$, the SFIFS structure transforms into a SIS tunnel junction. In this case,

$$C_0 = 1, \quad A_{pR,L} = [\Delta_0 + \Theta(d_F)]\exp\{\pm i\varphi/2\},$$

$$\Theta(d_F) = -\frac{2}{\gamma_{BI}}\pi T\sum_{\Omega>0}\frac{\pi T_c\Delta_0\Omega^2 q_\Omega\sin^2\frac{\varphi}{2}}{\Sigma_2(\Omega^2+\Delta_0^2)^2(1-\pi T_c q_\Omega^2 G_0/\omega)},$$

and, for the supercurrent I in the first approximation, we have the well-known result of the Ambegakaokar–Baratoff theory [14]:

$$I = \frac{2\pi T}{eR_N}\sum_{\omega>0}^{\infty}\frac{\Delta_0^2}{\omega^2+\Delta_0^2}\sin\varphi.$$

Using (32) for J_{11} and J_{12}, it is easy to get

$$J_{11} = -\frac{\Delta_0}{eR_N}2\Sigma_3, \quad J_{12} = \frac{\Delta_0}{eR_N}\Sigma_3, \qquad (53)$$

$$\Sigma_3 = \frac{4}{\gamma_{BI}}\pi T\sum_{\Omega>0}\frac{\Delta_0\Omega^2}{(\Omega^2+\Delta_0^2)^2 q_\Omega},$$

and the full current across the tunnel junctions is

$$I = \frac{\Delta_0}{eR_N}\left[\frac{\pi}{2}\tanh\frac{\Delta_0}{2T} - 2\Sigma_3\right]\sin\varphi + \frac{\Delta_0\Sigma_3}{eR_N}\sin 2\varphi.$$

The critical current is achieved at a phase difference φ_c,

$$\varphi_c = \frac{\pi}{2} - \frac{4\Sigma_3}{\pi}\tanh^{-1}\frac{\Delta_0}{2T},$$

and equals

$$I_c \approx \frac{\Delta_0}{eR_N}\left[\frac{\pi}{2}\tanh\frac{\Delta_0}{2T} - 2\Sigma_3\right]$$

at $T \longrightarrow 0$, $I(\varphi)$ simplifies to

$$I_c \approx \left[\frac{\Delta_0}{eR_N}\frac{\pi}{2} - \frac{1.92}{\gamma_{BI}}\left(\frac{\pi T_c}{\Delta_0}\right)^{3/2}\right].$$

At $T \approx T_c$, Eqs. (53) transform into the result obtained in [12].

CONCLUSIONS

In summary, we have studied the current–phase relations $J_S(\varphi)$ in SFIFS, SNINS, and SIS junctions in the regime in which the second harmonic of $J_S(\varphi)$ is not small. To solve this problem self-consistently, we have developed an analytical method for solving the linearized Usadel equations. This solution describes a weak suppression of the superconducting state in a superconductor caused either by the proximity of normal or ferromagnetic material or by a current in composite SN or SF proximity systems. The method is rather general and can be applied to a wide spectrum of proximity problems.

We have demonstrated that the full current across structure (48) consists of the sum of the $\sin\varphi$ and $\sin 2\varphi$ components and have calculated the amplitudes ($J_0 + J_{11}$) and J_{12} of these components. In SIS and SNINS structures, the corrections J_{11} and J_{12} to the previously calculated critical current J_0 are small. The $J(\varphi)$ curve is slightly deformed so that the maximum value of the supercurrent is achieved at the phase difference φ_c, which can be smaller or larger than $\pi/2$ for a positive or negative sign of J_{12}, respectively. In SFIFS junctions, $J_0 = 0$ at the point of the transition from the 0 to the π state. This means that, in this case, the calculated values J_{11} and J_{12} determine the $J(\varphi)$ curve. Since the amplitudes J_{11} and J_{12} may have comparable magnitude, the $J(\varphi)$ measured experimentally can be essentially different from $\sin\varphi$. The validity of the approach developed is determined by inequalities (44) and $\gamma_B \ll \gamma_{BI}$. These conditions also determine the validity of rigid boundary conditions in the models [2] describing the properties of SFIFS, SNINS, and SIS tunnel junctions.

This work has been supported in part by the Russian Ministry of Education and Science, by the Russian Foundation for Basic Research grant no. 040217397-a, INTAS grant no. 01-0809, NWO-RFBR cooperation program no. 047.016.005, and the ESF PiShift program.

REFERENCES

1. K. K. Likharev, Rev. Mod. Phys. **51**, 101 (1979).
2. A. A. Golubov, M. Yu. Kupriyanov, and E. Il'ichev, Rev. Mod. Phys. **76**, 411 (2004).
3. V. V. Ryazanov, V. A. Oboznov, A. Yu. Rusanov, *et al.*, Phys. Rev. Lett. **86**, 2427 (2001).
4. S. M. Frolov, D. J. van Harlingen, V. A. Oboznov, *et al.*, Phys. Rev. B **70**, 144505 (2004).
5. K. D. Usadel, Phys. Rev. Lett. **25**, 507 (1970).
6. A. I. Buzdin and M. Yu. Kupriyanov, Pis'ma Zh. Éksp. Teor. Fiz. **53**, 308 (1991) [JETP Lett. **53**, 321 (1991)].
7. M. Yu. Kupriyanov and V. F. Lukichev, Zh. Éksp. Teor. Fiz. **94**, 139 (1988) [Sov. Phys. JETP **67**, 1163 (1988)].
8. A. A. Golubov and M. Yu. Kupriyanov, Zh. Éksp. Teor. Fiz. **96**, 1420 (1989) [Sov. Phys. JETP **69**, 805 (1989)].
9. F. S. Bergeret, A. F. Volkov, and K. B. Efetov, Phys. Rev. Lett. **86**, 3140 (2001).
10. V. N. Krivoruchko and E. A. Koshina, Phys. Rev. B **63**, 224515 (2001); Phys. Rev. B **64**, 172511 (2001).
11. A. A. Golubov, M. Yu. Kupriyanov, and Ya. V. Fominov, Pis'ma Zh. Éksp. Teor. Fiz. **75**, 223 (2002) [JETP Lett. **75**, 190 (2002)].
12. M. Yu. Kupriyanov, Pis'ma Zh. Éksp. Teor. Fiz. **56**, 414 (1992) [JETP Lett. **56**, 399 (1992)].
13. Z. G. Ivanov, M. Yu. Kupriyanov, K. K. Likharev, *et al.*, Fiz. Nizk. Temp. **7**, 560 (1981) [Sov. J. Low Temp. Phys. **7**, 274 (1981)].
14. V. Ambegaokar and A. Baratov, Phys. Rev. Lett. **10**, 486 (1963).

JETP Letters, Vol. 81, No. 7, 2005, pp. 342–345. Translated from Pis'ma v Zhurnal Éksperimental'noĭ i Teoreticheskoĭ Fiziki, Vol. 81, No. 7, 2005, pp. 426–430.

Anomalous Hall Effect and Ferromagnetism in the New Diluted Magnetic Semiconductor $Sb_{2-x}Cr_xTe_3$

V. A. Kulbachinskiĭ[1], P. M. Tarasov[1], and E. Brük[2]

[1] *Moscow State University, Vorob'evy gory, Moscow, 119992 Russia*
e-mail: kulb@mig.phys.msu.ru
[2] *Van der Waals–Zeeman Insituut, Universiteit van Amsterdam, 1018XE Amsterdam, the Netherlands*

Received March 9, 2005

The magnetic and galvanomagnetic properties of single crystals of the new diluted magnetic semiconductor p-$Sb_{2-x}Cr_xTe_3$ ($0 \le x \le 0.02$) have been studied in the temperature range 1.7–300 K. A ferromagnetic phase with the Curie temperature $T_c \approx 5.8$ K and the maximum Cr content $x = 0.0215$ has been revealed. The easy magnetization axis is parallel to the C_3 crystallographic axis. In the presence of strong magnetic fields, the Shubnikov–de Haas effect has been observed. Analysis of this effect shows that doping with chrome reduces the concentration of holes. Negative magnetoresistance and the anomalous Hall effect are observed at liquid helium temperature. © *2005 Pleiades Publishing, Inc.*

PACS numbers: 72.20.My, 72.25.Hg, 72.80.Ey, 75.50.Pp

1. Layered semiconductors similar to Sb_2Te_3 have a rhombohedral structure ($R\bar{3}m$–D^5_{3d} spatial symmetry group) with symmetry axes of the second (C_2) and third (C_3) orders. Crystals Sb_2Te_3 always have p-type conductivity due to a high concentration of charged point defects predominantly of the antistructural type; i.e., antimony atoms substitute for tellurium positions. The formation of such defects is caused by a weak polarity of Sb–Te bonds.

Doping-induced change in the polarity of bonds leads to a change in the concentration of point defects and, therefore, in the concentration of holes. Hence, doping with an element of a certain group of the Periodic Table can lead to both donor and acceptor effects in connection with the effect on the polarity of a bond rather than with the group number. As an example, we point to indium, a Group III element, that provides the donor effect in Sb_2Te_3 [1, 2], which is a narrow-gap semiconductor whose indirect band gap is $E_g = 0.25$ eV (at 295 K) and $E_g = 0.26$ eV (at 4.2 K) [3]. The valence band consists of the upper band of light holes and the lower band of heavy holes. Each band is sixfold degenerate, and the Fermi surface for each band is six-ellipsoidal [1]. The anisotropy of the ellipsoids of the light-hole band is $\eta = S_{max}/S_{min} \approx 3.8$, and their slope angle to the basis plane is $\theta \approx 52.5°$ in Sb_2Te_3.

Recently, it has been found that doping with iron increases the Seebeck coefficient of Bi_2Te_3 [4, 5]. Moreover, low-temperature ferromagnetism was found in p-Bi_2Te_3 (Fe) [4, 6, 7]. More recently, ferromagnetism has been also found in $Sb_{2-x}V_xTe_3$ [8] and $Bi_{2-x}Mn_xTe_3$ [9]. An interesting manifestation of such an interaction in diluted magnetic semiconductors is ferromagnetism observed in GaAs diluted magnetic semiconductors with p-type conductivity (see review [10]).

In addition to pure scientific interest in hole-induced ferromagnetism in diluted magnetic semiconductors, there are promising prospects for using this phenomenon in spintronics for creating devices with controlled spin transport. In this work, the galvanomagnetic and magnetic properties of single crystals of the new diluted magnetic semiconductor p-$Sb_{2-x}Cr_xTe_3$ have been studied. In addition, the Shubnikov–de Haas effect has been analyzed in order to better understand

Shubnikov–de Haas oscillation frequency F; light-hole concentration P for $T = 4.2$ K; resistivity values $\rho_{4.2}$ and ρ_{300} for $T = 4.2$ and 300 K, respectively; Hall mobility μ for $T = 4.2$ K; and experimentally determined Cr content in $Sb_{2-x}Cr_xTe_3$

Sample	F, T	P, 10^{19} cm^{-3}	$\rho_{4.2}$, μΩ cm	ρ_{300}, μΩ cm	μ, m^2/(V s)	Cr, at. %
Sb_2Te_3	54.7	3.4	38.8	260	0.103	0
$Sb_{2-x}Cr_xTe_3$ ($x = 0.0115$)	43.4	2.3	142	437	0.029	0.23
$Sb_{2-x}Cr_xTe_3$ ($x = 0.0215$)	46.2	2.6	106	314	0.066	0.43

0021-3640/05/8107-0342$26.00

the chrome effect on the properties of the initial p-Sb_2Te_3 crystals.

2. The single crystals were grown by the Bridgman method from components taken in the stoichiometric ratio corresponding to the required composition $Sb_{2-x}Cr_xTe_3$. Ingots are easily cleaved along the cleavage planes that are perpendicular to the C_3 axis, i.e., along the (0001) planes, which are usually parallel to the axis of an ampule. Samples with characteristic sizes $1 \times 0.5 \times 4$ mm for measurements were cut by a spark erosion machine. Electric contacts were sealed by a BiSb alloy.

The chrome content in the samples after magnetic and electric measurements was determined by a JEOL-8621 electron microanalyzer. The measurements also show that chrome is uniformly distributed over a sample. The Cr content was found to be 0.23 and 0.43 at. % in two doped samples being investigated. These values correspond to $x = 0.0115$ and 0.0215, respectively, in the formula $Sb_{2-x}Cr_xTe_3$.

The temperature dependences of resistivity, as well as magnetoresistance and the Hall effect, were measured by the standard four-terminal method with current directed along the C_2 axis. A magnetic field up to 6 T was created by a superconducting solenoid, and it was perpendicular to layers along the C_3 axis. The Shubnikov–de Haas effect was measured in pulsed magnetic fields up to 54 T with a pulse duration of 10 ms. Magnetic measurements over the temperature range 1.7–300 K in magnetic fields up to 5 T were carried out in a Quantum Design MPMS-5S SQUID magnetometer. Some parameters of the samples under investigation are given in the table.

3. The resistivity ρ of all samples decreases with temperature, and it is saturated for low temperatures. The temperature dependence in the range 150–300 K has the form $\rho(T) \sim T^m$ with $m \approx 1.2$. The deviation from the $m = 1.5$ value characteristic of phonon scattering is likely attributable both to the additional scattering of holes on ionized impurities and to the temperature dependence of the effective mass in this temperature range. Chrome doping reduces mobility (see table), although mobility in the sample with 0.43 at. % Cr is higher than that in the sample with 0.23 at. % Cr. The latter property is most likely associated with different numbers of defects that arise in the samples during the growth process. Resistivity increases in the chrome-doped samples, although it is somewhat lower in the sample with higher chrome content. Resistivity in the chrome-doped samples increases also due to the additional scattering of holes by the localized magnetic moments of Cr ions. The latter conclusion is corroborated by the existence of negative magnetoresistance $\rho(B)$ in weak magnetic fields (see Fig. 1). An anomaly in the dependence $\rho(B)$ is observed for $B \approx 1.5$ T.

The Hall coefficient is positive in all samples, and it increases with the chrome content, which indicates a decrease in the hole concentration. However, it is impossible to use this coefficient to calculate the hole concentration, because bismuth and antimony tellurides contain two groups of holes with different unknown concentrations and mobilities. Hence, the temperature and magnetic field dependences of the Hall coefficient are complicated even in the absence of a magnetic impurity in these semiconductors [2, 11]. For this reason, in order to estimate the change in the concentration of light holes when Sb_2Te_3 is doped with chrome, the Shubnikov–de Haas effect is used (see below). The presence of Cr magnetic impurity in the samples under investigation gives rise to the anomalous Hall effect [12], which can be expressed as

$$\rho_{xy} = R_H B + R_a \mu_0 M, \quad (1)$$

where R_H is the standard Hall coefficient, R_a is the anomalous Hall coefficient, and M is the magnetization.

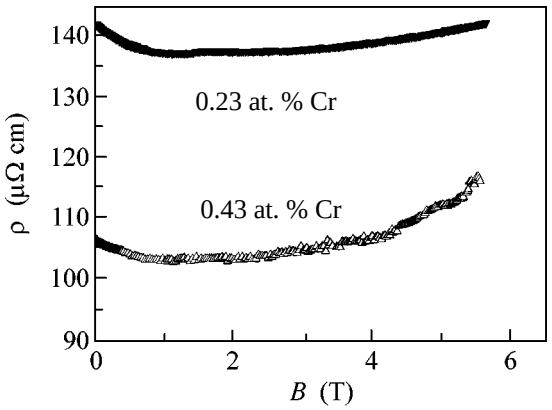

Fig. 1. Negative magnetoresistance of two $Sb_{2-x}Cr_xTe_3$ samples.

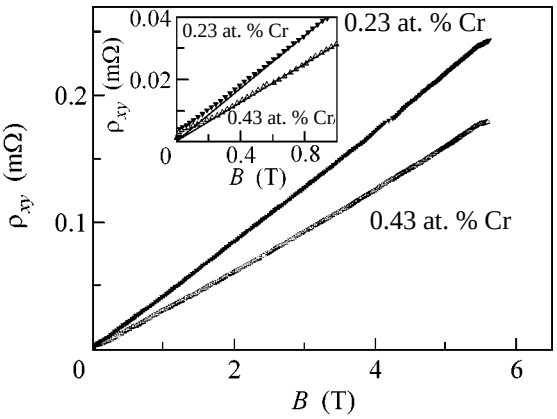

Fig. 2. Hall resistivity ρ_{xy} of the $Sb_{2-x}Cr_xTe_3$ samples vs. the magnetic field. The inset shows the deviation (the anomalous Hall effect) of (points) $\rho_{xy}(B)$ from a linear dependence in weak magnetic fields.

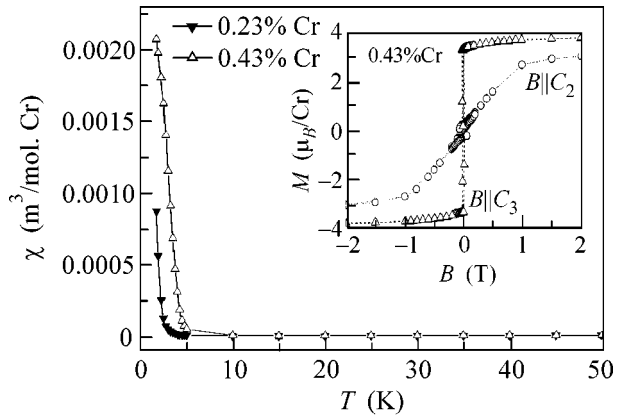

Fig. 3. Temperature dependence of the magnetic susceptibility of $Sb_{2-x}Cr_xTe_3$ in the magnetic field $B = 10$ mT. The inset shows the magnetization loops for the sample with a chrome content of 0.43 at. % at $T = 1.7$ K in the magnetic field B oriented along the C_3 or C_2 axis.

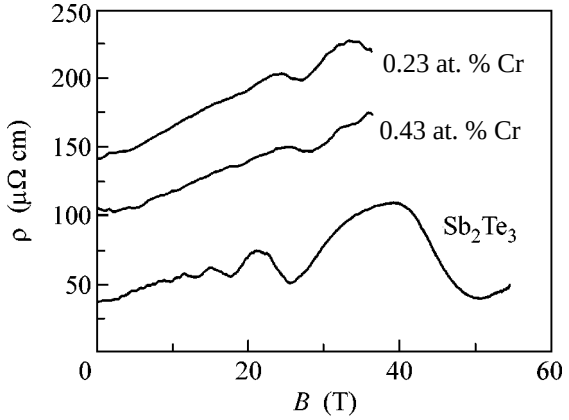

Fig. 4. Shubnikov–de Haas oscillations in $Sb_{2-x}Cr_xTe_3$ and Sb_2Te_3 for $B \parallel C_3$ at $T = 4.2$ K.

Figure 2 shows the Hall resistivity ρ_{xy} as a function of the magnetic field. The inset in Fig. 2 shows the deviation of ρ_{xy} from (straight lines) a linear dependence in weak magnetic fields. This deviation is caused by the anomalous Hall effect, and it is small because the observed ferromagnetism is rather weak.

4. The magnetic susceptibility χ of the Sb_2Te_3 initial single crystal is diamagnetic, it is nearly independent of temperature, and its value is equal to -8×10^{-10} m^3/mole in the principal crystallographic directions. Figure 3 shows the temperature dependence of the magnetic susceptibility of $Sb_{2-x}Cr_xTe_3$ per Cr ion after the subtraction of the diamagnetic background of the matrix in the C_3 direction in the magnetic field $B = 10$ mT. The absolute value of χ increases with the chrome content in the samples. The inset in Fig. 3 shows the magnetization loops for the sample with a chrome content of 0.43 at. % for $T = 1.7$ K in the magnetic field B oriented along the C_3 or C_2 axis. The hysteresis loop for $B \parallel C_3$ is narrow, with a coercivity of ≈15 mT, and the saturation magnetization corresponds to $3.8\mu_B$ per Cr ion. These data indicate the existence of ferromagnetism in the samples with chrome, and they are consistent with the Curie–Weiss temperature dependences of magnetic susceptibility with a positive paramagnetic Curie temperature. When magnetization is measured along the $B \parallel C_2$ direction, the width of the hysteresis loop increases to 70 mT, but the field $B = 2.5$ T is insufficient for the saturation of magnetization. Similar results were also obtained for the sample with a chrome content of 0.23 at. %.

5. The Shubnikov–de Haas effect is analyzed for $T = 4.2$ K in the magnetic field parallel to the C_3 axis. For this orientation, the sections of all six ellipsoids of the upper valence band of light holes coincide with each other, and one oscillation frequency is observed (see Fig. 4). The oscillation amplitude decreases appreciably in the doped samples. The oscillation frequencies are given in the table. The light-hole concentration that is presented in the table is calculated from these frequencies by the procedure described in [13, 14]. The concentration of light holes is lower than the total concentration of holes in the sample, but its change represents a change in the total hole concentration. According to the above data, doping with chrome reduces the concentration of holes, although this effect is nonmonotonic: the hole concentration in the sample with the high chrome content (0.43 at. %) is higher than that in the sample with a chrome content of 0.23 at. %. As was mentioned above, this anomaly can be attributed to different defectiveness degrees of the samples.

The donor action of chrome is associated with its effect on the polarity of bonds. A weak polarity of Sb–Te bonds results in the presence of numerous antistructural defects in the lattice (Sb atoms substitute for Te atoms). Doping with Cr changes the polarity of bonds. This change leads to a change in the concentration of charged point defects and, therefore, to a change in the hole concentration.

Chrome atoms primarily substitute for Sb atoms in the lattice, whereas the Te content remains on a level of 60%. Thus, the $Sb_{2-x}Cr_xTe_3$ solid solution is formed. This assumption is corroborated by a decrease in the unit-cell volume, because the covalent radius for chrome, $r_{Cr} = 0.127$ nm, is lower than that for antimony, $r_{Sb} = 0.138$ nm [15]. According to the x-ray measurements, the lattice constants for Sb_2Te_3 are $a = 0.42643(5)$ nm and $c = 3.0427(4)$ nm, whereas these constants for the sample with 0.43 at. % Cr are $a = 0.402602(4)$ nm and $c = 3.0431(3)$ nm. An increase in the bond polarity when Sb atoms are replaced by Cr atoms reduces the probability of forming antistructural defects. For $Sb_{2-x}Cr_xTe_3$, Sb atoms with electronega-

tivity $X_{Sb} = 1.9$ are replaced by Cr atoms with electronegativity $X_{Cr} = 1.5$, which increases the bond polarity.

6. In the diluted magnetic semiconductors p-$Sb_{2-x}Cr_xTe_3$ under investigation, the direct interaction between magnetic ions is impossible due to their low concentration. Hence, Ruderman–Kittel–Kasuya–Yosida long-range oscillating interaction mediated by holes can be responsible for the ferromagnetic transition. The sign of this interaction corresponds to ferromagnetic interaction, because the first zero of the interaction after which the interaction changes sign and becomes antiferromagnetic lies at a distance that is much larger (due to low hole concentration) than the cutoff length of the interaction. It is clear why ferromagnetism is absent for n-type conductivity: ferromagnetic interaction is hindered due to both a low effective mass and a small exchange integral of electrons. According to a theory developed by Jungwirth *et al.* [16, 17] for homogeneous systems with random distribution of localized spins, the Curie temperature T_c is determined from the formula

$$k_B T_c = \frac{cS(S+1)}{3}\frac{J_{pd}^2}{(g\mu_B)^2}\chi_f(p, T). \qquad (2)$$

Here, c is the magnetic impurity concentration, S is the Cr-ion spin determined from magnetization measurements, J_{pd} is the constant of the exchange interaction between localized magnetic moments and spins of current carriers, g is the Lande factor, μ_B is the Bohr magneton, and χ is the magnetic susceptibility that depends on the hole concentration p and temperature T. Disregarding correlation effects, we estimate susceptibility by the Pauli expression $\chi = (g\mu_B)^2 p/E_F$ or $\chi = (g\mu_B)^2 m^* k_F/h^2$, where h is Planck's constant and m^* is the effective mass of current carriers. Jungwirth *et al.* [17] supposed an additional contribution $\chi = (g\mu_B)^2 e^2 (m^*)^2/\varepsilon h^4$, where ε is the dielectric constant. When hole concentration is high (as in Sb_2Te_3), first contribution dominates. According to estimates for $g = 2$ and experimental values $S = 3/2$ for Cr and $T_c = 5.8$ K, the exchange constant is equal to 0.2–0.3 eV nm^3. This value is an order of magnitude less than the value calculated for (Mn)GaAs, but ferromagnetism is absent in (Mn)GaAs for such a low concentration of magnetic impurities. The above estimate is an upper estimate, because it contains the mass of current carriers and the heavy-hole mass is much larger than the electron mass.

Thus, investigation of the new diluted magnetic semiconductor $Sb_{2-x}Cr_xTe_3$ with p-type conductivity has revealed hole-induced ferromagnetism with a Curie temperature $T_c \approx 5.8$ K. The easy magnetization axis is parallel to the C_3 crystallographic axis. Magnetic measurements show that chrome is in the Cr^{3+} state. The Ruderman–Kittel–Kasuya–Yosida interaction in $Sb_{2-x}Cr_xTe_3$ is the most probable mechanism of the exchange interaction responsible for ferromagnetism. Doping with chrome within the range under investigation reduces the hole concentration. The presence of a magnetic impurity leads to negative magnetoresistance and the anomalous Hall effect.

We are grateful to T. Gortenmulder for the analysis of the chrome content in the samples.

REFERENCES

1. V. A. Kulbachinskii, Z. M. Dashevskii, M. Inoue, *et al.*, Phys. Rev. B **52**, 10 915 (1995).
2. N. B. Brandt and V. A. Kulbachinskii, Semicond. Sci. Technol. **7**, 907 (1992).
3. V. A. Kul'bachinskiĭ, H. Ozaki, Y. Miyahara, and K. Funagai, Zh. Éksp. Teor. Fiz. **124**, 1358 (2003) [JETP **97**, 1212 (2003)].
4. V. A. Kul'bachinskiĭ, A. Yu. Kaminskiĭ, K. Kindo, *et al.*, Pis'ma Zh. Éksp. Teor. Fiz. **73**, 396 (2001) [JETP Lett. **73**, 352 (2001)].
5. V. A. Kulbachinskii, A. Yu. Kaminsky, V. G. Kytin, and A. de Visser, J. Magn. Magn. Mater. **272–276**, 1991 (2004).
6. V. A. Kulbachinskii, A. Yu. Kaminsky, K. Kindo, *et al.*, Phys. Lett. A **285**, 173 (2001).
7. V. A. Kulbachinskii, A. Yu. Kaminsky, K. Kindo, *et al.*, Physica B (Amsterdam) **311**, 292 (2002).
8. J. S. Dyck, Wei Chen, P. Hajek, *et al.*, Physica B (Amsterdam) **312–313**, 820 (2002).
9. J. Choi, S. Choi, Jiyoun Choi, *et al.*, Phys. Status Solidi B **241**, 1541 (2004).
10. H. Ohno, J. Magn. Magn. Mater. **200**, 110 (1999).
11. V. A. Kulbachinskii, A. Yu. Kaminsky, K. Kindo, *et al.*, Phys. Status Solidi B **229**, 1467 (2002).
12. *The Hall Effect and Its Applications*, Ed. by C. L. Chien and C. R. Westgate (Plenum, New York, 1980).
13. V. A. Kulbachinskii, A. Yu. Kaminsky, R. A. Lunin, *et al.*, Semicond. Sci. Technol. **17**, 1133 (2002).
14. V. A. Kulbachinskii, G. V. Zemitan, C. Drasar, and P. Lostak, Fiz. Tverd. Tela (St. Petersburg) **40**, 441 (1998) [Phys. Solid State **40**, 404 (1998)].
15. P. Lostak, C. Drasar, J. Navratil, and L. Benes, Cryst. Res. Technol. **31**, 403 (1996).
16. T. Jungwirth, J. Masĕk, Jairo Sinova, and A. H. MacDonald, Phys. Rev. B **68**, 161202(R) (2003).
17. T. Jungwirth, J. Köonig, J. Sinova, *et al.*, Phys. Rev. B **66**, 012402 (2002).

Translated by R. Tyapaev

JETP Letters, Vol. 81, No. 7, 2005, pp. 346–350. Translated from Pis'ma v Zhurnal Éksperimental'noĭ i Teoreticheskoĭ Fiziki, Vol. 81, No. 7, 2005, pp. 431–436.

Nonchiral BN Haeckelite Nanotubes

S. V. Lisenkov[1], G. A. Vinogradov[1], T. Yu. Astakhova[1], and N. G. Lebedev[2]

[1] *Emanuel Institute of Biochemical Physics, Russian Academy of Sciences, ul. Kosygina 4, Moscow, 119991 Russia*
e-mail: lisenkov@sky.chph.ras.ru

[2] *Faculty of Physics, Volgograd State University, ul. Prodol'naya 30, Volgograd, 400062 Russia*

Received March 9, 2005

A new class of boron–nitrogen (BN) nanotubes composed of tetragons, pentagons, hexagons, heptagons, and octagons is considered. By analogy with carbon nanotubes of the same topological structure, these nanotubes were called Haeckelites. The geometry, energetics, and electronic properties were studied in detail for two regular mutual arrangements of the polygons. It was found that Haeckelite nanotubes are dielectrics with the energy gap E_g = 3.24–4.09 eV. As the nanotube diameter increases, the energy gap E_g decreases, approaching the value for the corresponding planar Haeckelite layer. The ground-state energy of the Haeckelite BN nanotubes is 0.3 eV/atom higher than that of well-known hexagonal BN nanotubes. © *2005 Pleiades Publishing, Inc.*

PACS numbers: 61.46.+w, 73.20.At, 73.22.–f

Carbon nanotubes were discovered in 1991 [1]. Subsequent intensive studies demonstrated that these systems exhibit a set of properties useful for potential applications [2, 3]. More recently, it was found that carbon is not the only element capable of forming nanotube structures. As early as in 1992, the first noncarbon nanotubes were synthesized based on layered molybdenum disulfide and tungsten disulfide [4]. In 1995, boron–nitrogen (BN) nanotubes were obtained by the arc-discharge method [5]. More recently, a method for producing BN nanotubes from carbon nanotubes by a substitution reaction was described [6]. Further studies demonstrated that other chemical elements can form nanotube structures under certain synthesis conditions [4]. Note that the existence and stability of BN nanotubes was theoretically predicted [7, 8] before they were detected experimentally.

As was previously found using the tight-binding (TB) method [7] and density functional theory (DFT) [8], the BN nanotubes composed of hexagons [henceforth referred to as $(BN)_6$] are dielectrics with a band gap ($E_g \sim 5.5$ eV) almost independent of the diameter and chirality. This is a dramatic difference between BN and carbon nanotubes; the latter can be either semiconductors or metals depending on their chirality and diameter [2]. The mechanical properties of BN nanotubes were studied with the use of the nonorthogonal TB method [9, 10]. Menon and Srivastava [11] found that zigzag-type $(BN)_6$ nanotubes are energetically more favorable than the armchair-type nanotubes. More recently, this conclusion was supported experimentally [12]. Note that both of these types of carbon nanotubes are energetically equally favorable.

In 2000, the existence of a new class of carbon nanotubes composed of either pentagons and heptagons or pentagons, hexagons, and heptagons was predicted [13]. Of course, these nanotubes topologically satisfy Euler's theorem; namely, the numbers of nonhexagonal units are pairwise equal for an arbitrary number of hexagons. In particular, if a nanotube consists of pentagons, hexagons, and heptagons, the number of pentagons n_5 is equal to the number of heptagons n_7. These nanotubes composed of nonhexagonal structure-forming units were called Haeckelites. Based on nonorthogonal TB calculations, Terrones *et al.* [13] concluded that Haeckelite carbon structures are energetically more favorable than C_{60} fullerene and exhibit metallic conductivity. Lambin and Biro [14] considered various conceivable types of Haeckelite carbon nanotubes. Recently, Rocquefelte *et al.* [15] calculated the electronic structures and vibrational spectra of a number of carbon nanotubes of this type using the DFT method and made a number of suggestions that allowed them to experimentally identify Haeckelite carbon nanostructures.

By analogy with carbon nanotubes, it is of interest to consider BN nanotubes composed of polygons other than hexagons. However, unlike purely carbon nanotubes, in which the presence of polygons with odd numbers of edges is permissible, this possibility for BN nanotubes is prohibited by the existence of energetically unfavorable B–B and N–N bonds in nonalternant systems [16]. For this reason, tetragons, hexagons, and octagons are feasible structural units provided that Euler's theorem is obeyed: $n_4 = n_8$ for an arbitrary number of hexagons.

In this work, we hypothesize the existence of a new class of Haeckelite BN nanotubes consisting of tetragons and octagons $[(BN)_{48}]$ or additionally including hexagons $[(BN)_{468}]$. It is shown that such nanotubes are energetically possible. For comparison with the above

types, a BN nanotube consisting of pentagons and heptagons [$(BN)_{57}$] was also considered.

The calculations were performed using DFT [17] in the generalized gradient approximation using the Perdew–Burke–Ernzerhof parameterization [18]. Ultrasoft Vanderbilt pseudopotentials [19] were used to describe atomic core electrons. The required basis set of sheet waves was specified by the kinetic energy cutoff parameter (so-called cutoff energy), which was equal to 45 Ry. The cutoff energy for charge density was chosen to be 360 Ry. The test calculations demonstrated that the use of higher cutoff energies changed the total energy by less than 1 meV. The atomic coordinates and unit-cell parameters were relaxed using the BFGS method [20] until forces acting on the atoms and mechanical stresses in the cell became lower than 2.5×10^{-3} eV/Å and 3×10^{-3} GPa, respectively. In the geometric optimization of nanotubes, 4–18 *k* points in the Brillouin zone were used. For each particular calculated structure, it was found that a further increase in the number of *k* points changed the total energy by less than 1 meV. The Monkhorst–Pack method [21] was used for the generation of *k* points.

Classification of BN Haeckelites. Since a nanotube can be represented as a graphite sheet rolled into a cylinder, we initially considered the planar prototypes of BN Haeckelite structures. First, the equilibrium geometric structure of Haeckelites should be determined. We considered two main types of these structures; one of them (Fig. 1a) consists of tetragons, hexagons, and octagons [henceforth referred to as $(BN)_{468}$]. Among numerous such structures, we considered only the one shown in Fig. 1a. Structures composed of tetragons and octagons [henceforth referred to as $(BN)_{48}$], a planar modification of which is shown in Fig. 1b, form another type of BN Haeckelites. To form BN nanotubes from $(BN)_{468}$ and $(BN)_{48}$ classes, the atoms of the (0,0) cell are joined to the required (*n*,*m*) cell (see Figs. 1a, 1b) using an $n\mathbf{a} + m\mathbf{b}$ vector (where **a** and **b** are the unit-cell vectors and *m* and *n* are integers). Then, both (*n*,*n*) (armchair type, Fig. 1c) and (*n*,0) (zigzag type, Fig. 1d) nanotubes can be obtained from a $(BN)_{468}$ sheet. Here, we use the terms *armchair* and *zigzag*, which were introduced for the designation of various types of carbon and BN nanotubes composed of hexagons, because BN Haeckelite nanotubes are similar to the above types of carbon nanotubes. Note that only armchair-type (*n*,*n*) nanotubes can be produced from a $(BN)_{48}$ sheet (Fig. 1e). According to this classification, we characterize a planar BN structure composed of hexagons as $(BN)_6$, whereas nanotubes formed by rolling this sheet are designated as armchair or zigzag nanotubes (*n*,*m*), as proposed by Rubio *et al.* [7]. Note that our study is restricted to only nonchiral nanotubes.

Energetics of BN Haeckelites. We determine the equilibrium geometry and the cohesive energy of each planar BN Haeckelite structure. For the geometry optimization, we used the supercells of these structures

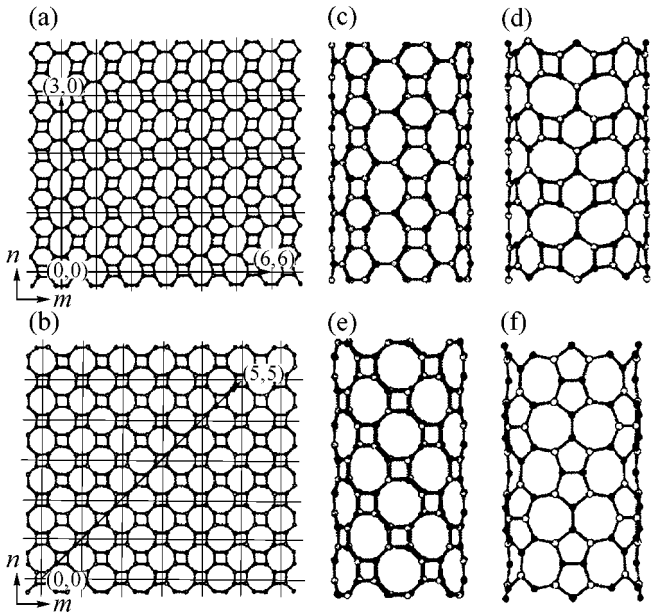

Fig. 1. Fragments of BN Haeckelite nanostructures: (a) $(BN)_{468}$ and (b) $(BN)_{48}$ sheets; (c) (7,7) $(BN)_{468}$, (d) (4,0) $(BN)_{468}$, (e) (6,6) $(BN)_{48}$, and (f) (4,0) $(BN)_{57}$ nanotubes. Open and closed circles indicate boron and nitrogen atoms, respectively.

containing 32 [in the case of $(BN)_6$ and $(BN)_{48}$ sheets] or 36 atoms [in the case of a $(BN)_{468}$ sheet]. In the calculation of the equilibrium geometry, we used 18 *k* points equivalent to a $6 \times 6 \times 1$ network of *k* points generated by the Monkhorst–Pack method [21]. The table summarizes the energies [measured from the energy of the $(BN)_6$ sheet] of all planar structures. It is seen in the table that the $(BN)_{468}$ and $(BN)_{48}$ atomic sheets are energetically less favorable than the $(BN)_6$ sheet by 0.29 and 0.32 eV/atom, respectively. Note that, according to the calculations made in [13, 15], carbon Haeckelite atomic sheets are also energetically less favorable (by ~0.3 eV/atom) than a carbon graphene sheet. It can be seen that the differences between the energies of carbon and BN Haeckelite sheets are nearly identical.

Next, we determined the equilibrium geometry structures and calculated cohesive energies for all above types of Haeckelite nanotubes. The table summarizes the main parameters [average diameter, B–N bond length, and the energy of each particular structure measured from the energy of the $(BN)_6$ planar structure] characterizing the Haeckelite nanotubes. Knowing the cohesive energies of planar BN structures and BN Haeckelite nanotubes, we can determine the strain energies E_{str} required for the formation of nanotube structures with various diameters from the corresponding flat prototype. This energy E_{str} can be calculated as the difference between the energies of a nanotube and the corresponding flat layer from which the nanotube was formed. Figure 2 demonstrates the dependence of

Main parameters (average diameter D; B–N bond length in tetragons, pentagons, hexagons, heptagons, and octagons; energy E measured from the energy of the $(BN)_6$ sheet; and band gap E_g) of hexagonal BN and Haeckelite $(BN)_{48}$ and $(BN)_{468}$ structures

Structure	D, Å	B–N bond length in N-gons, Å					E, eV/atom	E_g, eV
		$N = 4$	$N = 5$	$N = 6$	$N = 7$	$N = 8$		
slab–$(BN)_6$	–			1.45			0.00	4.56
(8,0)–$(BN)_6$	6.57			1.46			0.13	3.56
(10,0)–$(BN)_6$	8.03			1.46			0.08	4.03
(4,4)–$(BN)_6$	5.72			1.46			0.14	4.28
(5,5)–$(BN)_6$	7.14			1.45			0.11	4.31
slab–$(BN)_{468}$	–	1.48		1.45		1.47	0.29	3.24
(2,0)–$(BN)_{468}$	4.88	1.48		1.46		1.47	0.43	3.32
(3,0)–$(BN)_{468}$	7.30	1.48		1.46		1.47	0.35	3.30
(4,0)–$(BN)_{468}$	9.79	1.48		1.46		1.47	0.32	3.28
(4,4)–$(BN)_{468}$	5.92	1.48		1.46		1.47	0.40	3.59
(5,5)–$(BN)_{468}$	7.38	1.48		1.46		1.47	0.36	3.48
(6,6)–$(BN)_{468}$	8.68	1.48		1.46		1.47	0.34	3.41
(7,7)–$(BN)_{468}$	10.21	1.48		1.46		1.47	0.32	3.35
slab–$(BN)_{48}$	–	1.48				1.47	0.32	4.09
(5,5)–$(BN)_{48}$	7.89	1.48				1.47	0.38	4.24
(6,6)–$(BN)_{48}$	9.45	1.48				1.47	0.36	4.20
(7,7)–$(BN)_{48}$	10.99	1.48				1.47	0.35	4.16
(8,8)–$(BN)_{48}$	12.53	1.48				1.47	0.34	4.15
(4,0)–$(BN)_{97}$	9.77		1.47		1.46		0.71	2.02

the strain energy E_{str} of BN nanotubes of the $(BN)_{48}$ and $(BN)_{468}$ types on the mean diameter D. It is seen that the energy E_{str} decreases with increasing diameter of the nanotubes, as in the case of $(BN)_6$ nanotubes [8]. The power approximation of these data exhibited approximately inverse quadratic functions of diameter $E_{str} \sim 4.27/D^2$ (dashed line in Fig. 2) for $(BN)_{48}$ nanotubes and $E_{str} \sim 3.64/D^2$ (solid line in Fig. 2) for $(BN)_{468}$ nanotubes. The approximation $E_{str} \sim 12.39/D^{2.09}$ that was found previously for $(BN)_6$ nanotubes [22] had a much greater (by a factor of about 3–3.5) numerical coefficient. This difference indicates that the flexural modulus of BN Haeckelite nanotubes is lower than that of $(BN)_6$ nanotubes. Note that E_{str} for carbon Haeckelite nanotubes nearly obeys the $1/D^2$ law [13].

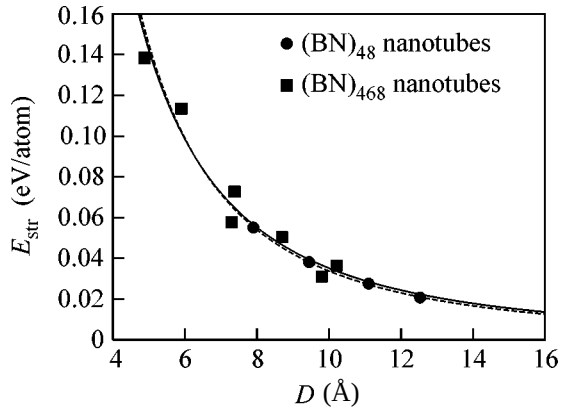

Fig. 2. Specific strain energy E_{str} of BN Haeckelite nanotubes vs. the mean diameter D. Dashed and solid lines indicate the power approximations of the data.

According to the table, $(BN)_{468}$ nanotubes are energetically more favorable (by ~0.03 eV/atom) than $(BN)_{48}$ nanotubes. In general, this result is not surprising, because tetragons and octagons contain stressed chemical bonds, which generally increase the energy of the entire system. In addition, the calculations show that BN Haeckelite nanotubes are energetically less favorable than analogous planar structures. However, the *ab initio* calculations demonstrate that the Haeckelite nanotube structures under consideration are nevertheless stable and they can either exist in nature or be prepared artificially.

Since there are two types of BN nanotubes from the $(BN)_{468}$ class [armchair (n,n) and zigzag $(n,0)$], the conclusion that $(n,0)$ $(BN)_{468}$ nanotubes are energetically more favorable (by ~0.01 eV/atom) than (n,n) $(BN)_{468}$ nanotubes of the same diameter is of great interest. This result is also expected, because these nanotubes are similar to $(BN)_6$ nanotubes, the zigzag type of which is

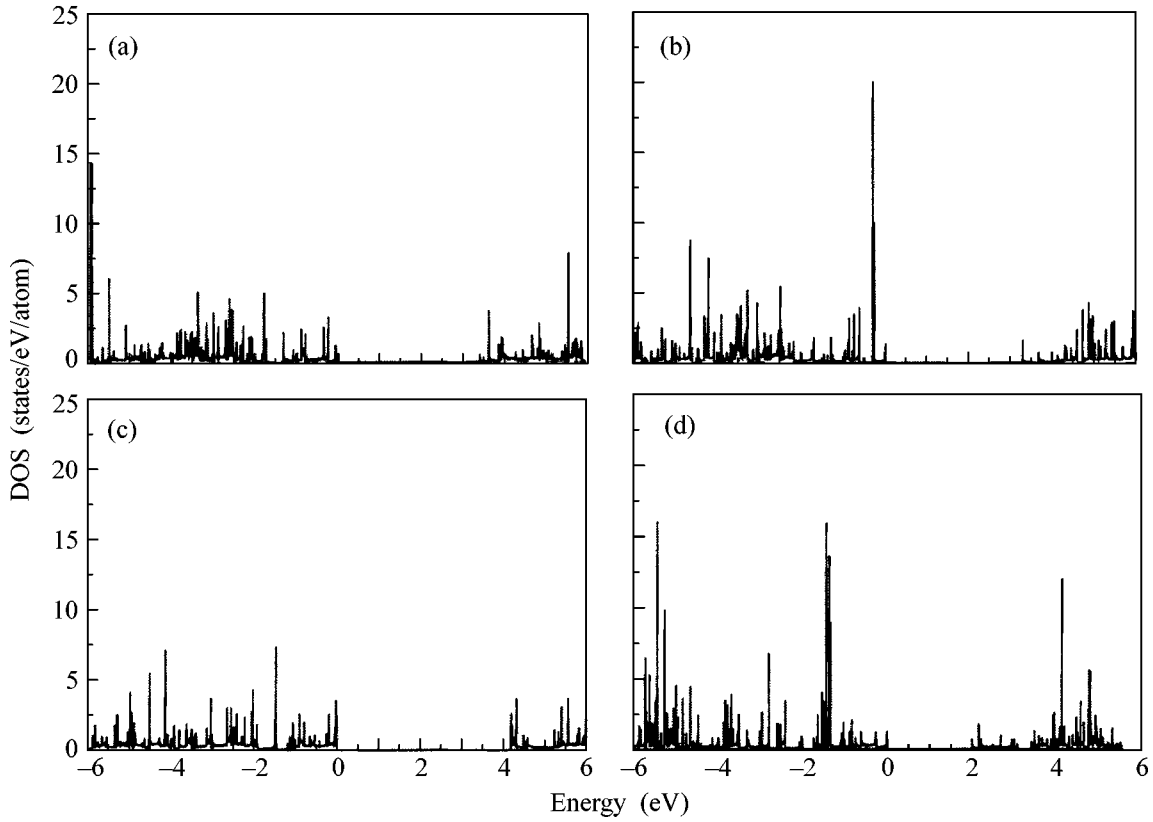

Fig. 3. Electronic densities of states (DOS) of the following BN Haeckelite nanotubes: (a) (7,7) $(BN)_{468}$, (b) (4,0) $(BN)_{468}$, (c) (6,6) $(BN)_{48}$, and (d) (6,0) $(BN)_{57}$. The Fermi level E_F was taken to be zero.

energetically more favorable than the armchair type [11]. Thus, it is expected that the zigzag $(BN)_{468}$ nanotubes would be prepared experimentally.

We compared the energy characteristics of BN Haeckelite nanotubes and $(BN)_6$ nanotubes. We calculated the cohesive energies of $(BN)_6$ nanotubes, and the table summarizes the resulting values. According to the table, $(BN)_6$ nanotubes, as well as a sheet of this type, are the most energetically favorable structures (by ~0.2–0.3 eV/atom), as compared to any class of Haeckelite nanotubes. Note that carbon Haeckelite nanotubes are also energetically less favorable than a carbon graphene sheet (by ~0.2–0.3 eV/atom) and hexagonal carbon nanotubes (by ~0.1 eV/atom) [13, 14]. Thus, the energy differences for carbon and BN Haeckelite nanotubes are approximately identical.

We also considered a BN Haeckelite nanotube that is composed of pentagons and heptagons, (4,0) $(BN)_{57}$, and whose geometric structure is shown in Fig. 1f. We used the classification proposed by Terrones *et al.* [13] for the designation of this class. This nanotube contains B–B and N–N bonds, which are energetically unfavorable [16]. The calculations demonstrated that the energy of the (4,0) $(BN)_{57}$ nanotube is higher than those of $(BN)_{468}$ and $(BN)_{48}$ nanotubes (by ~0.4 eV/atom) or of a $(BN)_6$ sheet (by ~0.7 eV/atom).

Electronic structure of BN Haeckelites. In conclusion, we calculated the electronic structures of planar BN structures and $(BN)_{48}$ and $(BN)_{468}$ nanotubes. Figure 3 shows the electronic density of states (DOS) of (a) (7,7) $(BN)_{468}$, (b) (4,0) $(BN)_{468}$, (c) (6,6) $(BN)_{48}$, and (d) (4,0) $(BN)_{57}$ nanotubes ~10 Å in diameter. The geometric structures of these nanotubes are depicted in Figs. 1c–1f, respectively. It is seen in Fig. 3 that the above BN Haeckelite nanotubes, as well as hexagonal $(BN)_6$ nanotubes, are dielectrics with the energy gaps E_g of 3.35, 3.28, 4.20, and 2.02 eV, respectively. The calculated values of E_g for BN Haeckelite nanotubes with various diameters are also given in the table. It is seen that the (4,0) $(BN)_{57}$ nanotube is characterized by a narrow energy gap (2.02 eV), as compared to the other Haeckelite nanotubes; however, the energy of this nanotube is higher (by ~0.4 eV/atom). A detailed analysis of the electronic structures of all above types of BN Haeckelite nanotubes demonstrated that, as the nanotube diameter D increases, E_g decreases and approaches the value for the corresponding flat layer [3.24 eV for $(BN)_{468}$ or 4.09 eV for $(BN)_{48}$]. Note that the energy gap E_g of the $(BN)_6$ nanotube increases with the diame-

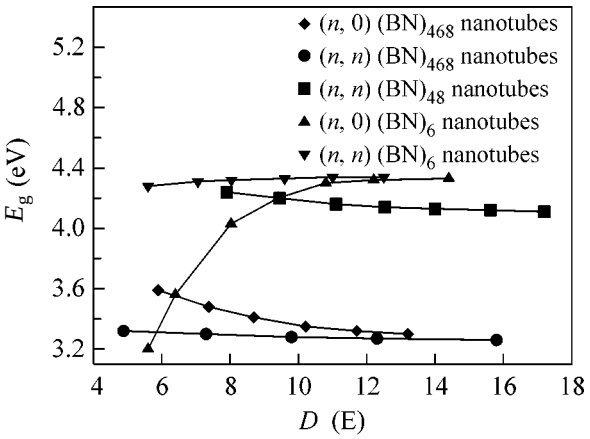

Fig. 4. Energy gap E_g vs. the mean diameter D of BN Haeckelite and hexagonal nanotubes.

ter D and approaches the value for the $(BN)_6$ flat layer [22]. Figure 4 shows the dependence of E_g on the diameter of $(BN)_{468}$, $(BN)_{48}$, and $(BN)_6$ nanotubes. We emphasize that this dependence of E_g on the diameter D of Haeckelite nanotubes is similar to the corresponding dependence for carbon nanotubes. For comparison, note that, according to the calculations performed in [13, 15], carbon Haeckelite nanotubes exhibit metallic conductivity regardless of the chirality and diameter of the nanotubes.

Thus, the *ab initio* calculations provide the conclusion that BN Haeckelite nanotubes are stable but energetically less favorable than hexagonal BN nanotubes. We can also hypothesize that the synthesis of BN Haeckelite nanotubes is possible. The formation of these structures is also probable in the synthesis of multilayered BN nanotubes. This hypothesis is based on the identification of carbon Haeckelite nanostructures that form the inner cavity of multilayered nanotubes [15]. However, this hypothesis can be tested only experimentally.

We are grateful to E.I. Isaev for his assistance in computations. The calculations were performed by S.V.L. at the Russian Joint Supercomputer Center and at the Computer Research Center, Moscow State University. This work was supported in part by the Russian Foundation for Basic Research (project nos. 04-03-96501 and 05-03-328876) and the Russian Academy of Sciences (program "Fundamental Problems of the Physics and Chemistry of Nanosized Systems and Materials").

REFERENCES

1. S. Iijima, Nature **354**, 56 (1991).
2. M. S. Dresselhaus, G. Dresselhaus, and P. C. Eklund, *Science of Fullerenes and Carbon Nanotubes* (Academic, San Diego, 1996).
3. P. J. F. Harris, *Carbon Nanotubes and Related Structures: New Materials for the Twenty First Century* (Cambridge Univ. Press, Cambridge, 1999; Tekhnosfera, Moscow, 2003).
4. R. Tenne and A. K. Zettl, Top. Appl. Phys. **80**, 55 (2001).
5. N. G. Chopra, R. J. Luyken, K. Cherry, *et al.*, Science **269**, 996 (1995).
6. D. Golberg, Y. Bando, W. Han, *et al.*, Chem. Phys. Lett. **308**, 337 (1999).
7. A. Rubio, J. L. Corkill, and M. L. Cohen, Phys. Rev. B **49**, 5081 (1994).
8. X. Blase, A. Rubio, S. G. Louie, and M. L. Cohen, Europhys. Lett. **28**, 335 (1994).
9. E. Hernandez, C. Goze, P. Bernier, and A. Rubio, Phys. Rev. Lett. **80**, 4502 (1998).
10. D. Srivastava, M. Menon, and K. Cho, Phys. Rev. B **63**, 195413 (2001).
11. M. Menon and D. Srivastava, Chem. Phys. Lett. **307**, 407 (1999).
12. D. Golberg, Y. Bando, L. Bourgeois, *et al.*, Appl. Phys. Lett. **77**, 1979 (2000).
13. H. Terrones, M. Terrones, E. Hernandez, *et al.*, Phys. Rev. Lett. **84**, 1716 (2000).
14. Ph. Lambin and L. P. Biro, New J. Phys. **5**, 141 (2003).
15. X. Rocquefelte, G.-M. Rignanese, V. Meunier, *et al.*, Nano Lett. **4**, 805 (2004).
16. J. R. Browser, D. A. Jelski, and T. F. George, Inorg. Chem. **31**, 154 (1992).
17. P. Hohenberg and W. Kohn, Phys. Rev. **136**, B864 (1964).
18. J. P. Perdew, K. Burke, and M. Ernzerhof, Phys. Rev. Lett. **77**, 3865 (1996).
19. D. Vanderbilt, Phys. Rev. B **41**, 7892 (1990).
20. H. B. Schlegel, J. Comput. Chem. **3**, 214 (1982).
21. H. J. Monkhorst and J. D. Pack, Phys. Rev. B **13**, 5188 (1976).
22. H. J. Xiang, J. Yang, J. G. Hou, and Q. Zhu, Phys. Rev. B **68**, 035427 (2003).

Translated by V. Makhlyarchuk

JETP Letters, Vol. 81, No. 7, 2005, pp. 351–355. From Pis'ma v Zhurnal Éksperimental'noĭ i Teoreticheskoĭ Fiziki, Vol. 81, No. 7, 2005, pp. 437–441.

Use of Small-Scale Quantum Computers in Cryptography with Many-Qubit Entangled States¶

K. V. Bayandin and G. B. Lesovik

Landau Institute for Theoretical Physics, Russian Academy of Sciences, Moscow, 117940 Russia

Received December 13, 2004; in final form, March 9, 2005

We propose a new cryptographic protocol. It is suggested to encode information in ordinary binary form into many-qubit entangled states with the help of a quantum computer. A state of qubits (realized, e.g., with photons) is transmitted through a quantum channel to the addressee, who applies a quantum computer tuned to realize the inverse unitary-transformation decoding of the message. Different ways of eavesdropping are considered, and an estimate of the time needed for determining the secret unitary transformation is given. It is shown that using even small quantum computers can serve as a basis for very efficient cryptographic protocols. For a suggested cryptographic protocol, the time scale on which communication can be considered secure is exponential in the number of qubits in the entangled states and in the number of gates used to construct the quantum network. © *2005 Pleiades Publishing, Inc.*

PACS numbers: 03.67.–a

1. INTRODUCTION

In 1982 Feynman suggested that simulation of a quantum system using another such system could be more effective than using classical computers, which demand exponential time depending on the size of the system [1]. Later discussions focused on the possibility of using quantum-mechanical systems for solution of classical problems. For example, Deutsch's algorithm [2] of verification of a balanced function was the first quantum algorithm that worked more efficiently than the classical analog.

The most famous of these, Shor's quantum factorizing algorithm [3], is capable of destroying a widespread cryptographic system RSA [4]. That fact made a strong impression and speeded up the development of quantum cryptography [5] and quantum information processing in general.

It is important to note that quantum mechanics destroying classical ways of coding still gives the possibility of constructing new ones. At present, there exist many ways of coding that use quantum mechanics.

As an example, the quantum algorithm of key distribution using orthogonal states should be mentioned [6]. It was first experimentally realized by Bennet and Brassard [7], who were able to carry out the transmission only at a distance of forty centimeters. Later, a communication line of several kilometers was realized [8].

Another example was first experimentally demonstrated in 1992 [9]. The method uses pairs of entangled photons, part of which, with the help of Bell inequalities of a special form [10], can be used to reveal attempted eavesdropping.

In the present article, another method of coding is proposed. It uses quantum computers for creating entangled states of several qubits. The safety of that method is based on the complexity of tomography for those states.

Later, it will be convenient to treat a single qubit as a spin-1/2 particle. To transmit information, Alice (the sender) first transfers it into a set of units and zeros and divides the numerals into groups of K bits. Then, for every group, she creates a set of K spins in pure states. The spin corresponding to a numeral gets projected along the fixed Z axis if the numeral is zero and projected opposite to the axis otherwise. After that, Alice employs a preset unitary transformation $\hat{U}$ for every group of K spins, thus obtaining a set of entangled quantum-mechanical states that hereinafter will be called messages:

$$|\Psi_k\rangle = \hat{U}|k\rangle, \tag{1}$$

where $|k\rangle$ is an unentangled state of spins with certain projections along the Z axis, and where the projections are defined by the sequence of units and zeros for the binary record of the number k.

Having received K entangled spins, Bob (the receiver) employs the inverse unitary transformation $\hat{U}^{-1}$, thus obtaining the original separable state of spins with defined projections, which can be measured and, thereby, the secret message can be decoded.

It is natural that only Alice and Bob know the unitary transformation $\hat{U}$, providing that Eve (eavesdropper), trying to measure the entangled quantum states,

¶ This article was submitted by the authors in English.

will obtain probabilistic results defined by quantum mechanics.

Further, we will consider ways of learning how to decode the transmitted information and, very importantly, how much time it takes. We will consider two different ways: quantum tomography of every entangled state and a simple guess of the quantum gate network. The obtained results allow an estimate to be made of how long Alice and Bob may safely use the unitary transformation without changing it.

2. QUANTUM TOMOGRAPHY OF AN ENTANGLED STATE

In the simplest case, Eve can determine the secret unitary transformation if she knows exactly what information is sent by Alice. We will not consider the question of how she can do that; we will just assume that, having intercepted the message, Eve knows exactly what information was encoded by Alice. Thus, for simplicity, in this section we deal with many identical entangled states.

The strategy for Eve is to employ quantum tomography for many identical intercepted entangled states. In [11] it was shown that the density matrix of the state of certain spins can be derived without using quantum computers. The idea of the method is based on a measurement of the probability $p(\mathbf{n}_1, m_1; \ldots; \mathbf{n}_K, m_K)$ for every spin $\hat{s}_i$ projected into the state m_i along the direction $\mathbf{n}_i$. The density matrix is determined by Monte Carlo integration:

$$\hat{\rho}_{\text{calc}} = \sum_{\{m_i\}=-\frac{1}{2}}^{\frac{1}{2}} \int\ldots\int \frac{d\mathbf{n}_1 \ldots d\mathbf{n}_K}{(4\pi)^K} p(\mathbf{n}_1, m_1; \ldots; \mathbf{n}_K, m_K) \times \hat{K}_{S_1}(\mathbf{n}_1, m_1)\ldots\hat{K}_{S_K}(\mathbf{n}_K, m_K), \quad (2)$$

where the kernel $\hat{K}_{S_i}(\mathbf{n}_i, m_i)$ acts in the space of the ith spin.

Let us introduce distance into the space of the density matrices:

$$|\hat{\rho}_1, \hat{\rho}_2| = \sqrt{\sum_{i,j} |\hat{\rho}_1 - \hat{\rho}_2|_{ij}^2}, \quad |\hat{\rho}| = \sqrt{\sum_{i,j} |\hat{\rho}|_{ij}^2}. \quad (3)$$

It is known that, in the Monte Carlo method, the relative precision of integration converges as the inverse square of the number of points used [12]. In our case, we have

$$\alpha = \frac{|\hat{\rho}_{\text{calc}} - \hat{\rho}_{\text{true}}|}{|\hat{\rho}_{\text{true}}|} \approx \frac{1}{\sqrt{N}}, \quad (4)$$

where N is the number of different sets of directions used for measurement of spins.

Now, we note that, for every set of fixed directions and for every spin, it is necessary to measure all probabilities for every combination of indices $\{m_i\}$. This takes about const $\times 2^K$ intercepted messages.

Thus, we obtain that, in order to derive every density matrix with precision α, it is necessary to intercept

$$N_{\text{intercepted}} \approx \text{const}\alpha^{-2} \times 2^K \quad (5)$$

messages.

To compose the desired unitary transformation, Eve has to derive the density matrices $\{\rho_k\}$ for all 2^K entangled states. Every density matrix $\{\rho_k\}$ has a single eigenvalue, 1, and an eigenvector $|\Psi_k\rangle$

$$\hat{\rho}_k = |\Psi_k\rangle\langle\Psi_k|. \quad (6)$$

Eve should find eigenvectors of the 2^K density matrices for all entangled states and put them together; thus, she will get the matrix $2^K \times 2^K$ for the unitary transformation $\hat{U}$ in the basis composed of vectors $|k\rangle$. Since the problem of finding an eigenvector for a matrix takes about 2^{2K} elementary operations, the whole problem takes about

$$N_{\text{operations}} = 2^{3K} \quad (7)$$

operations, provided that we have a classical computer that can operate with

$$N_{\text{data}} = 2^{2K} \quad (8)$$

complex numbers.

On top of this, for practical applications, Eve must construct a quantum network by the unitary transformation. As we will see in the next section, the number of necessary basic gates is

$$N_{\text{gates}} \approx 2^{2K}. \quad (9)$$

Therefore, as Alice and Bob increase the number of bits contained in a single message, the number of necessary intercepted messages, the time necessary for deriving the unitary transformation, and the complexity of the constructed quantum network grow exponentially.

3. GUESSING THE UNITARY TRANSFORMATION

Complicated unitary transformations can be constructed using simple ones that mix states of one or two qubits. Examples of actively studied gates for quantum networks are based on superconducting circuits [13], resonant cavities [14], linear ion traps [15], and nuclear magnetic resonance [16].

The operation of a quantum computer can be presented as a network of sequential simple unitary trans-

formations. The whole unitary transformation has the form

$$\hat{U} = \hat{U}_M \hat{U}_{M-1} \ldots \hat{U}_2 \hat{U}_1. \quad (10)$$

Ekert and Jozsa showed [17] that any unitary transformation of qubits can be represented as a network of every possible single-qubit gate and one type of double-qubit gate. An example of a double-qubit gate can be the "controlled NOT," which acts like $|a, b\rangle \longrightarrow |a, a \oplus b\rangle$.

Due to the fact that every gate has its counterpart, which carries out the inverse transformation, we can simply construct the inverse transformation:

$$\hat{U}^{-1} = \hat{U}_1^{-1} \hat{U}_2^{-1} \ldots \hat{U}_{M-1}^{-1} \hat{U}_M^{-1}. \quad (11)$$

Although the method of constructing the quantum network by the matrix of the unitary transformation was presented in [17], in the general case the algorithm requires a polynomial number of gates over the dimension of the matrix $\hat{U}^{-1}$; thus, in our case, it takes a number of gates that is exponential in the number of qubits. Nevertheless, Alice and Bob do not need to construct a quantum network to get a certain unitary transformation: instead, they can just agree on a particular one.

We assume that Alice and Bob possess identical quantum computers that can carry out any of L different simple unitary transformations, provided that there exists an inverse transformation for every one in the set. If Alice and Bob use the simple transformations M times, then the number of possible quantum networks is

$$N_{\text{quant}}(L, M) = L^M. \quad (12)$$

Eve has no chance to guess the correct unitary transformation by trying every quantum network, taking into account that M and L should be greater than the square number of qubits K^2, because Alice and Bob at least need to mix every qubit with each other.

As one can see, dependence (12) is again exponential. This formula does not yet take into account the fact that, for every trial network, Eve must make several measurements of quantum states to realize whether the network she has guessed is correct or not. Let

$$p = \left|\langle k| \hat{U}_{\text{guess}}^{-1} \hat{U} |k\rangle\right|^2 \quad (13)$$

be the probability of erroneous acceptance of a trial unitary transformation $\hat{U}_{\text{guess}}$ instead of the right one $\hat{U}$. Then, the probability of not distinguishing these two transformations after n measurements is

$$P = p^n = e^{n \ln p}. \quad (14)$$

Since, for the overwhelming majority of quantum networks, the probability p is far less than one, a few measurements are sufficient to realize that the network is erroneous.

As a result, we conclude that, to increase the security of the cryptographic method, Alice and Bob should increase not only the number of qubits but also the number of quantum gates used.

4. CASE OF A PRIORI KNOWN TIME CORRELATIONS

Earlier, we supposed that Eve knew what information was coded into the entangled states. Now, we will assume that she knows only the time correlations between messages of K classical bits. The correlations can be described by the value

$$\xi_{kl}(y) = \langle p_k(x) p_l(x + y) \rangle_x, \quad (15)$$

where $p_k(x)$ equals unity, if the xth message is $|k\rangle$, and zero otherwise.

We suppose that Eve possesses *a priori* information such as the frequencies of appearance and the correlations between the K-bit messages that were sent by Alice. She then tries to construct a quantum network that gives the same frequencies and correlations.

The estimated value of intercepted messages necessary for deduction of the unitary transformation is divided into two parts: the number of trial unitary transformations and the number of necessary measurements for each of them to understand whether the correlations are proper or not. The first part of the problem is due to entanglement, and the second is the same as in the case of a classical replacement cipher.

The number of trial unitary transformations is defined by formula (12). For calculation of the correlations, it is necessary to measure a number of quantum states that is polynomial in the value 2^K:

$$N_{cl} \approx P_n(2^K), \quad (16)$$

where the power n of the polynomial $P_n(x)$ corresponds to taking long time correlations into account. This can be understood in the following way: for the calculation of correlations, it is essential to evaluate the probabilities of appearance for the series of n messages, so it is desirable to consider all possible series.

The final number of messages to be intercepted is

$$N_{\text{net}} \approx N_{\text{quant}} * N_{cl}. \quad (17)$$

5. DISCUSSION

In the suggested method of encoding information, the number of messages that Eve must intercept is exponential in the number of qubits and quantum gates used. This is clearly seen from equations (5), (12), and (17).

According to the obtained estimations, it is necessary for Eve to derive the structure of all 2^K entangled states, that is, to intercept

$$N \approx C \times 2^{2^K} \quad (18)$$

messages. This corresponds to transmission of

$$N_{\text{bit}} \sim K \times 2^{2K} \tag{19}$$

bits of classical information.

On the contrary, according to (12), it is necessary for Alice and Bob to preset M numbers less than L to define the order of simple unitary transformations. As we pointed earlier, M and K are of order K^2; therefore, the number of bits required for this is

$$N_{\text{key}} \sim K^2 \log_2 K^2. \tag{20}$$

This expression gives the length of the secret key that must be shared by Alice and Bob. They can use a protocol of quantum key distribution to get it. Expression (19) shows how many classical bits can be safely transmitted using that secret key.

Let us estimate the length of time that Alice and Bob may use a given unitary transformation without changing it. For this, let us consider the encrypting of telephone calls, which require transmission of about fifty thousand bits per second. If the quantum computer operates with $K = 8$ qubits, then, according to our estimates, Eve should intercept $N \approx 65 \times 10^3$ messages, so Alice can send about $NK = 5 \times 10^5$ classical bits or can talk to Bob for ten seconds. If the computer operates with $K = 16$ qubits, then the time necessary to guess the unitary transformation equals several weeks. And in the case of $K = 24$ qubits, the time of secure conversation for Alice and Bob rises to four thousand years.

Although the suggested protocol requires a preset secret key, it still has an advantage over classical block cipher algorithms, which are also believed to be secure for transmission of an exponential number of bits in the length of the key. The example of the RSA system and Shor's algorithm shows that quantum mechanics can greatly simplify the breaking of codes based on the complexity of classical algorithms. On the contrary, the safety of the suggested protocol is assured by fundamental laws of nature.

The main advantage of the suggested protocol is that Alice and Bob, having arranged the secret transformation once, can use it for a long time. The transmission is carried out in one direction, as opposed to the protocols of secret key distribution, which require repeated back-and-forth transmissions from Alice to Bob.

It should be mentioned that, according to Section 4, the problem of determination of the secret unitary transformation is added to the classical cryptographic problems. The main source of additional security is the fact that the cloning of a state is forbidden for any quantum-mechanical system [18]. Due to this theorem, a measurement in a wrong basis may give less information than in the classical case, where an intercepted message can readily be used for correlation calculations. In the quantum case, a part of the intercepted entangled states will be an inevitable distraction for the determination of the secret unitary transformation.

Another issue is that, according to the noncloning theorem [18], Eve destroys the quantum state by measuring it in a wrong basis, and, therefore, she is unable to send the same state to Bob. In accordance with basic principles of quantum cryptography [6], Bob can easily notice the attempted eavesdropping, and he can ask Alice to stop the transmission. In another similarity to the case of relativistic quantum cryptography [19], Bob can detect the attempted eavesdropping by the time delay for incoming messages.

Although the considered protocol looks promising, there are some problems in its realization. First, it appears that the construction of quantum computers capable of handling tens of qubits is still a matter of the future. Second, due to small decoherence times for systems with massive entangled particles, photons remain the best objects for transmission of quantum states, but the conversion of a state of qubits into a state of photons is a challenging problem for experimentalists. Nevertheless, some efforts have been made to study coupling between photons and qubits [20] and to convert pairs of spin-entangled electrons to pairs of polarization-entangled photons [21]. Finally, during the transmission of photons, there is the inevitable influence of the medium on their states, and, therefore, the use of some quantum error-correction techniques will be needed [22].

To conclude, we have presented estimates showing that, for the suggested cryptographic protocol, the time that a secure secret unitary transformation can be used is exponential in the number of qubits within the entangled states and in the number of gates used to construct the quantum network.

Although we can not at the moment present a rigorous proof of the proper statements for Eve's general attack, the suggested protocol in our opinion can serve as an interesting alternative to the existing schemes in quantum cryptography. The main advantage of the cryptographic protocol is that using even relatively small quantum computers with several dozen qubits allows for a practical scheme that is more efficient than existing ones in several respects (e.g., weaker loading of the communication channel).

We acknowledge discussions with S. Molotkov, G. Blatter, R. Renner, M. Feigelman, and M. Skvortzov and financial support through the Russian Foundation for Basic Research, the Russian Ministry of Science, and the Russian Program for Support of Scientific Schools.

REFERENCES

1. R. Feynman, Int. J. Theor. Phys. **21**, 467 (1982).
2. D. Deutsch, Proc. R. Soc. London, Ser. A **400**, 97 (1985).
3. P. W. Shor, SIAM J. Comput. **26**, 1484 (1997).
4. R. Rivest, A. Shamir, and L. Adleman, Technical Report MIT/LCS/TR-212 (MIT Laboratory for Computer Science, 1979).

5. *The Physics of Quantum Information*, Ed. by D. Bouwmeester, A. Ekert, and A. Zeilinger (Springer, Berlin, 2000; Postmarket, Moscow, 2002).
6. C. H. Bennet and G. Brassard, in *Proceedings of IEEE International Conference on Computer Systems and Signal Processing* (IEEE, New York, 1984).
7. C. H. Bennet *et al.*, J. Cryptology **5**, 3 (1992).
8. A. Muller, J. Breguet, and N. Gisin, Europhys. Lett. **23**, 383 (1993).
9. A. K. Ekert *et al.*, Phys. Rev. Lett. **69**, 1293 (1992).
10. J. F. Clauser, M. A. Horne, A. Shimony, and R. A. Hol, Phys. Rev. Lett. **23**, 880 (1969).
11. G. M. D'Ariano, L. Maccone, and M. Paini, quant-ph/0210105.
12. W. H. Press, S. A. Teukolsky, W. T. Veterlingt, and B. P. Flannery, *The Art of Scientific Computing* (Cambridge Univ. Press, Cambridge, 1988–1992), Chaps. 7.6 and 7.8.
13. M. H. Devoret, A. Wallraff, and J. M. Martinis, cond-mat/0411174.
14. *Cavity Quantum Electrodynamics, Advances in Atomic, Molecular and Optical Physics*, Ed. by P. Berman (Academic, New York, 1994), Suppl. 2; S. Haroche, in *Fundamental Systems in Quantum Optics: Les Houche Summer School Session LIII*, Ed. by J. Dalibard, J. M. Raimond, and J. Zinn-Justin (North-Holland, Amsterdam, 1992).
15. J. I. Cirac and P. Zoller, Phys. Rev. Lett. **74**, 4091 (1995); J. F. Poyatos, J. I. Cirac, and P. Zoller, Phys. Rev. Lett. **81**, 1322 (1998).
16. N. A. Gershenfeld and I. L. Chuang, Science **275**, 350 (1997).
17. A. Ekert and R. Jozsa, Rev. Mod. Phys. **68**, 733 (1996).
18. W. K. Wootters and W. H. Zurek, Nature **299**, 802 (1982).
19. S. N. Molotkov and S. S. Nazin, quant-ph/0106046.
20. R. J. Schoelkopf *et al.*, Nature **431**, 162 (2004).
21. V. Cerletti, O. Gywat, and D. Loss, cond-mat/0411235.
22. E. Knill and R. Laflamme, Phys. Rev. A **55**, 900 (1997).